

On-Orbit Photometric Calibration of the WFPC2 Linear Ramp Filters

J. Biretta, P. L. Lim, M. McMaster, and S. Gonzaga
December 17, 2009

ABSTRACT

As part of the WFPC2 close-out calibrations, we have revised the SYNPHOT throughput curves for the linear ramp filters using on-orbit photometry of a standard white dwarf, EGGR-102 (GRW +70 5824). Comparison of the new on-orbit data and previous ground-based calibrations show differences up to ~20%. The accuracy of the new throughput table is expected to be ~2% at most wavelengths, though as noted herein, some wavelengths with limited or no on-orbit data will have poorer accuracy. The new ramp filter throughput file has been delivered to CDBS and will be used in reprocessing the WFPC2 archive.

1. Introduction

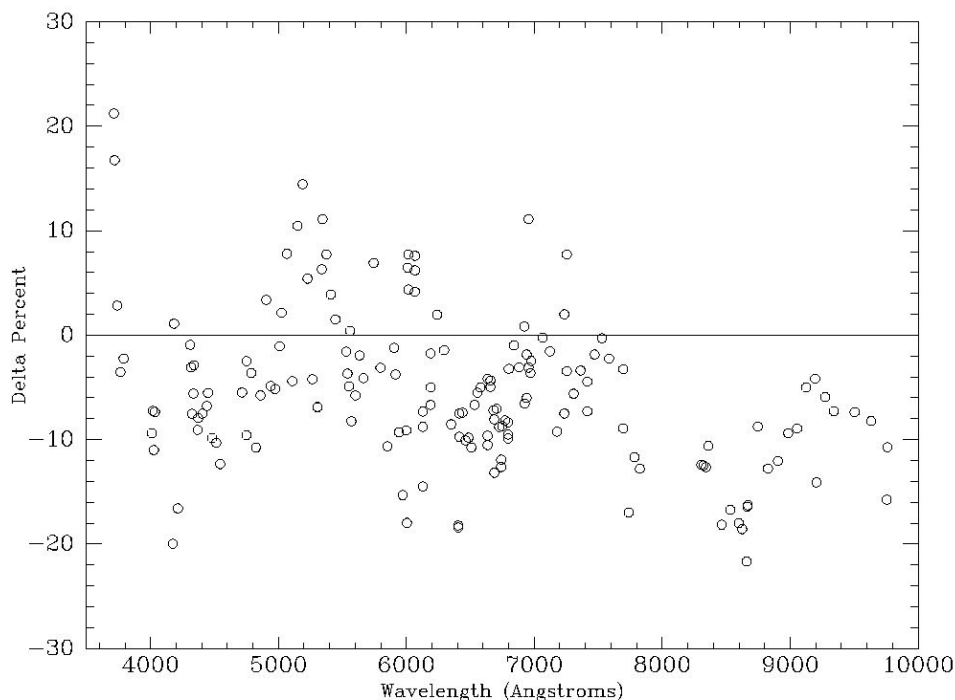
WFPC2 contains a set of linear ramp filters (LRFs), which provide a narrow-band imaging capability ($\Delta\lambda/\lambda \sim 1.3\%$) and are continuously tunable from 3710 Å to 9762 Å. These were designed for “narrow-band emission or absorption line imaging of moderately extended objects” (McMaster, Biretta, et al. 2008; hereafter IHB). Approximately 1500 science images, or 1% of the WFPC2 science program, were obtained through the LRFs. Approximately 326 different wavelength settings were utilized.

The LRFs consist of four filter glasses, namely FR418N, FR533N, FR680N, and FR868N, each containing four separate strips, where the central wavelength varies approximately linearly with the position on the filter glass. Each filter can be used at four possible orientations of the filter wheel (0°, +15°, -18°, and -33°), so as to move the desired

wavelength range into an optimum region on the CCD detectors. In practice, the observer simply specifies the filter as “LRF” with a desired wavelength. The scheduling system uses a look-up table to choose the optimum parameters for that wavelength (Biretta et al. 1996). Just prior to the exposure, the target is slewed to the optimum position on the detector. Due to their design, the unvignetted field-of-view (FOV) is only $\sim 13''$ and a few wavelengths have smaller unvignetted FOVs.

Until the present work, the LRF photometric calibration was based on pre-launch scans of the LRF filter throughputs, which were then incorporated into SYNPHOT (Biretta et al. 1996). Early on-orbit calibrations by M. McMaster et al. (private communications), as shown Figure 1, suggested that there were significant discrepancies between the ground-calibrated throughputs and the on-orbit observations of standard stars, which in some cases were as large as $\sim 20\%$. In this report, we have obtained new on-orbit data, which further confirm the discrepancies between the pre-launch and the on-orbit throughputs. Using all the available on-orbit observations spanning 10 years, we have revised the LRF throughputs and incorporated these results in a revised SYNPHOT LRF table, which can be used for photometric calibration of science data.

Figure 1: Early finding of discrepancies between observed count rates and count rates predicted from the original ground-based LRF throughputs that reside in the SYNPHOT database, courtesy of M. McMaster et al. The Y-axis, “Delta Percent,” is the percentage difference between the observed and the predicted count rates.



We discuss our observations, data reduction, analysis, SYNPHOT table correction, and possible future work in Sections 2 to 6, respectively. Lastly, we summarize our report in Section 7.

2. Observations

All observations herein use the standard white dwarf named EGGR-102, also known as GRW +70 5824. It has $V=12.773$ mag and $B-V=-0.091$ mag (Landolt & Uomoto 2007).

The data were obtained through multi-cycle observations spanning over 10 years, involving four proposals (6194, 8454, 8820, and 11038). Unfortunately, it has not been practical to calibrate every possible wavelength setting of the LRFs. Early proposals made some effort to sparsely calibrate the LRFs across their entire wavelength range. The most recent proposal (11038) attempted to fill-in gaps in wavelengths, where science observations had been made, but where there were no calibration data, or where there appeared to be possible issues with the existing calibration data. Ultimately, due to cost-benefit considerations, some wavelength ranges with relatively few science images would not be calibrated on-orbit (see Section 6).

The fifth proposal, 8054, was not included in our final analysis due to questionable quality of those data caused by missing proper motion information in its Phase II proposal. The star has high proper motions in RA and DEC of -403.80 and -26.17 mas yr⁻¹, respectively (Perryman et al. 1997). The problem was reported in HOPR 593, stating that “not only was the star in the wrong position, but it was also in areas of the Linear Ramp Filters which suffered from vignetting and/or cross talk with other ramp filters, making the data unusable for calibration purposes” (O’Dea et al. 1999; private communications).

3. Data Reduction

We corrected for WF4 anomaly (Biretta & Gonzaga 2005) only for images from proposal 11038 as it is the only one to execute after 2002, when the anomaly started. We flatfielded the exposures using narrow-band reference files from WFPC2 ISR 02-02 (Koekemoer, Biretta, & Mack 2002) closest in wavelength to the respective ramp filters. We limited ourselves to the flatfields in Table 1 due to their better reliability. To investigate the effect of such flatfield choices, we generated two versions of flatfielded images using F502N and F656N reference files, respectively, for ramp filter wavelengths between 5020-6560 Å, which lie at wavelengths between these two filters (see Section 4.3).

Table 1: Reference files used for flatfielding.

Reference File	Filter	USEAFTER Date
m3c10045u	F375N	1996-10-30
m3c1004fu	F502N	1996-10-30
m3c1004nu	F656N	1996-10-30
m3c10052u	F953N	1996-10-30

Where available, we combined exposure pairs with IRAF task “*crrej*” for cosmic ray rejections. We visually examined all single and combined images to exclude “bad” images – cosmic rays, bad pixels or columns, images precariously near chip edges, or in vignetted regions – from our final analysis. Manual cleaning of the single exposures could alter their PSFs and compromise the photometry quality, in addition to being unreasonably labor intensive given the large amount of data (431 usable single data points, excluding proposal 8054); hence, we decided against that procedure. Hereafter, the remaining non-“bad” exposures are referred to as “good” observations.

As suggested in Part II Chapter 5.2 of WFPC2 Data Handbook (Baggett et al. 2002; hereafter DHB), we applied geometric (*f1k1552bu.r9h*) and 34th row (Anderson & King 1999) corrections to the images. We also examined them for saturation but found none.

At the time this work was carried out, WFPC2 was still observing and accepting new proposals. Therefore, an effort was made to reduce and analyze all the existing standard star data, even for those wavelengths where there might ultimately be no science data.

4. Analysis and Discussions

4.1. Conversion between Position and Wavelength

For proposals 8454, 8820, and 11038, we obtained star positions on the chips using central wavelengths in header keyword PHOTMODE and the LRF calculator¹, which linearly interpolated across IHB Tables 3.7 and 3.8 to predict the optimum placement of the star on the detector. Due to the large amount of images, we modified the calculator’s algorithm to be used in a script for batch processing.

Proposal 6194 contained spatial scan observations, i.e., the star was on multiple positions on the same chip in the same exposure. In this case, we manually recorded the star’s positions and then used the LRF calculator to compute the wavelength for each position.

As reported in HOPR 593 (see Section 2) for proposal 8054, the expected positions in the FOV derived using the LRF calculator tool disagreed with the observed positions by about 6.5”, which is sufficient to move the star into vignetted regions of the filter. This was attributable to the missing proper motion information for the star in the Phase II proposal. In general, the other proposals showed good correspondence between the observed star positions and the optimum position on the detector for that wavelength.

¹ http://www.stsci.edu/hst/wfpc2/software/wfpc2_lrfcalc.html

4.2. Photometry

We performed aperture photometry using the IRAF task “*phot.*” Re-centering was done on manually measured positions with “*centroid*” algorithm within a 5-pixel box. We used gain and read noise values from IHB Table 4.2. Full width at half-maximum (FWHM) was obtained with IRAF task “*psfmeasure.*” We used a 0.5" aperture radius around the star (11 and 5 pixels for PC and WF, respectively). To measure the sky level, we used 1.5" inner radius for the annulus with width of 0.5" and the “*centroid*” fitting algorithm.

We applied CTE loss corrections as formulated by Dolphin (2004). For combined images, we divided the star and the sky counts by two prior to correction as CTE loss affected each single exposure individually. For aperture correction, we applied the 0.1-mag factor as stated in DHB page WFPC2:5-21. We followed WFPC2 Photometry Tutorial (Gonzaga 2002) to calculate photometry errors.

4.3. Flux Comparisons for Different Parameters

Given that there was already some evidence for discrepancies between the pre-launch and the on-orbit calibrations, we explored several possible effects which might impact the on-orbit data:

Flatfields: As stated in Section 3, we compared photometry results from the same exposures with ramp wavelengths between 5020–6560 Å reduced using F502N and F656N flatfield reference files. The count rates derived from using the two different flatfields agreed within ~3%, which was the accuracy of the SYNPHOT ground-based calibration (Biretta et al. 1996). In fact, approximately 77% and 59% of the data agreed within 2% and 1%, respectively.

Combined vs. single exposures: We compared count rates measured from combined images with their corresponding single exposures. Their percentage differences followed a somewhat Gaussian distribution, centered on zero with $\sigma \sim 1\%$. This gave us some confidence in the validity of results, where only a single exposure was available.

Throughput vs. epoch: We compared the count rates over time for several ramp wavelength ranges, namely 6200–6300, 6500–6650, 7050–7150, and 7450–7550 Å. For each range, the magnitude fluctuations were $\lesssim 0.2$ mag. The implication of such scatter was inconclusive because the data points had a wide range of central wavelengths. However, detailed studies of LRF (and narrow band) wavelength and bandwidth stabilities had been done separately in WFPC2 ISRs 09-04 (Biretta & Lim 2009) and 09-05 (Lim & Biretta 2009), which generally found excellent stability of the filters ($\lesssim 1$ Å change in central wavelength and $\lesssim 1\%$ change in the bandwidth).

Different proposals: We compared single-exposure count rates from proposal 11038 with observations from the other proposals. We defined a matching pair to have central wavelengths that agreed within 5 Å (not enough data otherwise) and to belong to the same physical ramp on the filter glass (there are some duplications of wavelengths between the end of one ramp and the start of the next one). For 11038 and 6194, only 3 matches were found and they agreed within 3%. For 11038 and 8454, ~81% of the images agree within 3%. Their largest disagreements were ~8% and involved the dataset *u5ly0307r* at 6190 Å from 8454; for unknown reasons, the 11038 data at this wavelength had a ~4" pointing error, which might have contributed to the differences. Discrepancies between 11038 and 8054 were often 15% to 20%; these might be related to the large pointing errors for 8054 previously described (see Section 2). There were no matching wavelengths between proposals 11038 and 8820.

4.4. Comparison Between Observed Counts and SYNPHOT Predictions

The observed count rates were taken from *all* single and combined exposures. For predicted count rates, we used SYNPHOT with the ground-based LRF throughput table and the observed flux for EGGR-102 on the HST pure hydrogen WD flux scale from the CDBS CALSPEC² database. The spectrum table we used is *grw_70d5824_stis_001.fits*, which is $\sim 1\% \pm 0.2\%$ ($\sim 2\%$ at the blue end) brighter than its successor, *grw_70d5824_stisnic_002.fits*. At the time of our analysis, the latter spectrum was not yet available.

Comparisons of the observed and predicted count rates are shown in Figure 2 to Figure 8. Each figure is separated into 3 panels, as explained below:

Top panel: Percentage differences between observed and predicted count rates. Blue, purple, red, orange, and green points represent data from proposals 11038, 8820, 8454, 8054, and 6194, respectively. Filled circles, open squares, and plusses indicate single “good” exposures, combined “good” exposures (i.e., CR-SPLIT), or “bad” exposures (cosmic ray, bad column, or other defects), respectively. For example, a red filled circle is the “good” data from a single exposure from proposal 8454. Results using both the F502N and F656N flats are plotted for data between 5020-6560 Å, as discussed in Section 3.

Middle panel: The approximate number of LRF science exposures taken at each wavelength. The values plotted are the number of exposure logsheet lines in WFPC2 Phase II documents from 1994-2008 as provided by D. Karakla (2008; private communications). The legend box refers to what was mentioned for the top panel.

² <http://www.stsci.edu/hst/observatory/cdbs/calspec.html>

Bottom panel: LRF configurations for the respective ramp wavelength ranges, as defined in IHB Tables 3.7 and 3.8. For instance, the label “FR418P15,WF4,yes” means FR418N rotated at $+15^\circ$ on the WF4 chip with vignetting. The label applies to all the wavelengths within the color crosshatched region (spanning all the panels) where it belongs.

The photon statistical error for the data in Figure 2 to Figure 8 is 0.5% or less. The expected uncertainties including all error sources (flats, CTE corrections, etc.) are about 2%.

Several conclusions can be drawn from these figures. Most importantly, large discrepancies between the observed and the calculated (SYNPHOT) count rates, often up to 20%, are confirmed both by the new data in proposal 11038 and by re-analyses of older data. While these discrepancies seem large, they are similar in size to discrepancies seen between ground-based and on-orbit calibrations for many other WFPC2 filters (“tens of percent,” Holtzman et al. 1995).

Whenever the data from several proposals are available, proposals 6194, 8454, 8820, and 11038 are generally in good agreement with each other (within a few %). As mentioned before, the largest discrepancies between these are $\sim 8\%$ for proposals 8454 and 11038 around 6190 \AA , where proposal 11038 has a $\sim 4''$ pointing error due to unknown causes.

On the other hand, proposal 8054 is often systematically offset from the other proposals. As discussed before, this proposal suffers from $\sim 6''$ pointing errors due to a problem with the phase II proposal. Usually its count rate is lower than the other proposals, which would be consistent with vignetting caused by the pointing error. The largest differences occur around $5950, 7100, 7750, \text{ and } 8550 \text{ \AA}$ and run 15-20% lower than the other proposals. The sizes of these differences are somewhat difficult to understand, as we would expect vignetting to have a slow onset as target leaves the optimum position on the LRF. The $\sim 6''$ pointing error happens to be in the direction perpendicular to the wavelength direction on the filter, which maximizes the vignetting effect. However, this would move the star $1''$ or less into the vignettted region.

Other effects must be invoked to explain these large differences. The filter wheel rotation anomaly (Gonzaga, Baggett, & Biretta 2001; Biretta & Lim 2009) may also be present, where the filter wheel settles $\sim 0.5^\circ$ from the normal position. This would have the largest effect on the WF4 CCD, which is the farthest from the filter wheel rotation axis and could move the star an additional $\sim 2''$ into the vignettted region. The largest errors do, in fact, occur for the WF4 CCD, which may be significant.

However, a combined offset of $\sim 3''$ into the vignettted region is still expected to cause only $\sim 5\%$ light loss. An offset of $7''$ or $8''$ into the vignettted region would be required to produce

the 15-20% observed differences. Hence, it appears that other unknown problems may exist. For example, if there is significant misalignment of the LRF filter relative to the CCDs or if there is a wide non-optical region between the wavelength strips on the LRF. In any case, due to the pointing errors in proposal 8054 and the apparent photometry errors, we decided to ignore those data when revising the SYNPHOT table.

Figure 2: Difference between observed and predicted fluxes, science observation tallies, and instrument configurations for 3600–4600 Å. See text in Section 4.4 for full details.

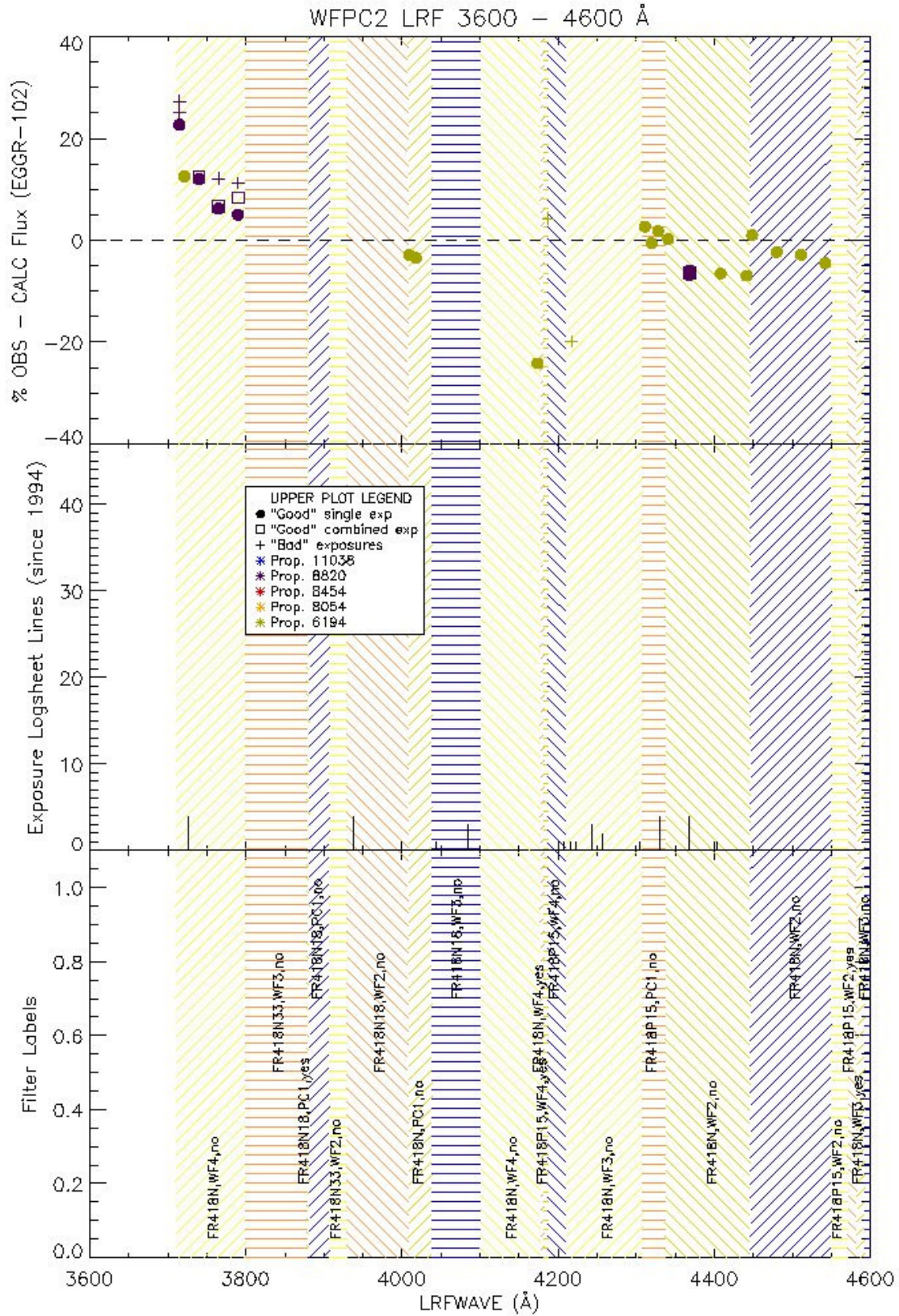


Figure 3: Difference between observed and predicted fluxes, science observation tallies, and instrument configurations for 4600–5600 Å. See text in Section 4.4 for full details.

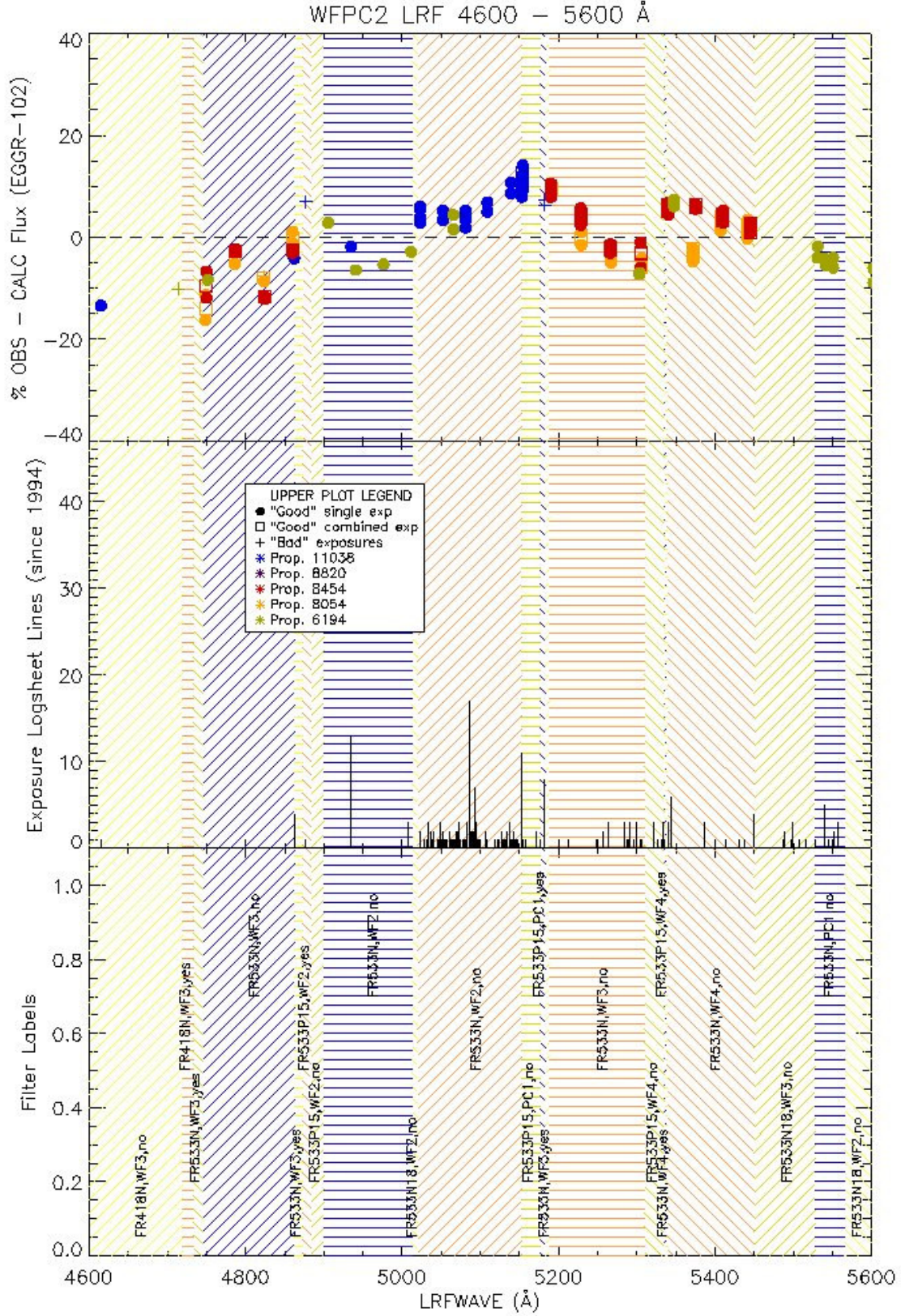


Figure 4: Difference between observed and predicted fluxes, science observation tallies, and instrument configurations for 5600–6600 Å. See text in Section 4.4 for full details.

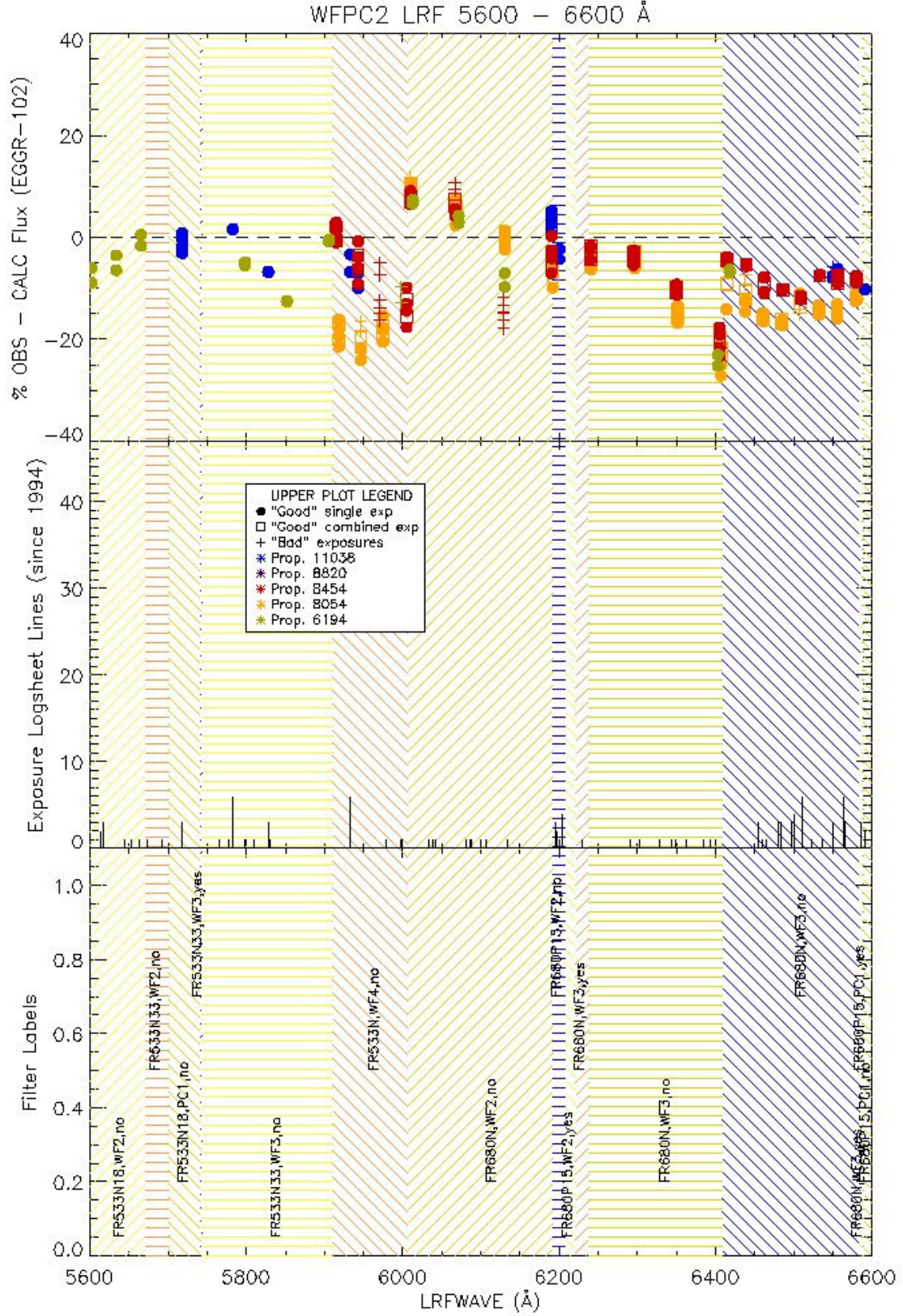


Figure 5: Difference between observed and predicted fluxes, science observation tallies, and instrument configurations for 6600–7600 Å. See text in Section 4.4 for full details.

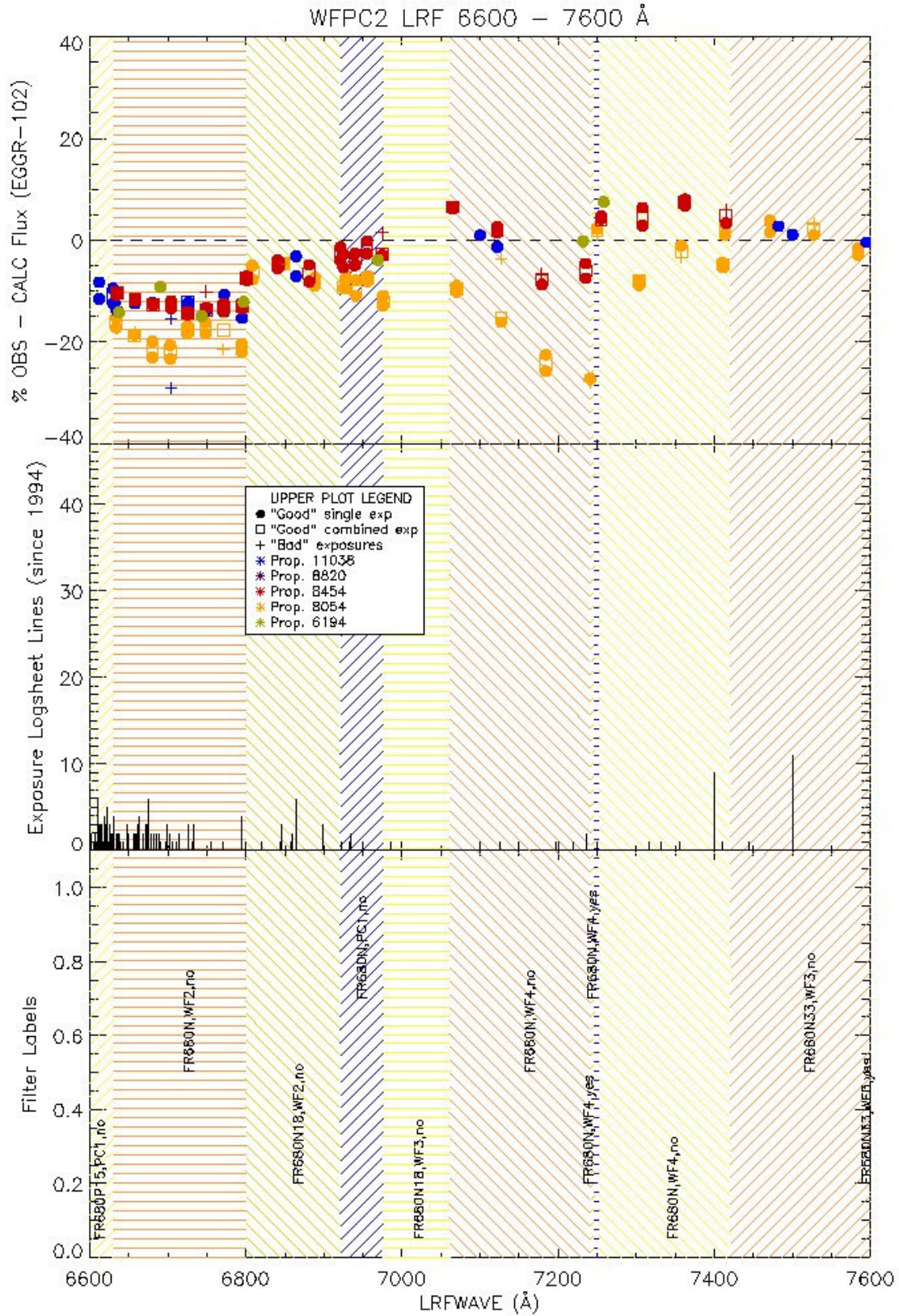


Figure 6: Difference between observed and predicted fluxes, science observation tallies, and instrument configurations for 7600–8600 Å. See text in Section 4.4 for full details.

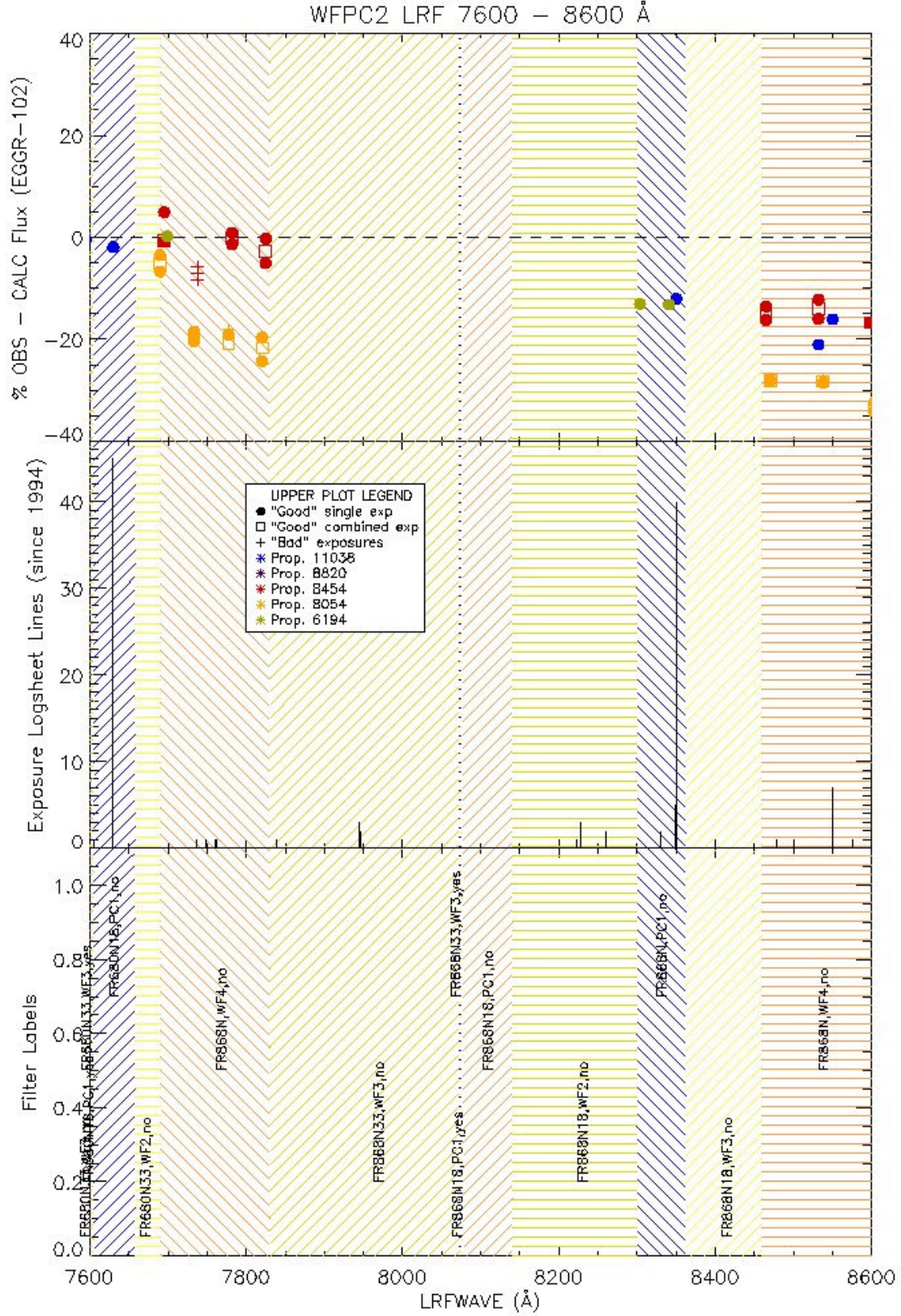


Figure 7: Difference between observed and predicted fluxes, science observation tallies, and instrument configurations for 8600–9600 Å. See text in Section 4.4 for full details.

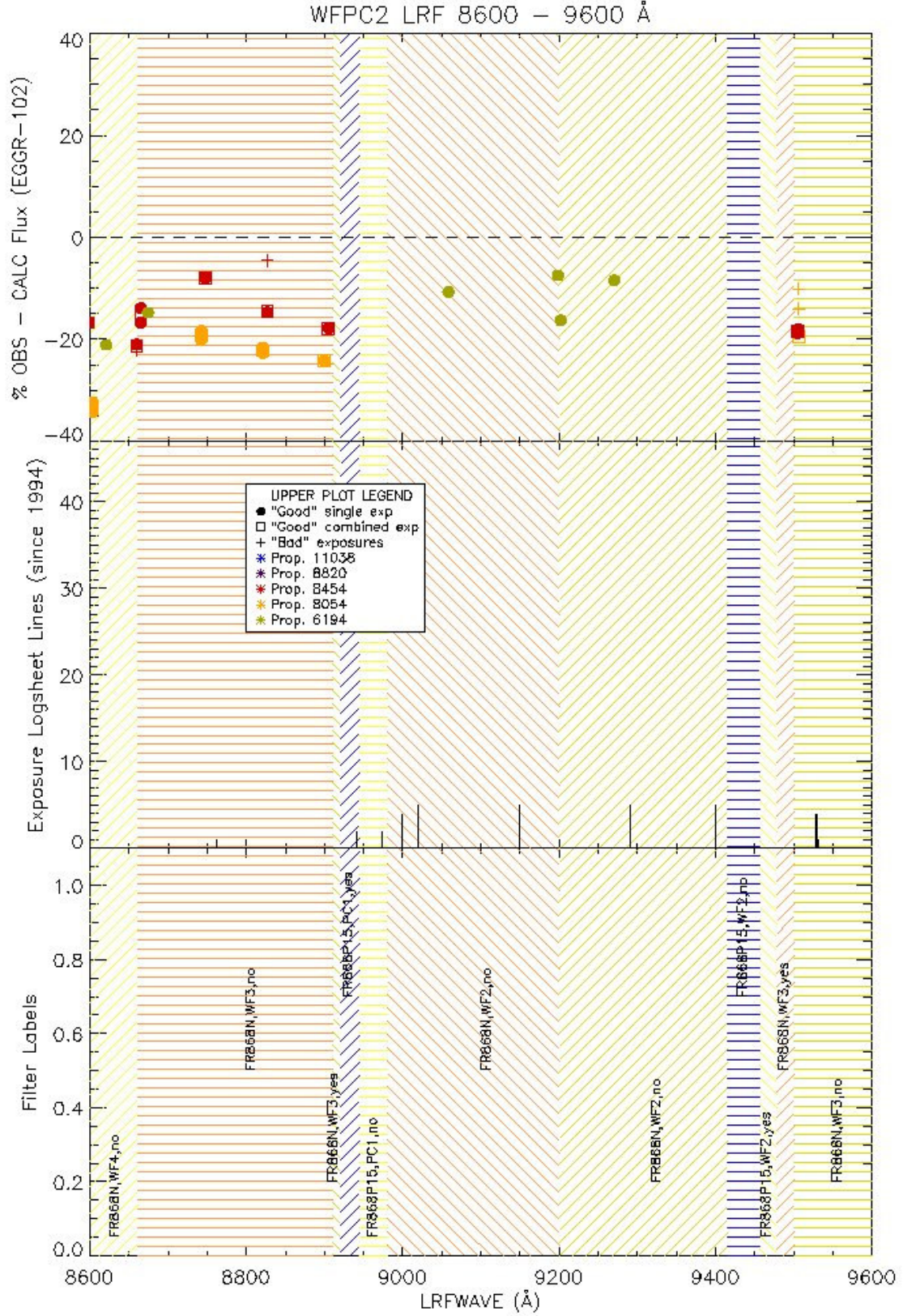
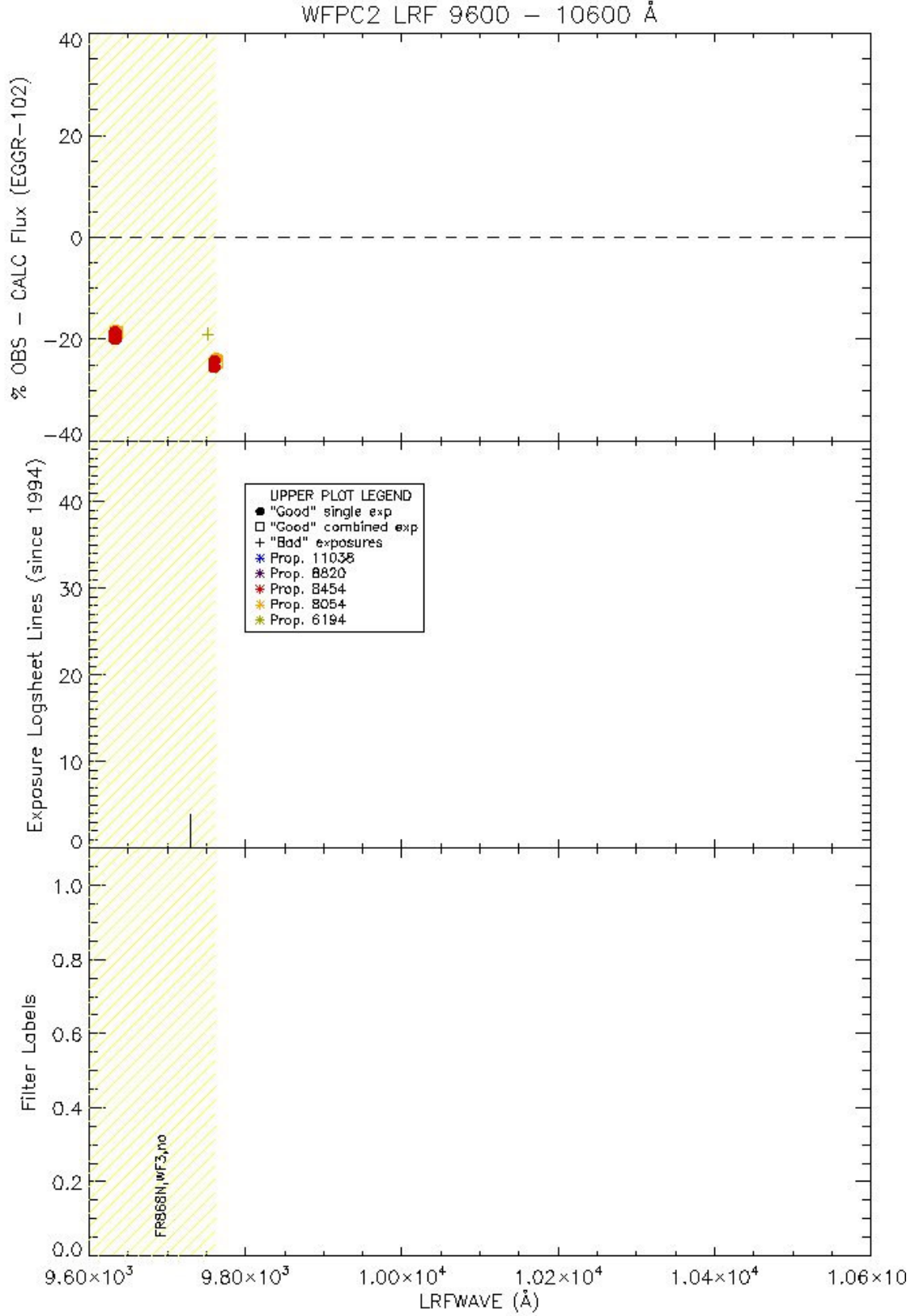


Figure 8: Difference between observed and predicted fluxes, science observation tallies, and instrument configurations for 9600–10600 Å. See text in Section 4.4 for full details.



5. SYNPHOT LRF Table Correction and Delivery

5.1. Throughput Table Correction

From the comparison between observed and predicted count rates, it was clear that the ground-based ramp filter calibrations used by SYNPHOT were not sufficiently accurate. Hence, we had undertaken the effort to revise the LRF throughput table³ using our on-orbit observations. The table format was described in details in the WFPC2 ISR 96-06 (Biretta et al. 1996).

Results in Section 4.4 provided us with the wavelength-dependent percentage differences, D , between observed and predicted count rates, F_{obs} and F_{calc} , respectively. We could characterize the trends using a collection of functions (from straight lines to 3rd-degree polynomials), as defined in Equation 1:

$$D = 100 (1 - F_{calc} / F_{obs}) = A_0 + A_1 \lambda + A_2 \lambda^2 + A_3 \lambda^3, \quad (1)$$

where A_n is the polynomial coefficient for the n^{th} -term and λ is the ramp wavelength.

For each ramp filter configuration as defined in IHB Tables 3.7 and 3.8, we visually chose the best-fitting function, giving more emphasis to wavelengths with science observations. If the trend appeared discontinuous within a configuration, we split it into sub-regions by wavelength so that each one would have a continuous function. Detailed fitting information is in Appendix A. Fitted coefficients are tabulated in Table 2 – Each region is defined by $\lambda_1 < \lambda \leq \lambda_2$ and has N amount fitted data points. Since WFPC2 was still accepting proposals and observing during most of this work, effort was made to fit all the wavelengths with on-orbit calibration data.

Then, we calculated correction factors, C , to be applied to corresponding wavelength regions, as defined in Equations 2 and 3:

$$C = F_{obs} / F_{calc} = (1 - D/100)^{-1}, \quad (2)$$

$$T_{new} = C T_{old}, \quad (3)$$

where T_{old} represents the transmission values from the ground-based throughput table *column* containing LRF wavelength of interest and T_{new} represents the corrected transmission values for the same column in the new throughput table. For wavelength regions with insufficient on-orbit data, their original transmission values were copied as-is to the new table. For continuity, the first (WAVE#3709.999) and the last (WAVE#9762.001) table columns, which are just outside the supported wavelength range, use the same correction coefficients as their

³ The ramp filter throughput table from CDBS we used to calculate and apply our re-calibrations was *wfpc2_lrf_004_syn.fits*.

neighboring columns; the values are tabulated in the first and the last rows of Table 2, respectively.

We compare the observed and predicted count rates with the revised throughput table in Figure 9 to Figure 15. The “good” data showed a RMS of 1.5% with the largest differences being 7% at 6190 Å (Figure A19). For completeness, we also plotted data from proposal 8054 (orange points) and “bad” exposures (pluses) although they were not used for calculations.

The accuracy of the revised LRF throughput table varies from one wavelength range to another. Many of the wavelength ranges of the LRF, especially those with many science observations, are well-sampled by the calibration data, and show modest throughput variations across the range (e.g., Figure A10, Figure A22, and Figure A24). In these cases, the photometric accuracy can be estimated from the residuals in the fits, which is about 2%. Other ranges have poorer sampling, but the calibration and science data are at nearly the same wavelength (e.g., Figure A7) and should also have this same accuracy.

Still, there are wavelength ranges with larger gaps between the calibration and science data (e.g., Figure A11 and Figure A30) and one must be concerned about the possible existence of poorly sampled and rapidly fluctuating throughputs (10-15 %; e.g., Figure A8 and Figure A19). In these situations, the accuracy should be judged on a case-by-case basis and is probably poorer, perhaps ~10%. The optical layout of the camera sets some limit on the possibility of rapid throughput variations with wavelength. This is determined by ~32" diameter of the spherically aberrated OTA pupil at the LRF, which makes large variations unlikely over wavelength ranges $<15 \text{ Å}$ and $<30 \text{ Å}$ at the blue and red ends of the LRF range, respectively. In any case, the accuracies at the following wavelengths are likely to be poorer, perhaps 5-10%, due to larger wavelength separation between the calibration and the science data: 5170, 5980, 6020-6100, 6820, 6900, 7150, 7440, 7610, 7750, 8500, 9000-9200, and 9400 Å. This affects a total of ~40 science observations.

Table 2: Fitted polynomial coefficients used to compute throughput correction factors. All configurations in this table are unvignetted.

λ_1	λ_2	LRF	CHIP	A_0	A_1	A_2	A_3	N^\dagger
3710.00	3800.00	FR418N	WF4	4.679356E+04	-2.475892E+01	3.275484E-03	—	9
4008.00	4038.00	FR418N	PC1	-3.203000E+00	—	—	—	2
4100.00	4177.00	FR418N	WF4	-2.417700E+01	—	—	—	1
4308.00	4337.00	FR418P15	PC1	1.330667E+00	—	—	—	3
4337.00	4369.12	FR418N	WF2	1.053003E+03	-2.425260E-01	—	—	4
4369.12	4446.00	FR418N	WF2	-6.745000E+00	—	—	—	2
4446.00	4550.00	FR418N	WF2	8.835006E+03	-3.877247E+00	4.251704E-04	—	4
4593.00	4720.00	FR418N	WF3	-1.340900E+01	—	—	—	1
4746.00	4863.00	FR533N	WF3	-1.227193E+07	7.664266E+03	-1.595479E+00	1.107068E-04	15
4900.00	5013.00	FR533N	WF2	1.116058E+06	-6.648800E+02	1.320053E-01	-8.734356E-06	5
5020.00	5153.00	FR533N	WF2	1.765887E+04	-6.981838E+00	6.902526E-04	—	18
5153.00	5176.00	FR533P15	PC1	1.178617E+01	—	—	—	6
5188.00	5310.00	FR533N	WF3	1.663671E+04	-6.218528E+00	5.808938E-04	—	26
5339.00	5450.00	FR533N	WF4	-1.408825E+04	5.267533E+00	-4.921656E-04	—	26
5528.00	5541.63	FR533N	PC1	1.080814E+03	-1.959345E-01	—	—	4
5541.63	5566.00	FR533N	PC1	-4.966500E+00	—	—	—	2
5566.00	5671.00	FR533N18	WF2	2.928688E+04	-1.050675E+01	9.420720E-04	—	6
5700.00	5741.00	FR533N18	PC1	-1.159500E+00	—	—	—	4
5743.00	5774.39	FR533N33	WF3	1.650595E+00	—	—	—	(1)
5774.39	5850.10	FR533N33	WF3	9.777683E+02	-1.690848E-01	—	—	6
5850.10	5910.00	FR533N33	WF3	-1.303057E+03	2.205342E-01	—	—	4
5910.00	6007.00	FR533N	WF4	4.830022E+04	-1.605009E+01	1.332967E-03	—	22
6007.00	6063.49	FR680N	WF2	7.538000E+00	—	—	—	8
6063.49	6192.00	FR680N	WF2	1.098196E+05	-3.579261E+01	2.916170E-03	—	20
6192.00	6208.00	FR680P15	WF2	-3.299500E+00	—	—	—	2
6238.00	6409.00	FR680N	WF3	-3.295221E+04	1.053389E+01	-8.419174E-04	—	24
6409.00	6584.00	FR680N	WF3	1.113811E+06	-5.102051E+02	7.789661E-02	-3.964021E-06	51
6590.00	6631.00	FR680P15	PC1	-8.529058E+04	2.581825E+01	-1.954081E-03	—	6
6631.00	6800.00	FR680N	WF2	-8.373680E+05	3.746699E+02	-5.587757E-02	2.777639E-06	41
6800.00	6880.50	FR680N18	WF2	-6.419934E+04	1.875343E+01	-1.369627E-03	—	8
6880.50	6921.00	FR680N18	WF2	-6.645743E+02	9.563333E-02	—	—	6
6921.00	6976.00	FR680N	PC1	-7.501061E+04	2.156445E+01	-1.549915E-03	—	14
7061.00	7241.00	FR680N	WF4	-4.516123E+06	1.900068E+03	-2.664487E-01	1.245371E-05	14
7251.00	7420.00	FR680N	WF4	3.559357E+06	-1.457778E+03	1.990097E-01	-9.055659E-06	12
7420.00	7600.00	FR680N33	WF3	1.810682E+02	-2.390347E-02	—	—	3
7605.00	7658.00	FR680N18	PC1	-1.903000E+00	—	—	—	1
7690.00	7830.00	FR868N	WF4	4.777680E+06	-1.847969E+03	2.382579E-01	-1.023942E-05	10
8300.00	8362.00	FR868N	PC1	-1.279600E+01	—	—	—	3
8460.00	8661.00	FR868N	WF4	-1.340266E+04	3.158884E+00	-1.863380E-04	—	14
8661.00	8910.00	FR868N	WF3	-3.731831E+06	1.270737E+03	-1.442233E-01	5.455818E-06	12
8980.00	9200.00	FR868N	WF2	-9.103000E+00	—	—	—	2
9200.00	9415.00	FR868N	WF2	-1.238350E+01	—	—	—	2
9501.00	9762.00	FR868N	WF3	-1.308946E+04	2.739106E+00	-1.434962E-04	—	8

[†] Number in parenthesis means that the data point used for visual fitting actually belongs to a neighboring region with the same configuration.

Figure 9: Same as Figure 2 but with corrected SYNPHOT throughput table.

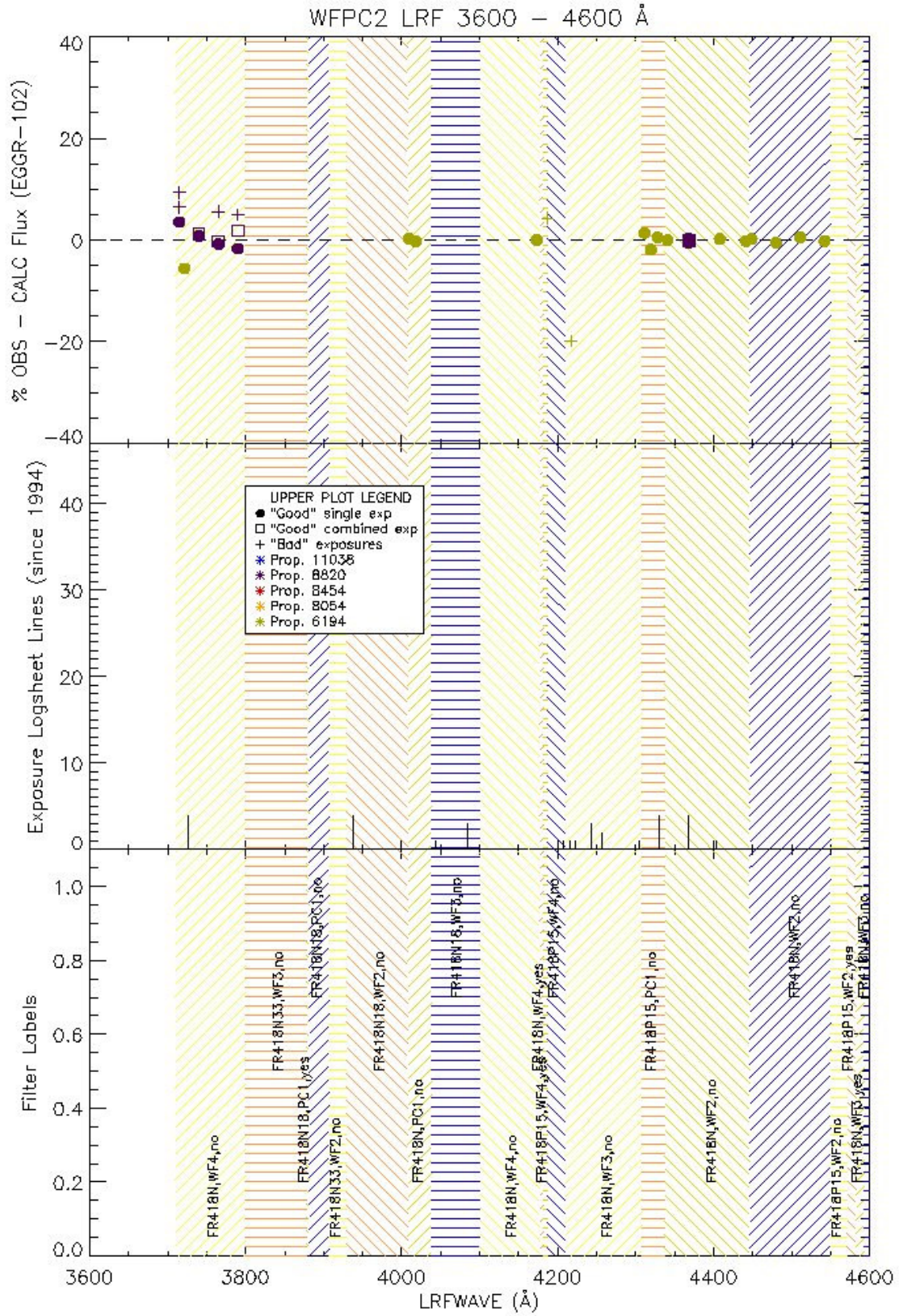


Figure 10: Same as Figure 3 but with corrected SYNPHOT throughput table.

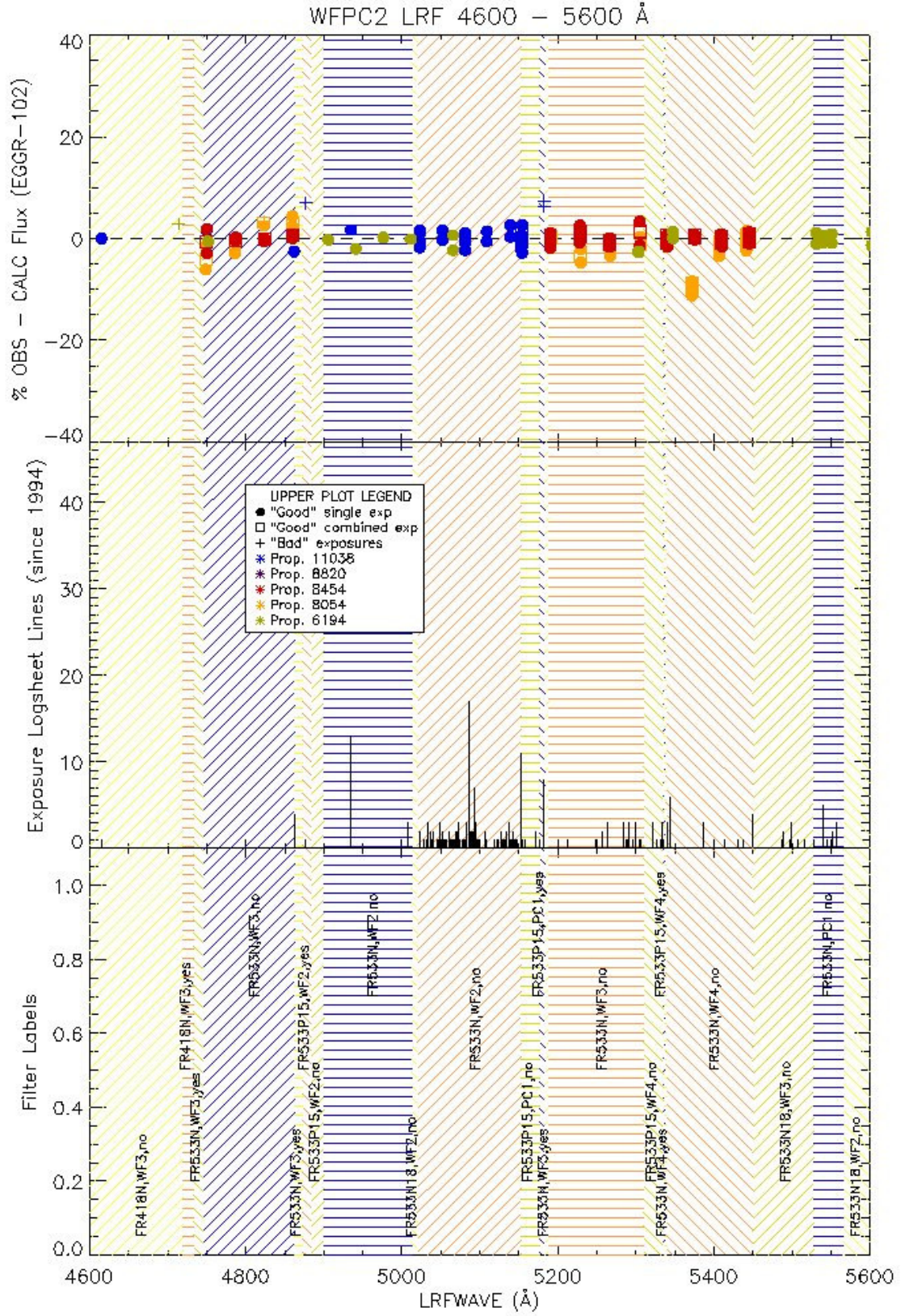


Figure 11: Same as Figure 4 but with corrected SYNPHOT throughput table.

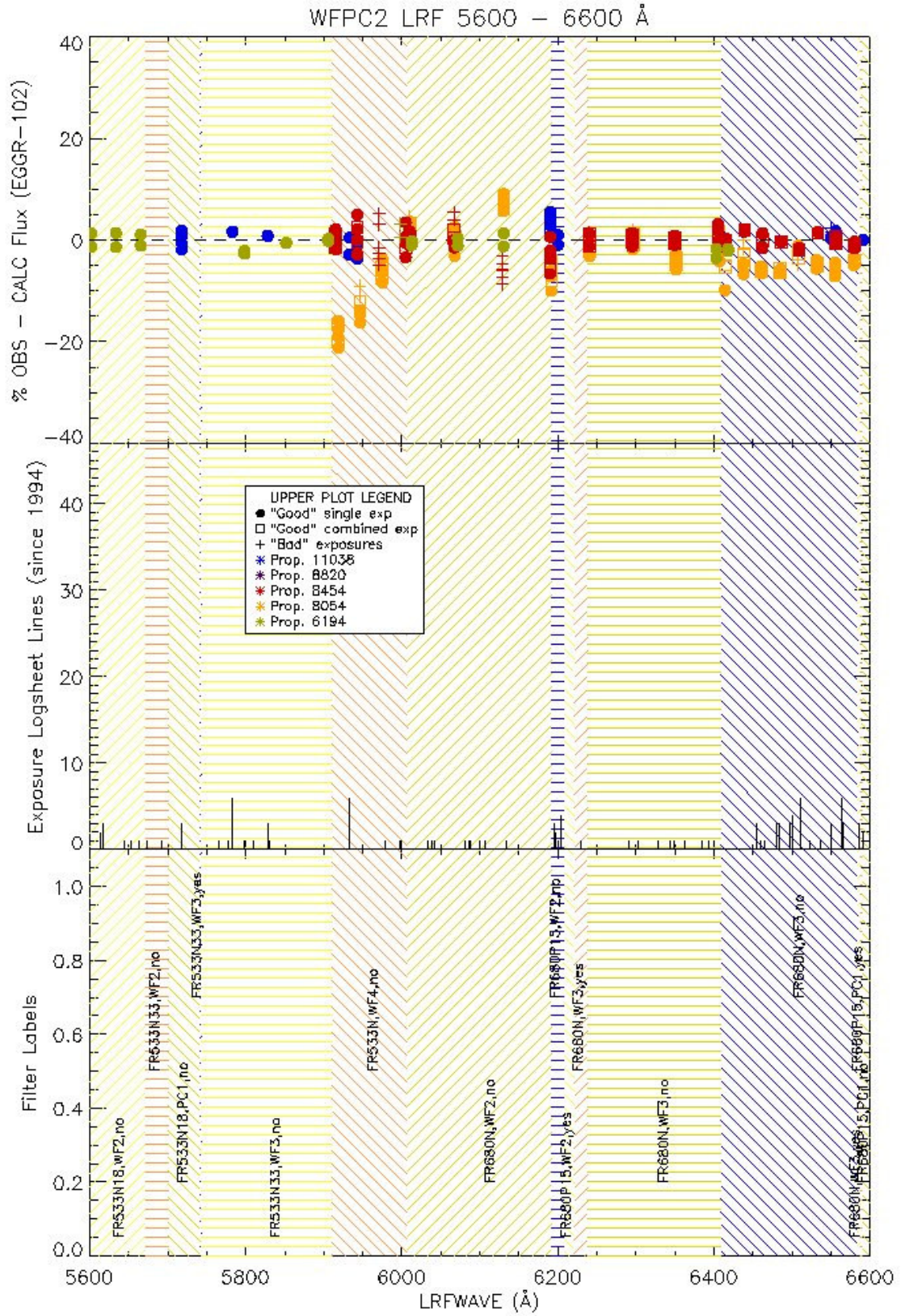


Figure 12: Same as Figure 5 but with corrected SYNPHOT throughput table.

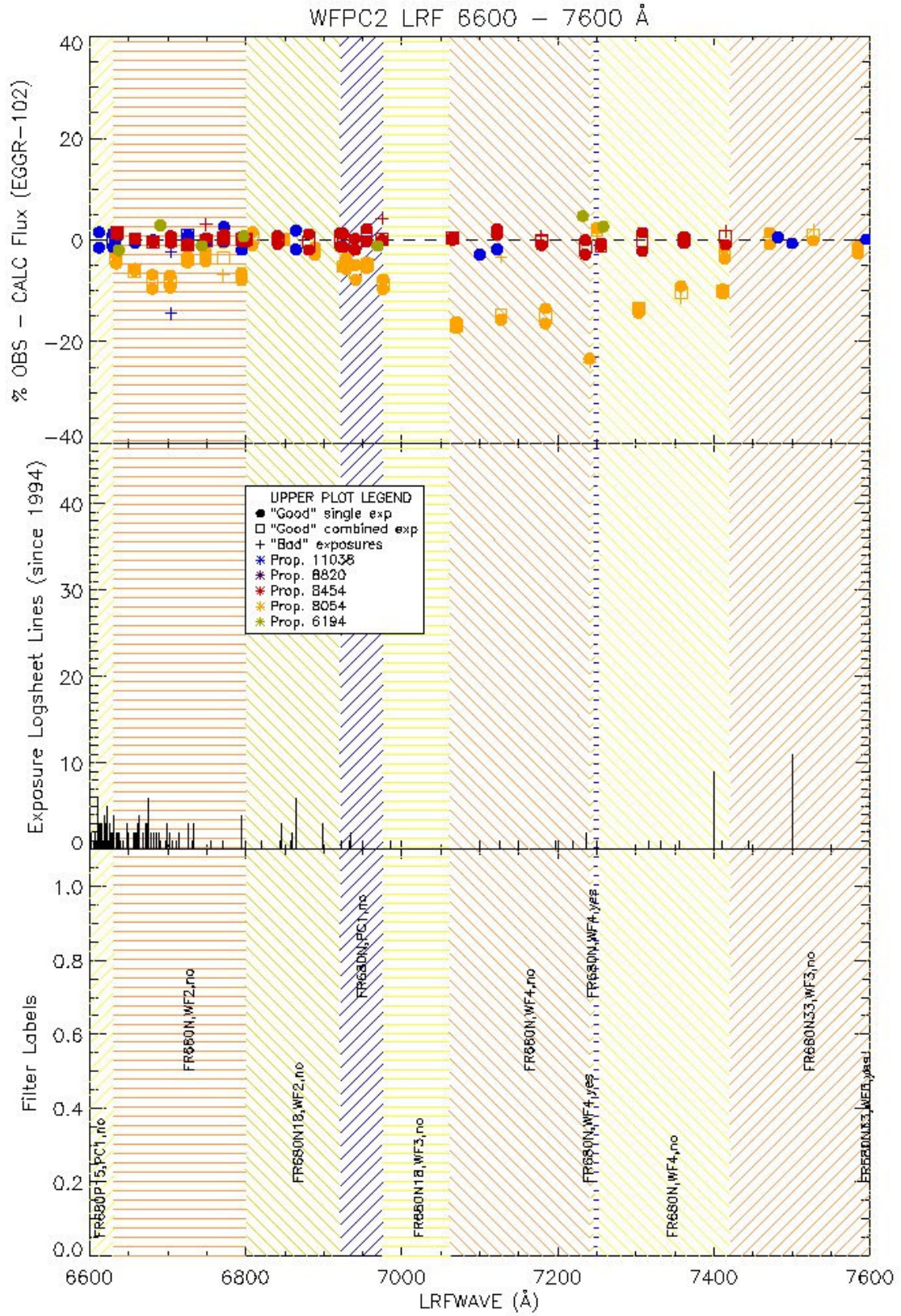


Figure 13: Same as Figure 6 but with corrected SYNPHOT throughput table.

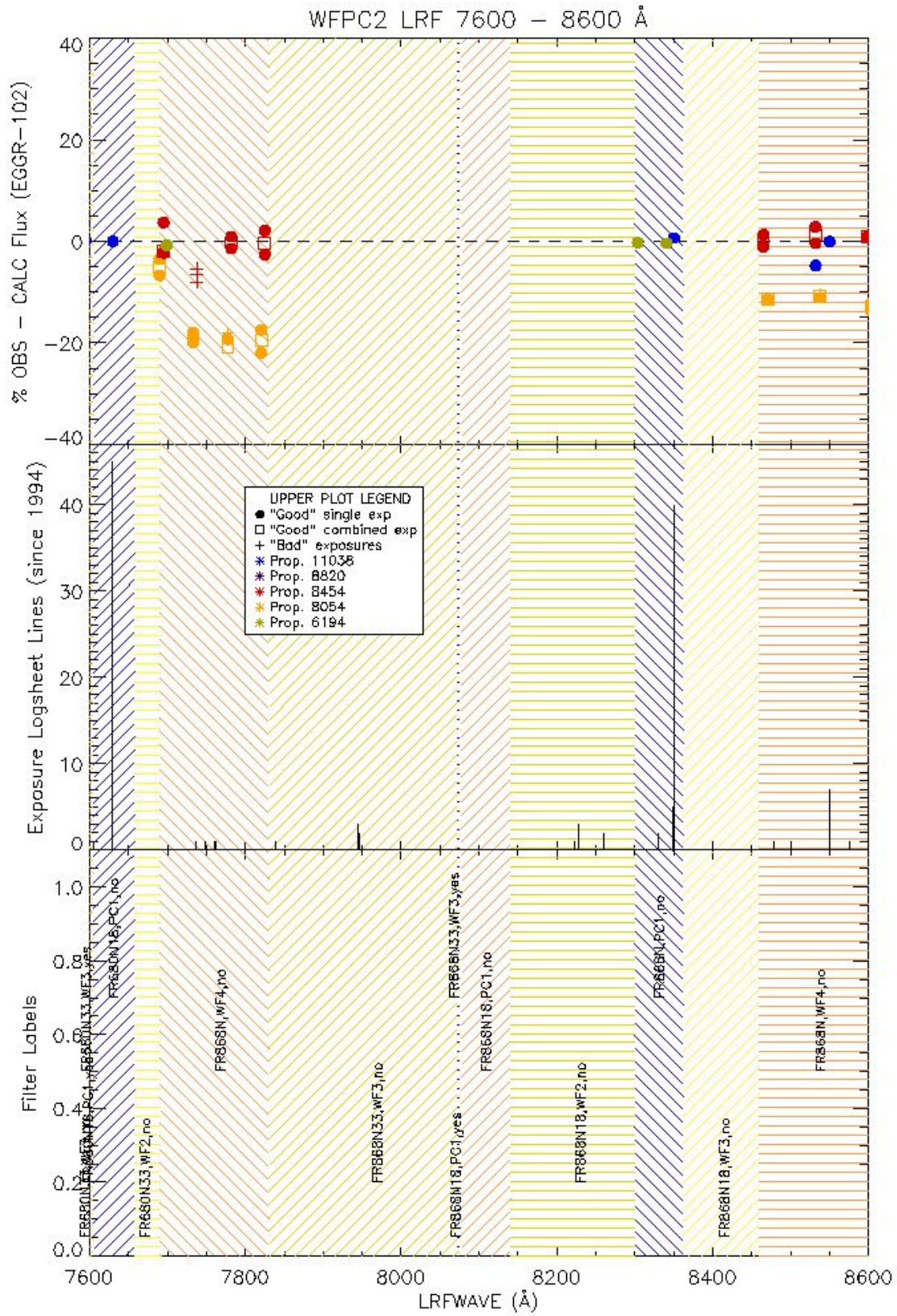


Figure 14: Same as Figure 7 but with corrected SYNPHOT throughput table.

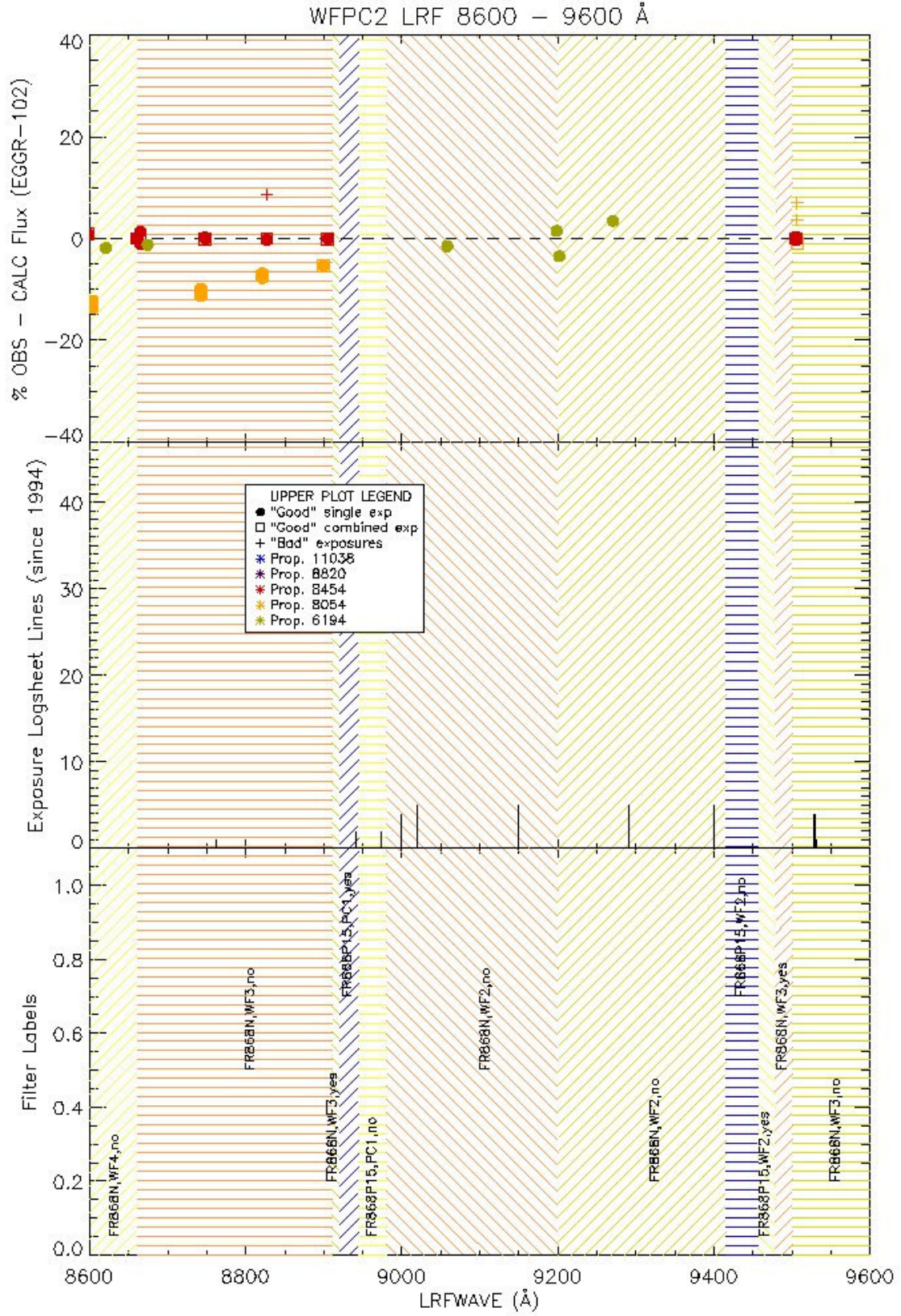
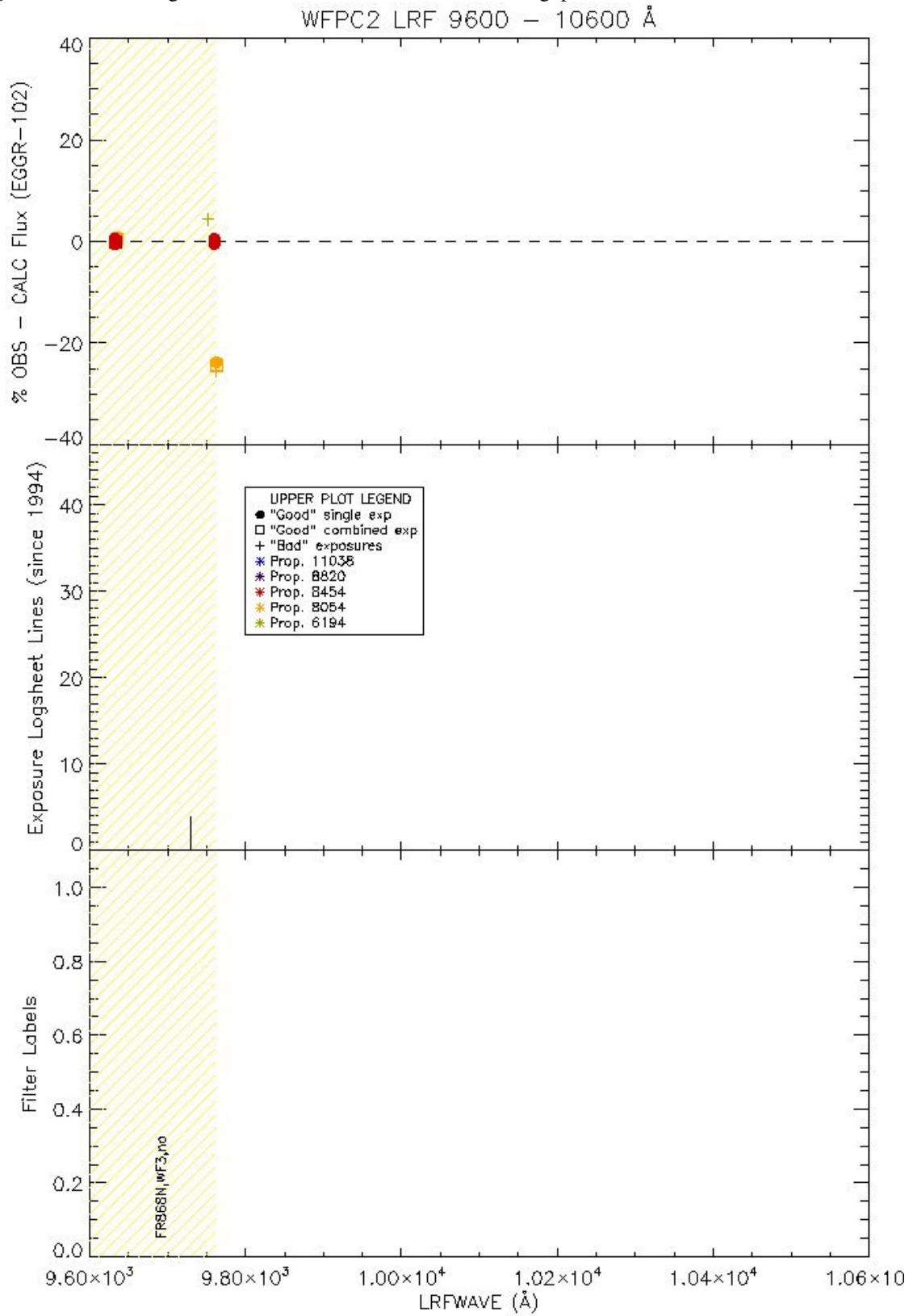


Figure 15: Same as Figure 8 but with corrected SYNPHOT throughput table.



5.2. Delivery to CDBS

We delivered the corrected SYNPHOT LRF throughput table to CDBS, as instructed by CDBS TIR 08-01 (Diaz & Cracraft 2008). In the header, we updated PEDIGREE to be “*INFLIGHT 26/04/1997 07/09/2007.*” We also added HISTORY with the following, “*This table is updated with on-orbit observations. Corrections done by J. Biretta and P. L. Lim (Nov 2008).*” The new throughput table was ingested into CDBS on August 5, 2009, and is designated as *wfpc2_lrf_005_syn.fits*.

6. Future Work

Our calibration observations covered most of the ramp filter wavelengths, especially those most used by observers. However, due to limited resources, there are still some LRF configurations with science observations but no on-orbit calibration data. They are tabulated in Table 3; values for λ_1 , λ_2 , LRF, and CHIP are as in IHB Tables 3.7 and 3.8. The ramp wavelengths and number of Phase II proposal exposure logsheet lines requested by observers are given by λ and N_{\log} , respectively. The number of actual corresponding exposures archived is N_{arc} , which can be larger if there are CR-SPLITS or multiple exposures. We also excluded exposure logsheet lines without corresponding archival data (i.e., unexecuted exposures). The numbers in the table are complete for the entire WFPC2 mission.

SYNPHOT calibrations for these tabulated configurations are still derived from ground-based data and should be used with caution. We have included in the table an estimate of the uncertainty on the ground-based calibration, which takes into account the difference between the ground-based and the on-orbit calibrations at nearby wavelengths on the same LRF physical filter strip. In some cases, the uncertainties are quite small – these are cases where the ground-based calibration proved to be accurate at nearby locations on the same filter strip. In other cases, where there is little or no information, the uncertainties are taken as 20%, which is typical of the largest differences between the ground-based and the on-orbit calibrations. There might be some possibility to improve this situation via post-mission lab studies of the LRFs, but considerable effort would be required to accurately model the effects of the OTA pupil, etc., at the filters.

Both this table and our calibration work herein do not include vignetted LRF configurations (i.e., IHB Table 3.8) because they were rarely used and already have compromised data quality.

Table 3: List of LRF configurations with existing science observations but no on-orbit calibration data. See text for full details.

λ_1	λ_2	LRF	CHIP	λ	N_{\log}	N_{arc}	Uncertainty
3929	4008	FR418N18	WF2	3937.0	4	8	15%
4038	4100	FR418N18	WF3	4044.0	1	4	10%
				4085.0	3	3	20%
4186	4210	FR418P15	WF4	4208.0	1	8	20%
4210	4308	FR418N	WF3	4215.0	1	8	15%
				4223.0	1	8	12%
				4243.0	3	3	10%
				4256.0	2	16	10%
				4305.0	1	8	5%
5310	5335	FR533P15	WF4	5322.0	3	2	7%
				5332.0	1	8	7%
				5333.0	3	2	7%
5450	5528	FR533N18	WF3	5487.7	1	2	3%
				5488.0	2	12	3%
				5498.0	1	8	3%
				5499.0	3	2	3%
				5508.0	1	8	3%
				5515.7	1	2	3%
5671	5700	FR533N33	WF2	5673.0	1	8	3%
				5692.0	1	2	3%
6976	7061	FR680N18	WF3	6984.8	1	2	5%
7830	8072	FR868N33	WF3	7839.7	1	2	5%
				7944.0	3	7	15%
				7946.0	2	4	15%
8140	8300	FR868N18	WF2	8222.9	1	2	20%
				8228.0	3	7	20%
				8260.0	2	2	20%

7. Summary

We found significant discrepancies (up to ~20%) between observed and the predicted count rates for standard star EGGR-102 using the ground-based SYNPHOT LRF throughout table. As a result, we have revised the LRF throughput table using standard star data from four proposals (6140, 8454, 8820, and 11038) taken over a ten-year period. The new SYNPHOT LRF throughput table is designated *wfpc2_lrf_005_syn.fits* and has been delivered to CDBS.

The accuracy of our revised calibration is expected to be ~2% for most wavelengths. There are some wavelengths, noted in Section 5.1, where the scarcity of on-orbit calibration data and the potential for rapid variations with wavelength reduce the accuracy to 5-10%; approximately 80 of the ~1500 LRF science images fall into this category.

We have made an effort to calibrate throughputs for as many of the LRF science exposures as reasonably possible. However, due to limitations on the HST time available for calibration, some of the least-used LRF configurations were not directly calibrated on-orbit. Instead these will need to rely on calibrations at nearby wavelengths, or rely on the ground-based calibration. The ~148 exposures with no on-orbit calibration have been tabulated along with an estimate of the expected uncertainty; these range from 3-20%, depending on the constraints available from on-orbit data at nearby wavelengths. It might be possible to

improve the situation with post-mission laboratory tests on the LRFs, though considerable effort would be needed to correctly model the effects related to the OTA pupil size, etc.

8. Epilogue

Subsequent to the analyses herein, new calibrations were obtained for the standard star EGGR-102 (Bohlin, private communication). Herein we have used the reference spectrum *grw_70d5824_stis_001.fits* whereas the more recent spectrum *grw_70d5824_stisnic_002.fits* is ~1% fainter (~2% fainter at blue wavelengths). In addition, new calibrations of the time-dependent throughput variations in WFPC2 were recently derived (Gonzaga, et al., in preparation). We have repeated representative portions of our analyses with the new information, and here describe the changes that would result. At most wavelengths the change in the predicted LRF count rates is less than 1%, and hence is small compared to other errors and uncertainties in our analyses (~2% or more). At wavelengths between 3800 Å and 5000 Å the new information would reduce the predicted counts for EGGR-102 by about 2%, and hence imply a throughput for the LRF filters that is about 2% higher than our final results. This would appear to impact 28 WFPC2 LRF science exposures falling into this wavelength range. Short-ward of 3800 Å the effect increases to 4%, and hence implying LRF filter throughputs about 4% higher than our final results (this impacts only 4 WFPC2 exposures). Our final results were used to generate the LRF filter throughput table *wfpc2_lrf_005_syn.fits* which was subsequently used to reprocess the WFPC2 archive during late 2009. Neither the throughput table, nor the reprocessed WFPC2 archival data, are corrected for the new information. A total of 32 WFPC2 LRF science exposures are potentially affected by the new information.

Acknowledgements

We thank Ms. Diane Karakla for providing us with the extremely helpful science logsheet tallies of LRFs from 1994 to 2008. In addition, we extend our gratitude to Dr. Chris O'Dea, Dr. Keith Noll, Dr. James Rhoads, and Dr. Brad Whitmore, who worked on early calibrations of the LRFs. We are also grateful to Dr. Van Dixon and Dr. Ralph Bohlin, who provided insightful feedbacks.

References

- Anderson, J., & King, I. R. 1999, PASP, 111, 1095
- Baggett, S., et al. 2002, in HST WFPC2 Data Handbook, v. 4.0, ed. B. Mobasher, Baltimore, STScI

- Biretta, J., Baggett, S., & Noll, K. 1996, “Photometric Calibration of WFPC2 Linear Ramp Filter Data in SYNPHOT,” WFPC2 Instrument Science Report 96-06
- Biretta, J., & Gonzaga, S. 2005, “Early Assessment of the WF4 Anomaly,” WFPC2 Instrument Science Report 05-02
- Biretta, J., & Lim, P. L. 2009, “Wavelength Stability of the WFPC2 Narrow Band and Linear Ramp Filters,” WFPC2 Instrument Science Report 09-04
- Diaz, R. I., & Cracraft, M. 2008, “Assessment and Delivery of Reference Files,” CDBS Technical Instrument Report 08-01
- Dolphin, A. E. 2004, WFPC2 Calibration and CTE Correction Updates (December 2004), http://purcell.as.arizona.edu/wfpc2_calib/2004_12_20.html
- Gonzaga, S. 2002, WFPC2 Data Analysis: A Tutorial, version 3.0, (Baltimore, STScI)
- Gonzaga, S., Baggett, S., & Biretta, J. 2001, “Preliminary Assessment of the FR533N Filter Anomaly,” WFPC2 Instrument Science Report 01-04
- Holtzman, J., et al. 1995, PASP, 107, 156
- Koekemoer, A. M., Biretta, J., & Mack, J. 2002, “Updated WFPC2 Flatfield Reference Files for 1995 – 2001,” WFPC2 Instrument Science Report 02-02
- Landolt, A. U., & Uomoto, A. K. 2007, AJ, 133, 768
- Lim, P. L., & Biretta, J. 2009, “Bandwidth Stability of the WFPC2 Narrow Band and Linear Ramp Filters,” WFPC2 Instrument Science Report 09-05
- McMaster, M., Biretta, J., et al. 2008, WFPC2 Instrument Handbook, Version 10.0 (Baltimore: STScI)
- Perryman, M. A. C., et al. 1997, A&A, 323, L49

Appendix A: Throughput Correction Coefficients.

As discussed in Section 5.1, we visually determined the best polynomial function to fit the percentage differences between observed and predicted count rates for each ramp wavelength region in order to obtain the corresponding correction factors for the SYNPHOT throughput table. When there is only one data point available in the region, its value is taken as the coefficient A_0 ; if two data points, then their mean value is used. The best-fit functions are as shown in Figure A1 to Figure A37, which correspond to Table 2 – Some figures cover multiple rows in the table. The plot title labels the ramp filter name, chip, and vignetting information. Dotted vertical lines mark the region boundaries, where $\lambda_1 < \text{LRFWAVE} \leq \lambda_2$. Each figure has top and bottom panels, as explained below.

Top panel: Differences between observed and predicted count rates. It is equivalent to the top panels in Figure 2 to Figure 8, zooming in the corresponding colored regions. The dashed red line is the fitted polynomial as defined in Equation 1.

Bottom panel: Number of science exposure logsheet lines from 1994 to 2008 (Karakla 2008; private communications), similar to the middle panels in Figure 2 to Figure 8. However, the tallies here are binned across 10 \AA , instead of the exact ramp wavelength, for visual clarity. The number of each tally is also labeled in the histogram bar.

Figure A1: Fitted polynomial(s) across the difference between observed and predicted fluxes. Science observation tallies are also shown. See text for full details.

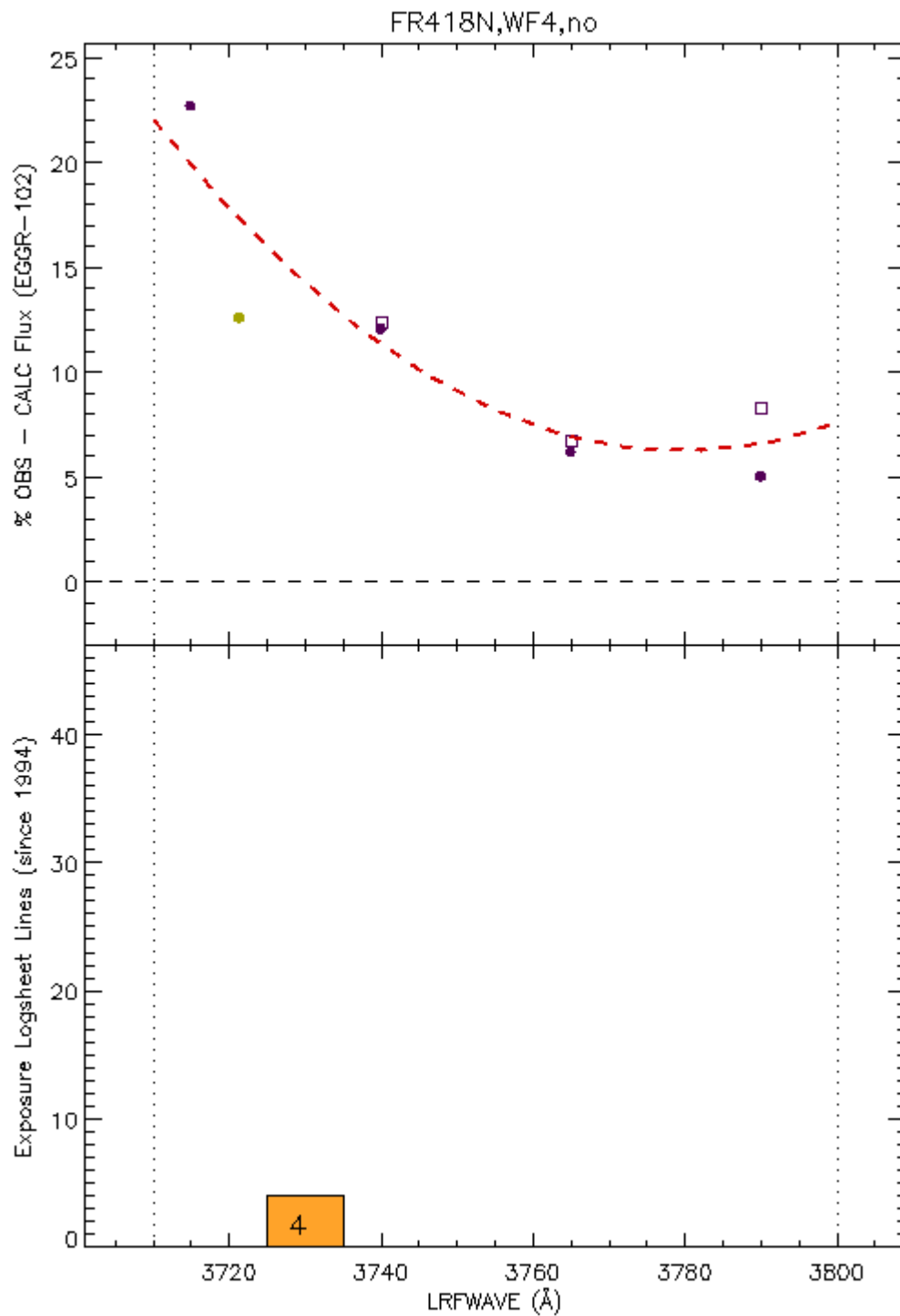


Figure A2: Fitted polynomial(s) across the difference between observed and predicted fluxes. Science observation tallies are also shown. See text for full details.

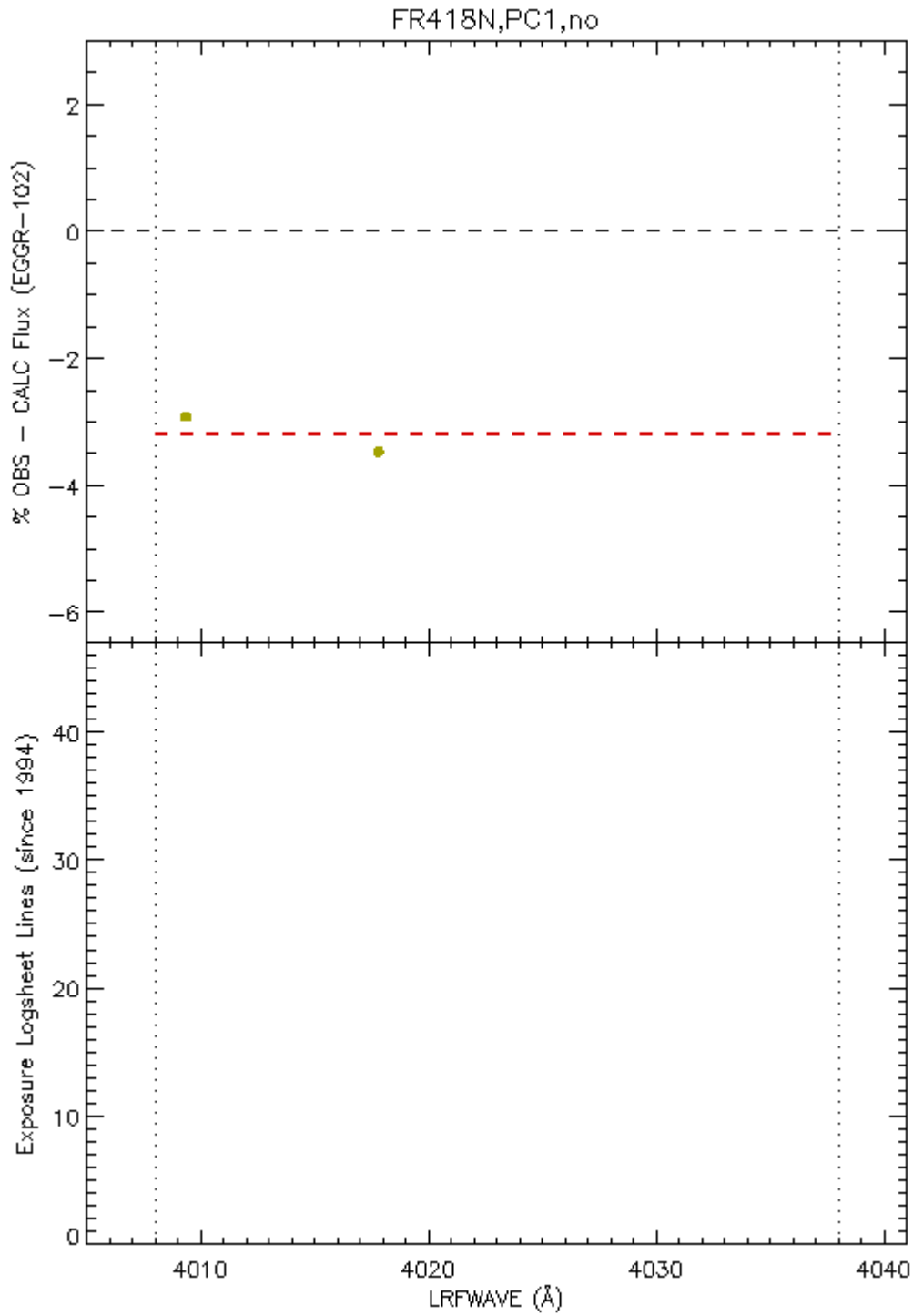


Figure A3: Fitted polynomial(s) across the difference between observed and predicted fluxes. Science observation tallies are also shown. See text for full details.

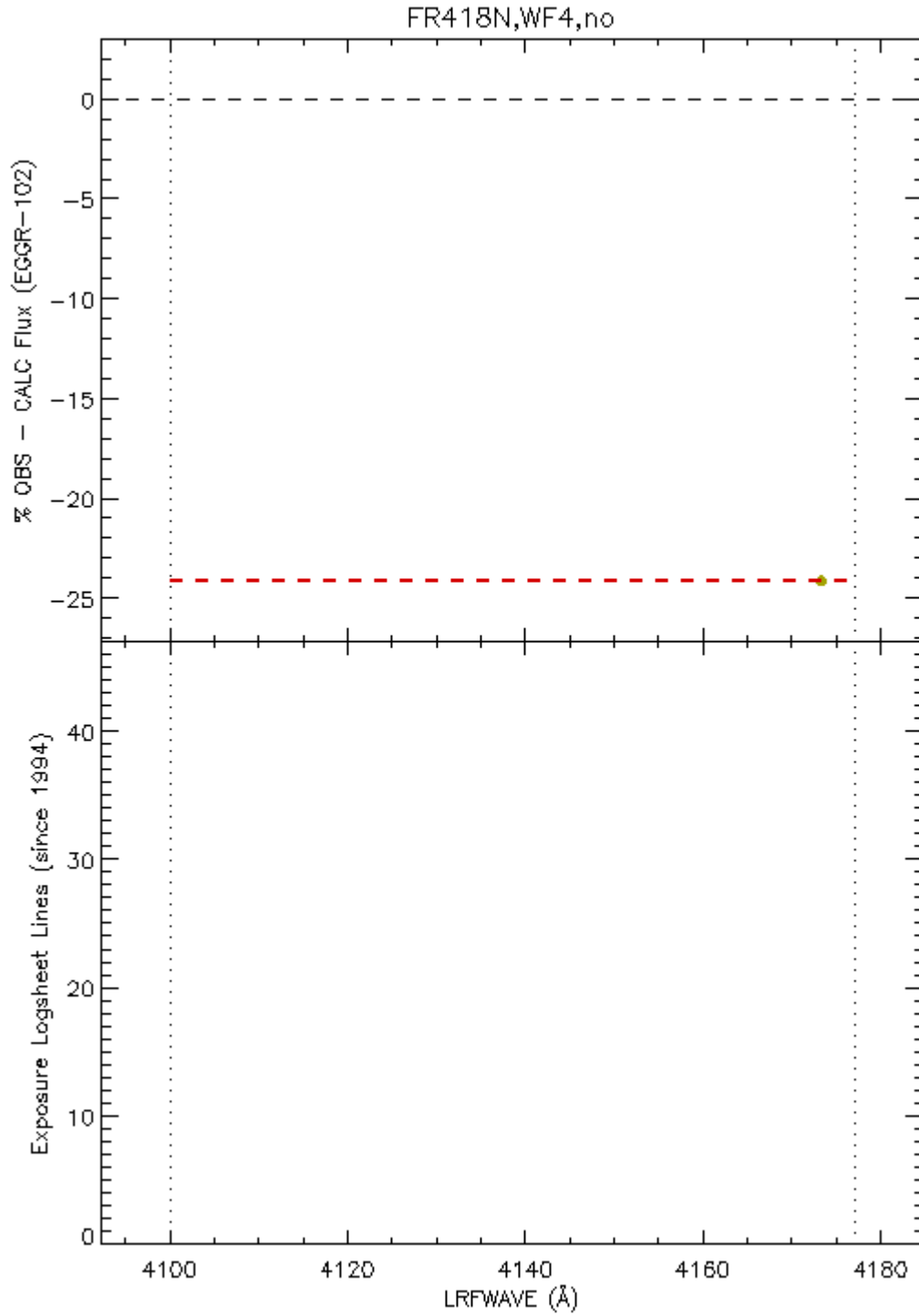


Figure A4: Fitted polynomial(s) across the difference between observed and predicted fluxes. Science observation tallies are also shown. See text for full details.

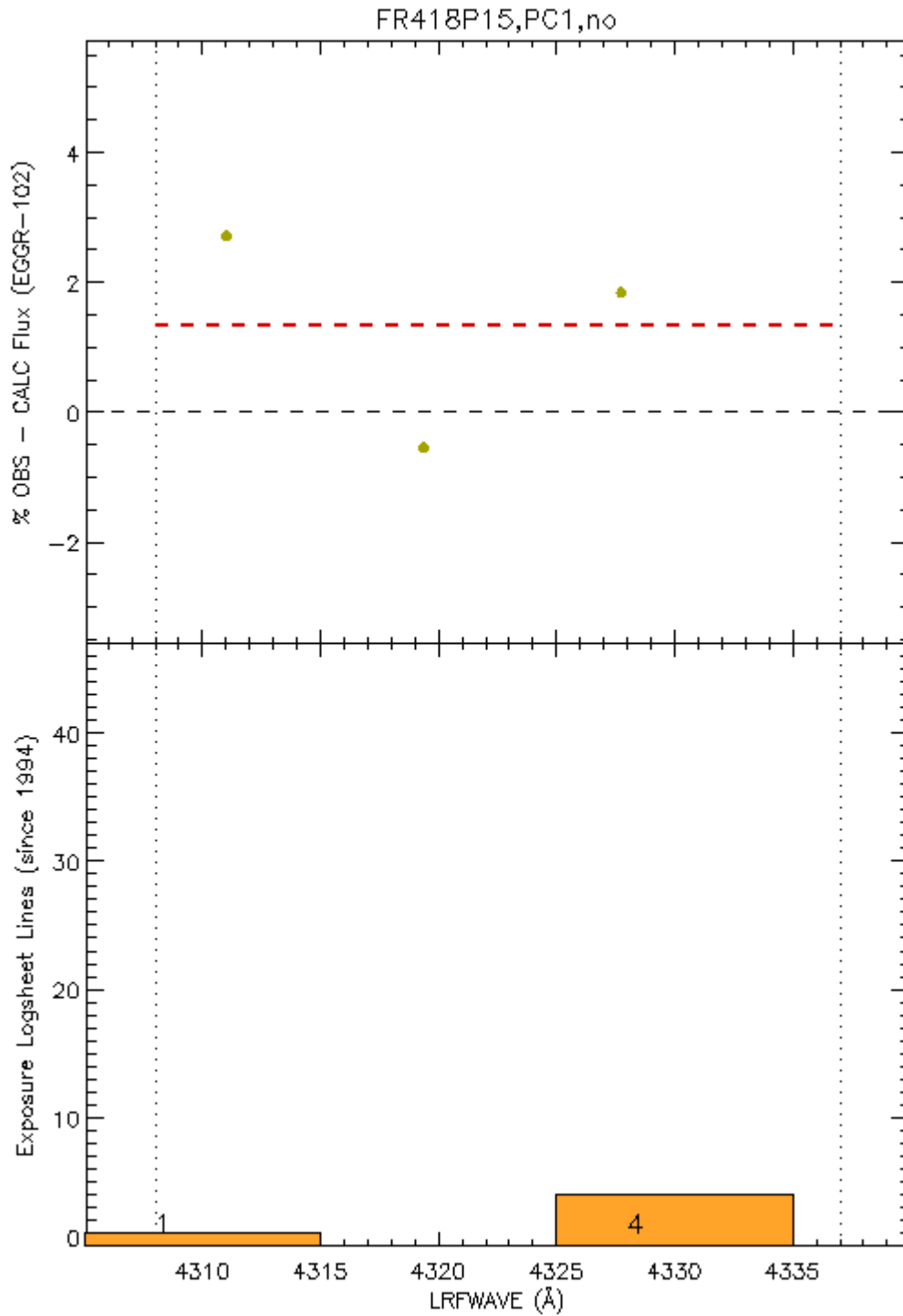


Figure A5: Fitted polynomial(s) across the difference between observed and predicted fluxes. Science observation tallies are also shown. See text for full details.

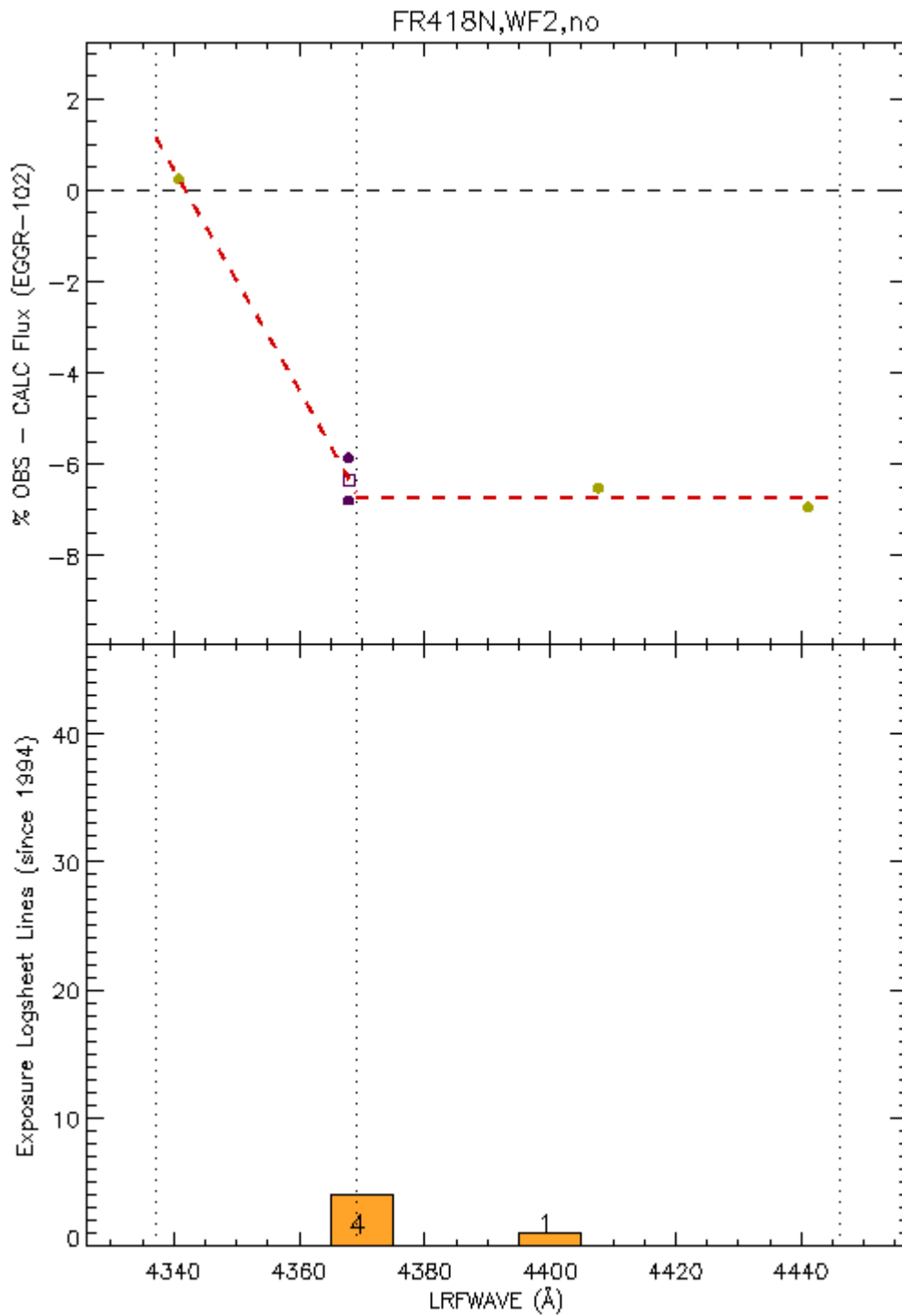


Figure A6: Fitted polynomial(s) across the difference between observed and predicted fluxes. Science observation tallies are also shown. See text for full details.

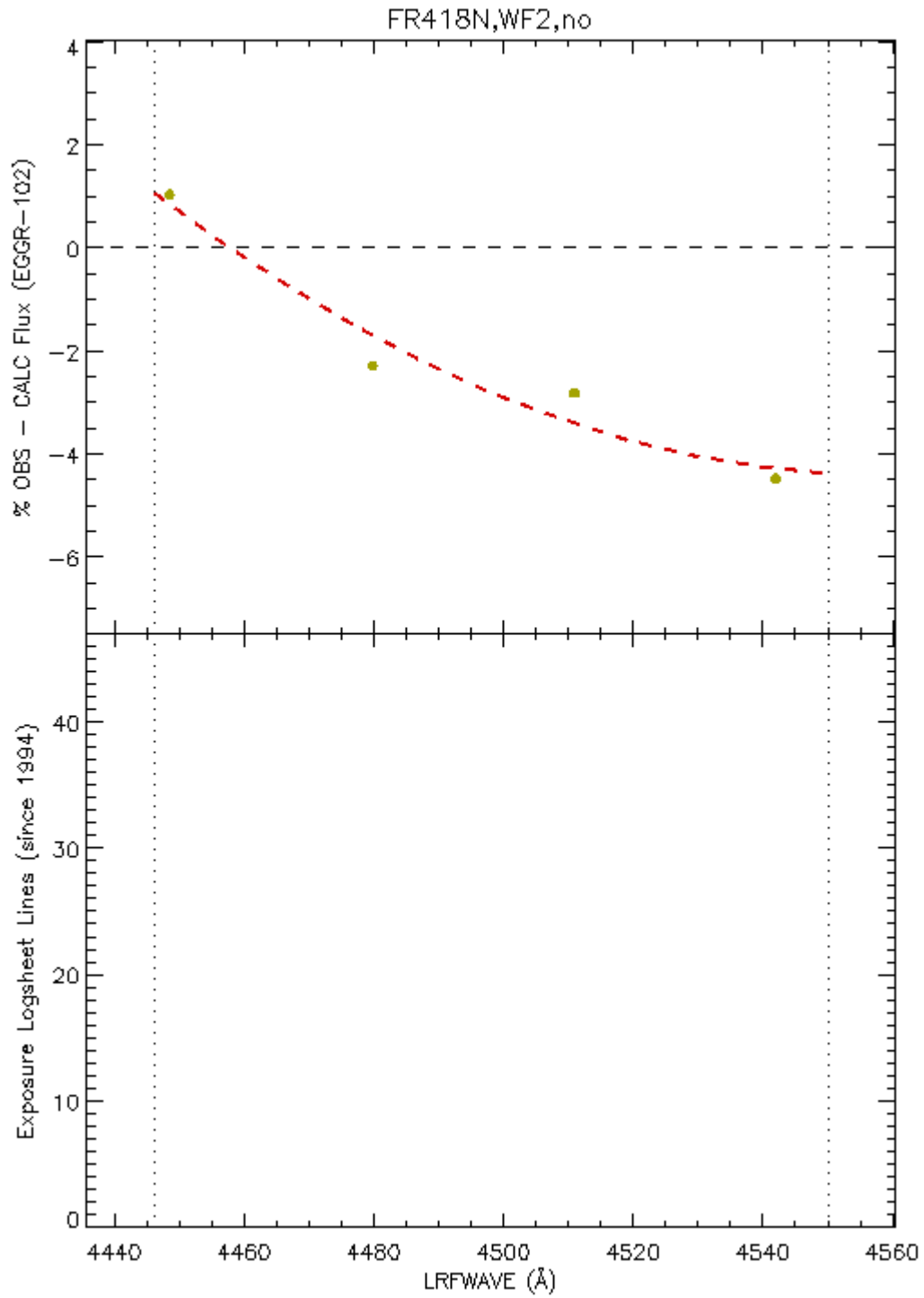


Figure A7: Fitted polynomial(s) across the difference between observed and predicted fluxes. Science observation tallies are also shown. See text for full details.

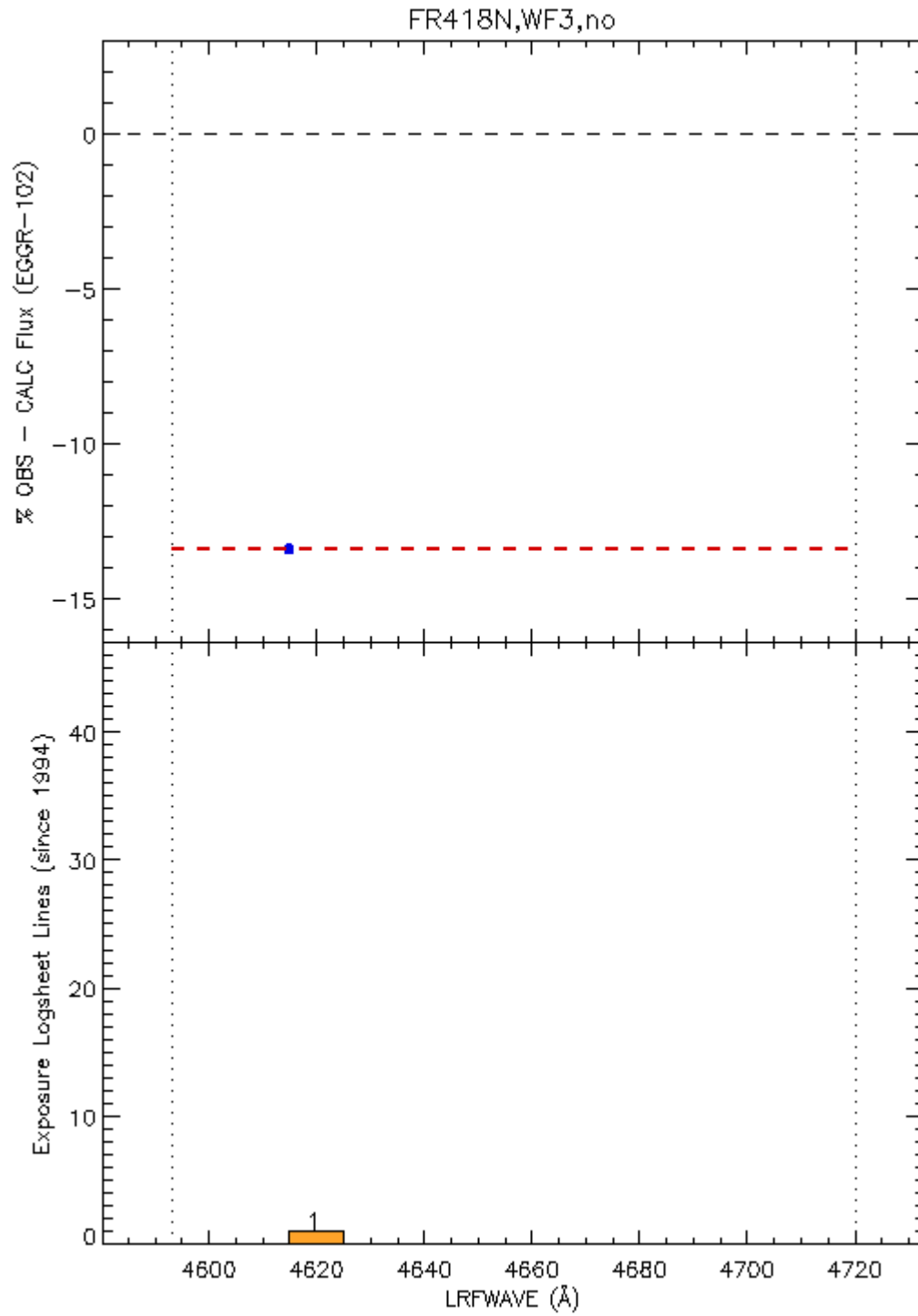


Figure A8: Fitted polynomial(s) across the difference between observed and predicted fluxes. Science observation tallies are also shown. See text for full details.

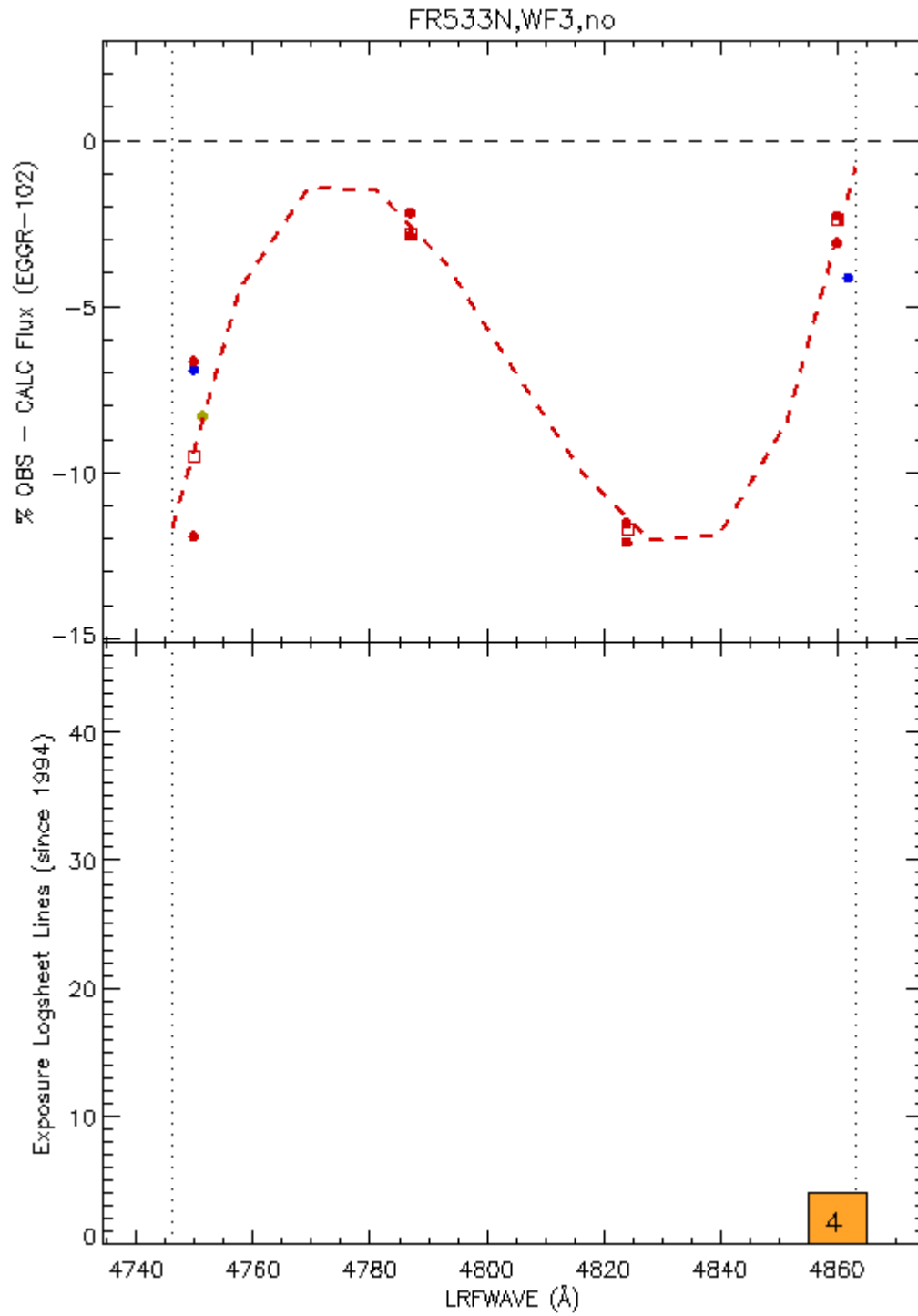


Figure A9: Fitted polynomial(s) across the difference between observed and predicted fluxes. Science observation tallies are also shown. See text for full details.

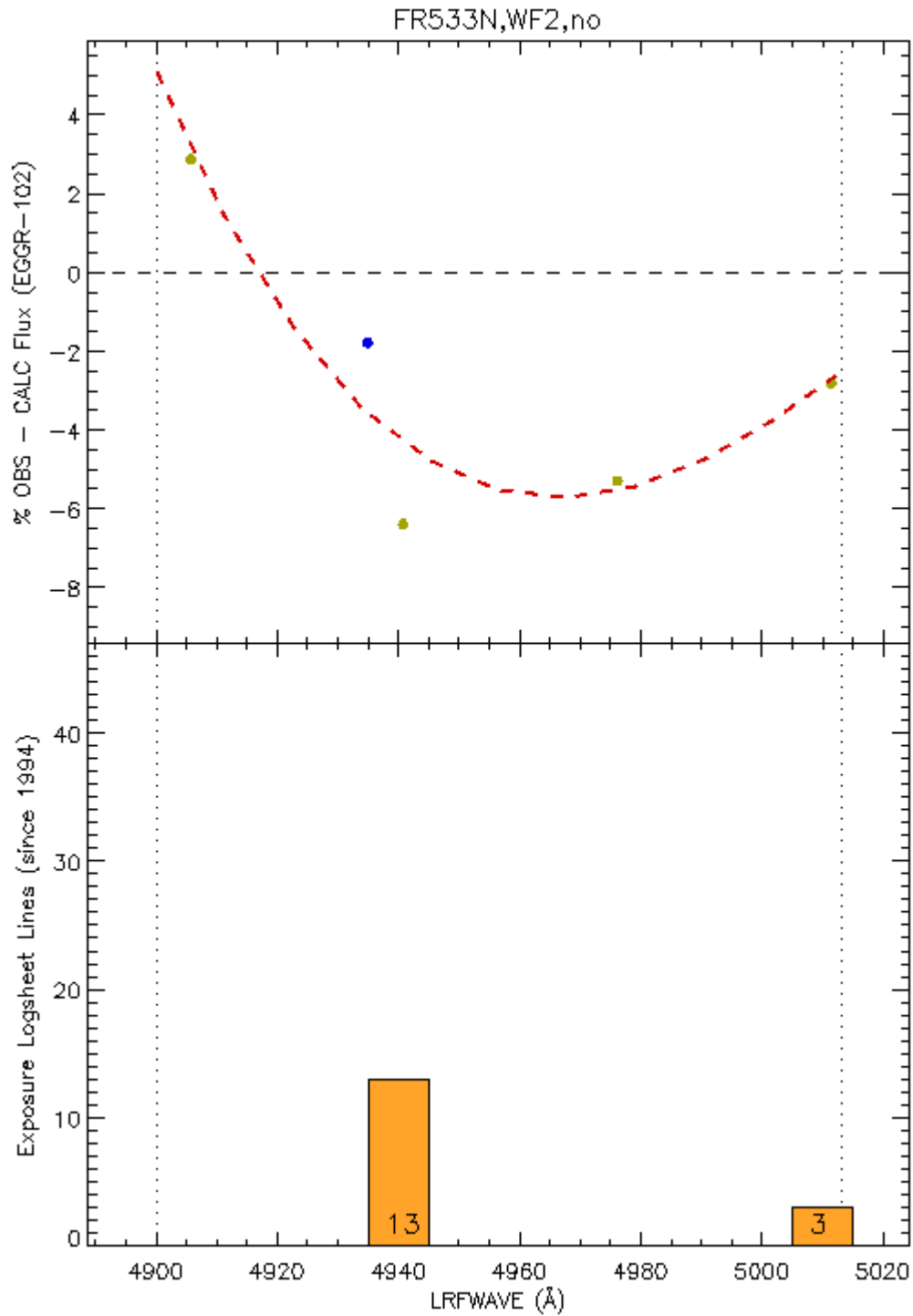


Figure A10: Fitted polynomial(s) across the difference between observed and predicted fluxes. Science observation tallies are also shown. See text for full details.

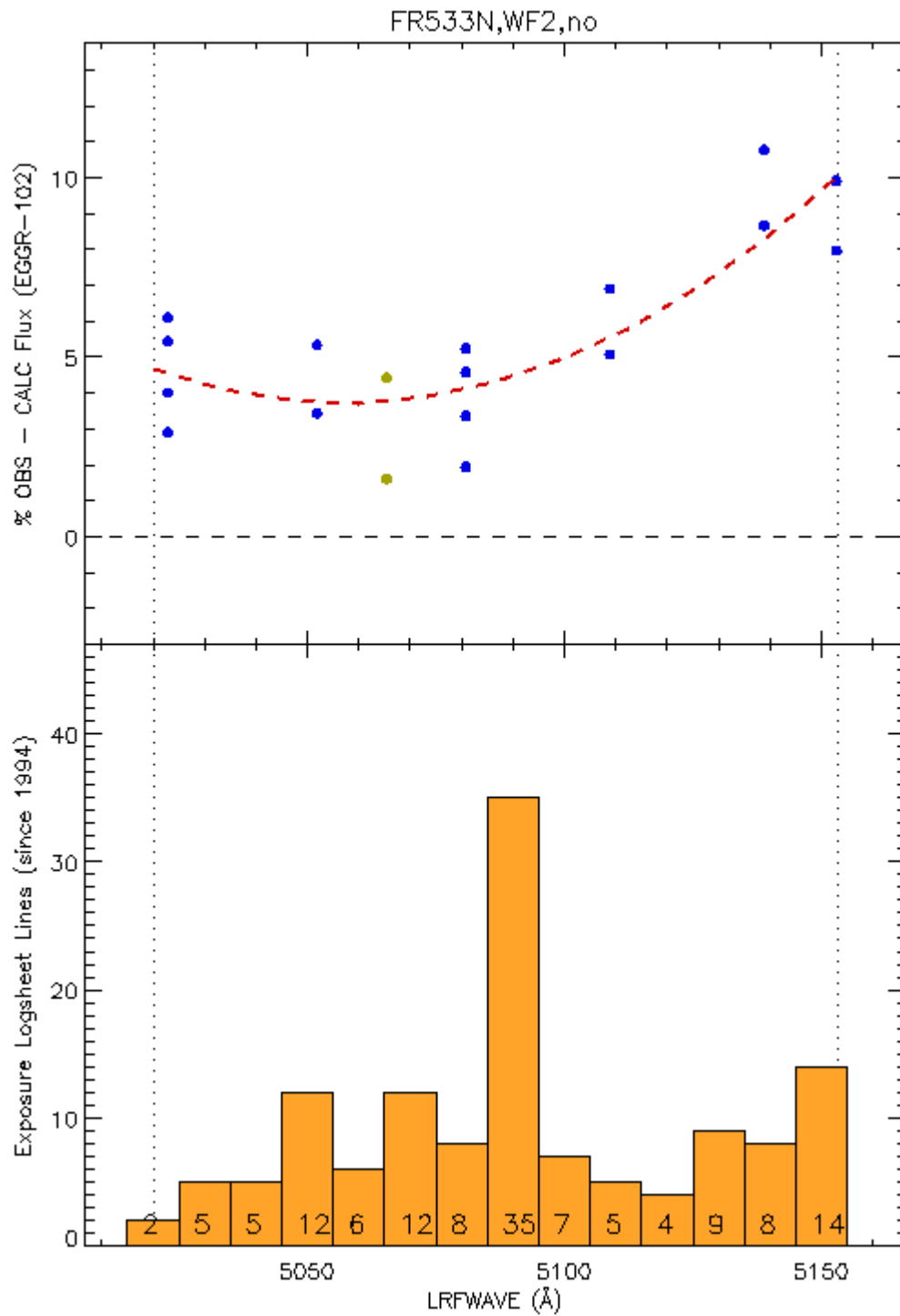


Figure A11: Fitted polynomial(s) across the difference between observed and predicted fluxes. Science observation tallies are also shown. See text for full details.

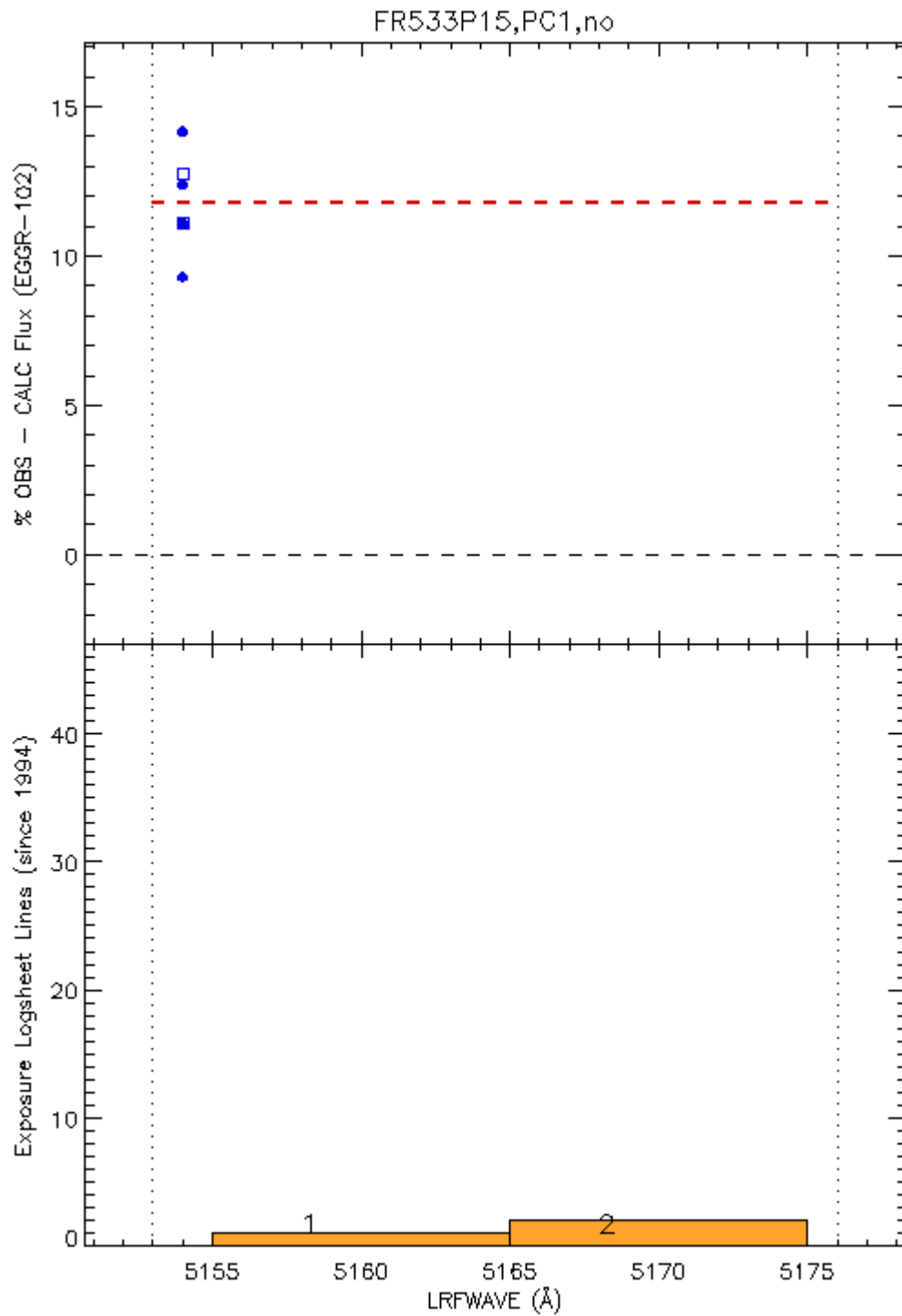


Figure A12: Fitted polynomial(s) across the difference between observed and predicted fluxes. Science observation tallies are also shown. See text for full details.

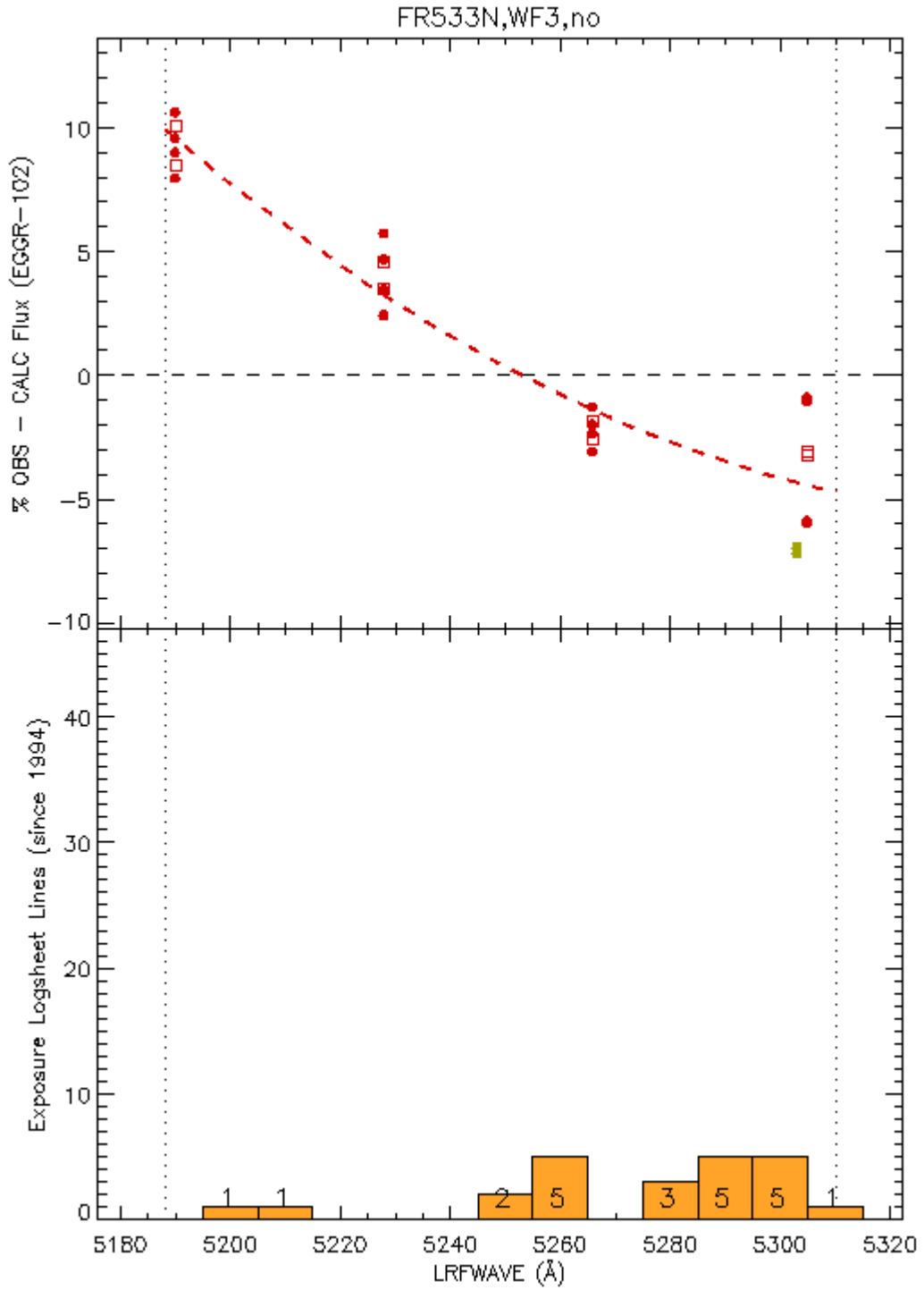


Figure A13: Fitted polynomial(s) across the difference between observed and predicted fluxes. Science observation tallies are also shown. See text for full details.

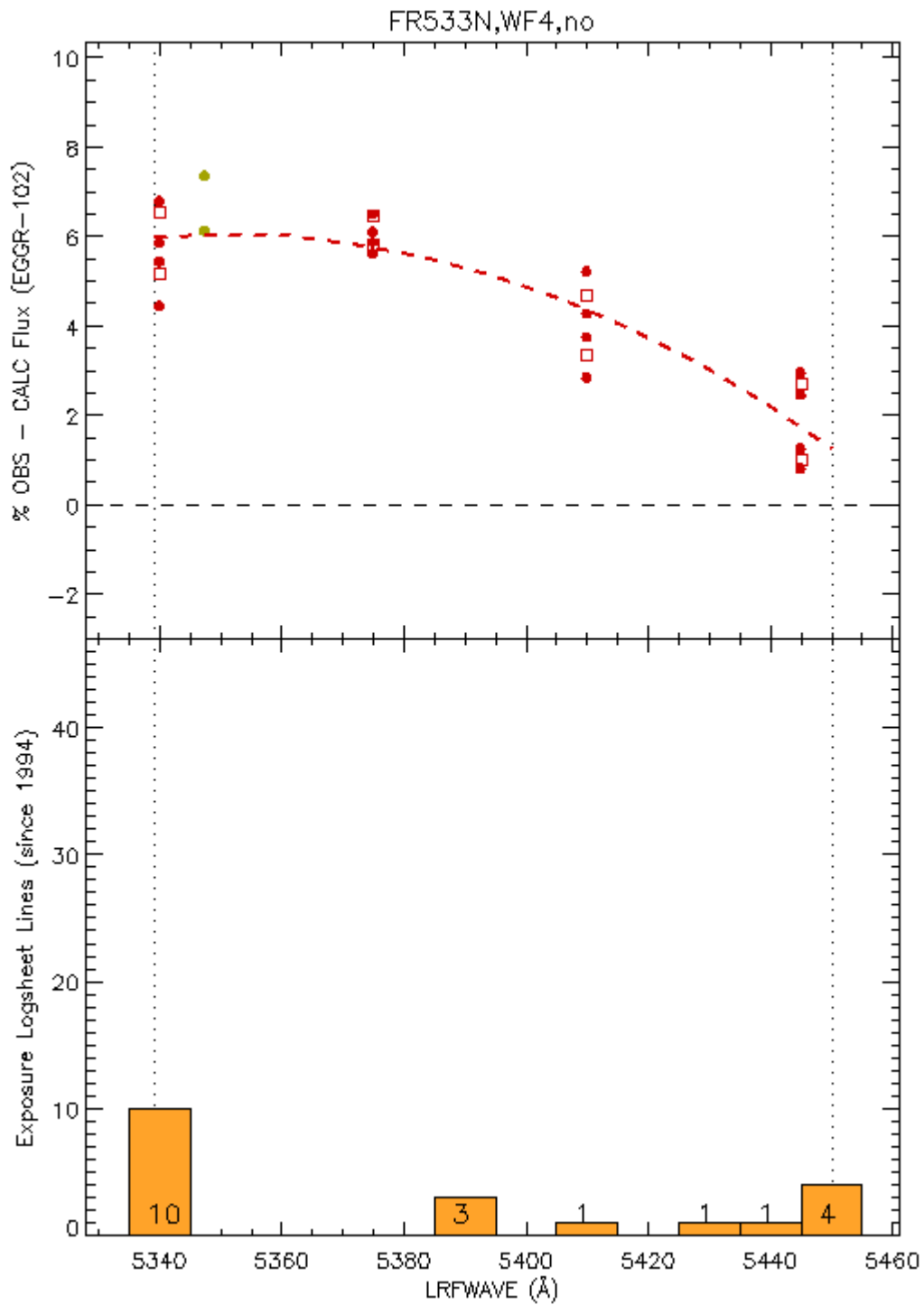


Figure A14: Fitted polynomial(s) across the difference between observed and predicted fluxes. Science observation tallies are also shown. See text for full details.

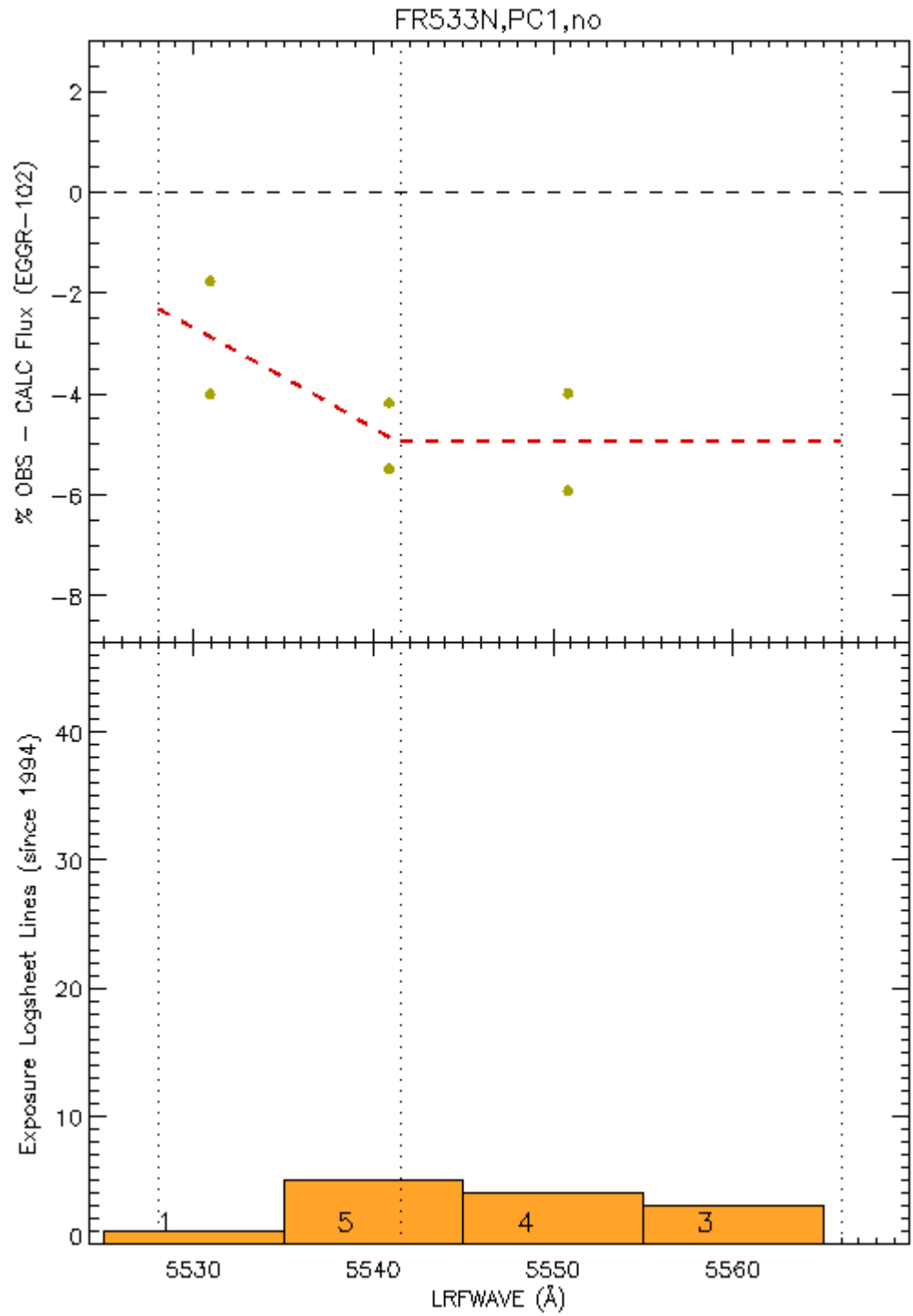


Figure A15: Fitted polynomial(s) across the difference between observed and predicted fluxes. Science observation tallies are also shown. See text for full details.

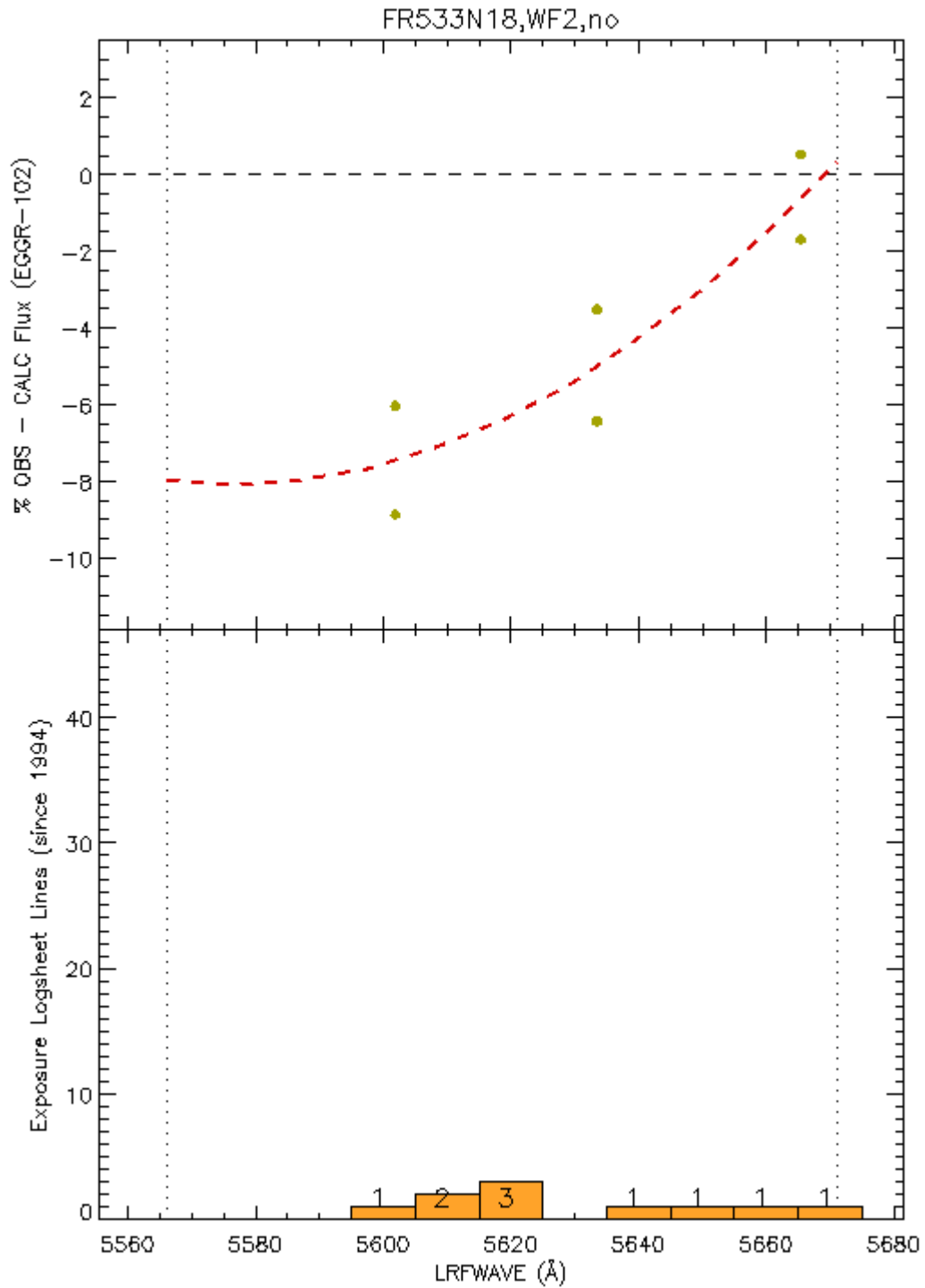


Figure A16: Fitted polynomial(s) across the difference between observed and predicted fluxes. Science observation tallies are also shown. See text for full details.

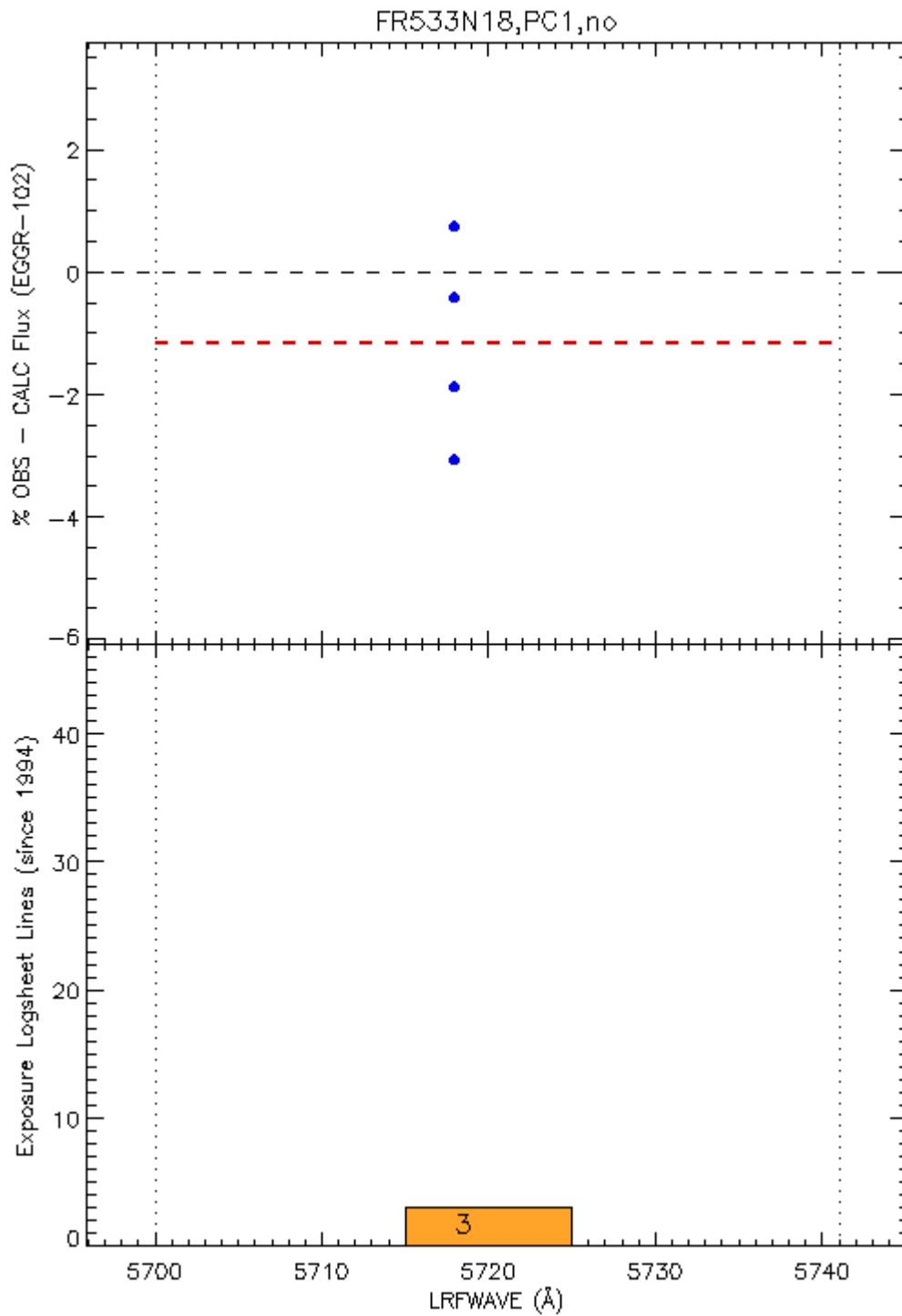


Figure A17: Fitted polynomial(s) across the difference between observed and predicted fluxes. Science observation tallies are also shown. See text for full details.

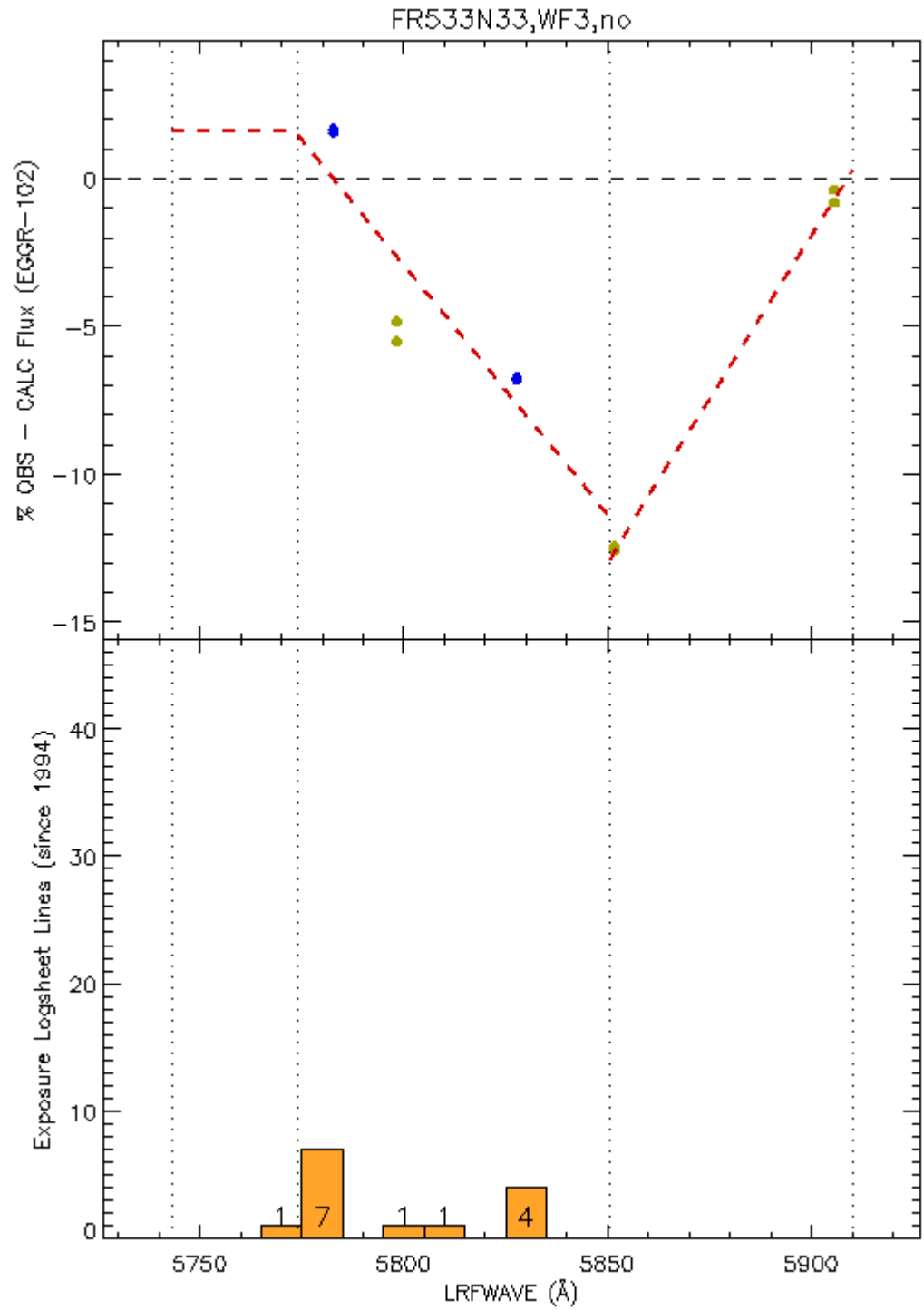


Figure A18: Fitted polynomial(s) across the difference between observed and predicted fluxes. Science observation tallies are also shown. See text for full details.

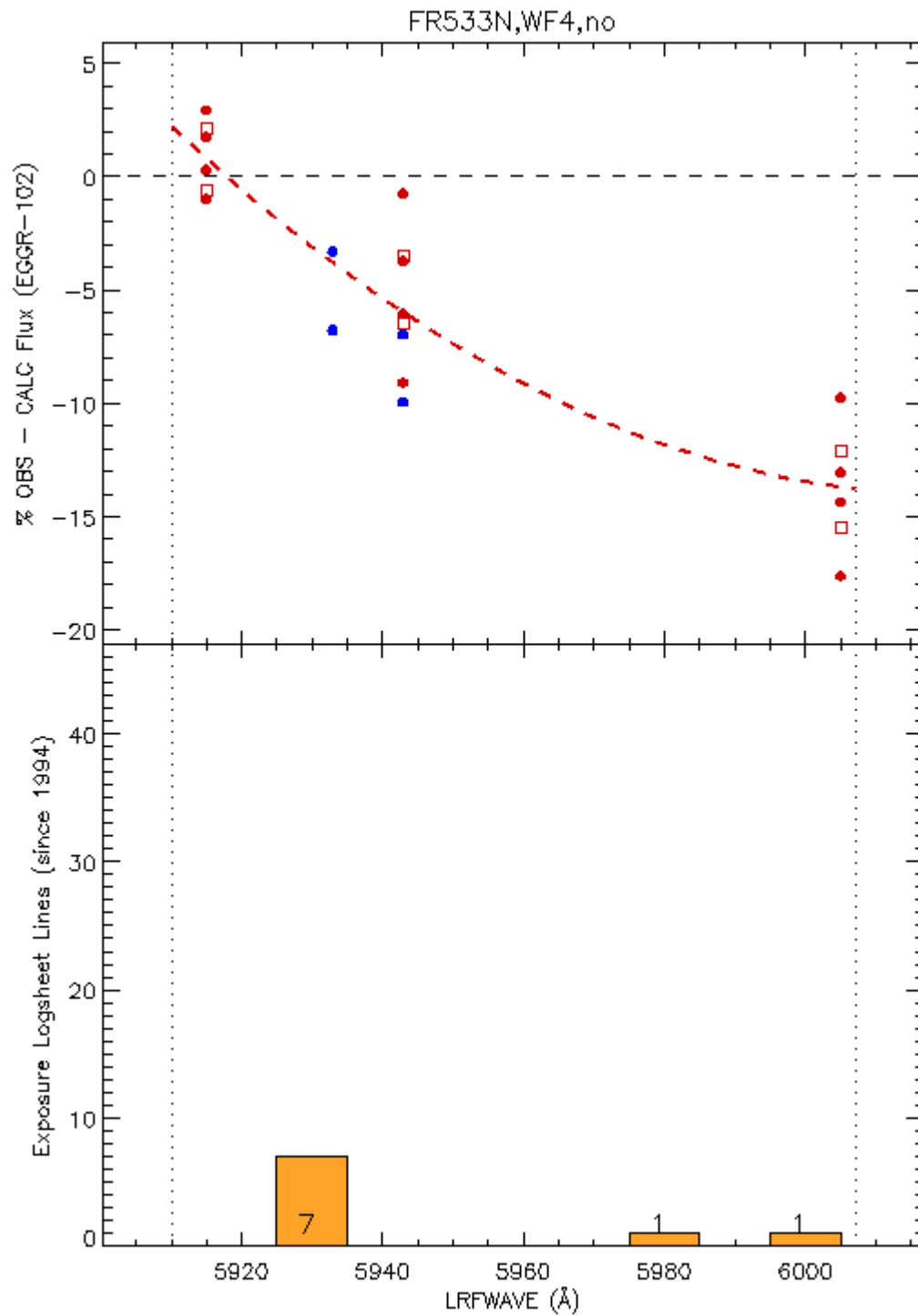


Figure A19: Fitted polynomial(s) across the difference between observed and predicted fluxes. Science observation tallies are also shown. See text for full details.

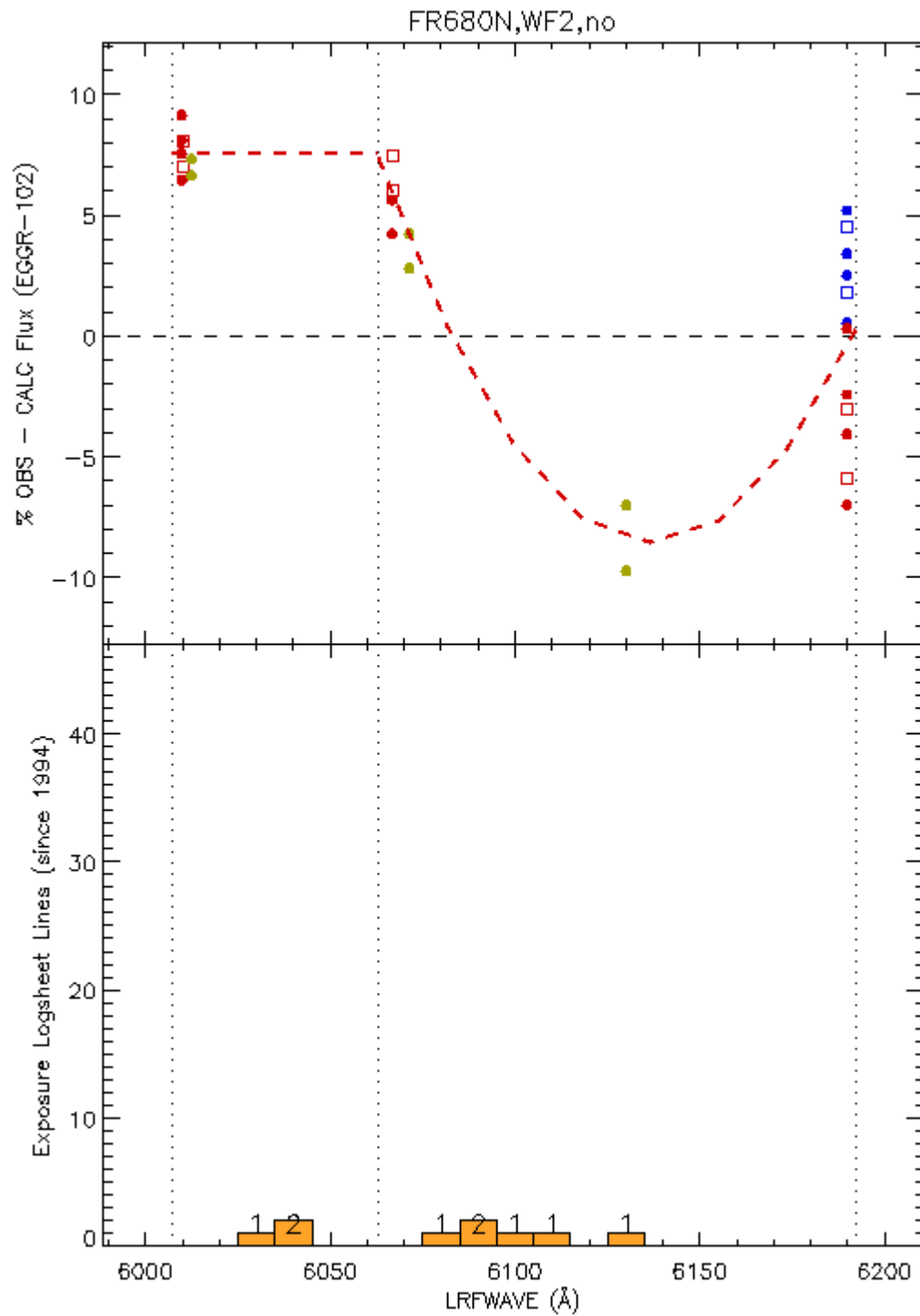


Figure A20: Fitted polynomial(s) across the difference between observed and predicted fluxes. Science observation tallies are also shown. See text for full details.

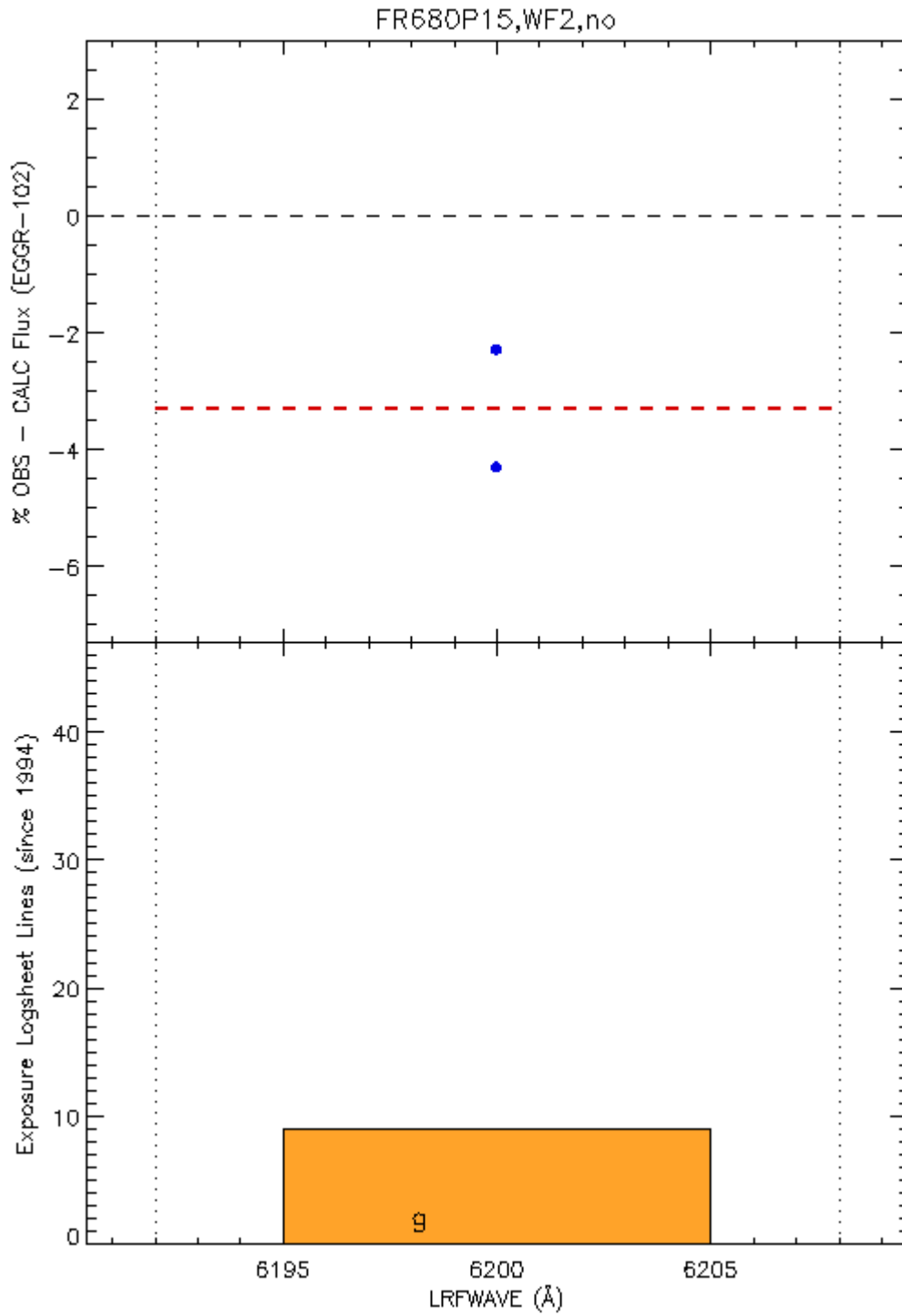


Figure A21: Fitted polynomial(s) across the difference between observed and predicted fluxes. Science observation tallies are also shown. See text for full details.

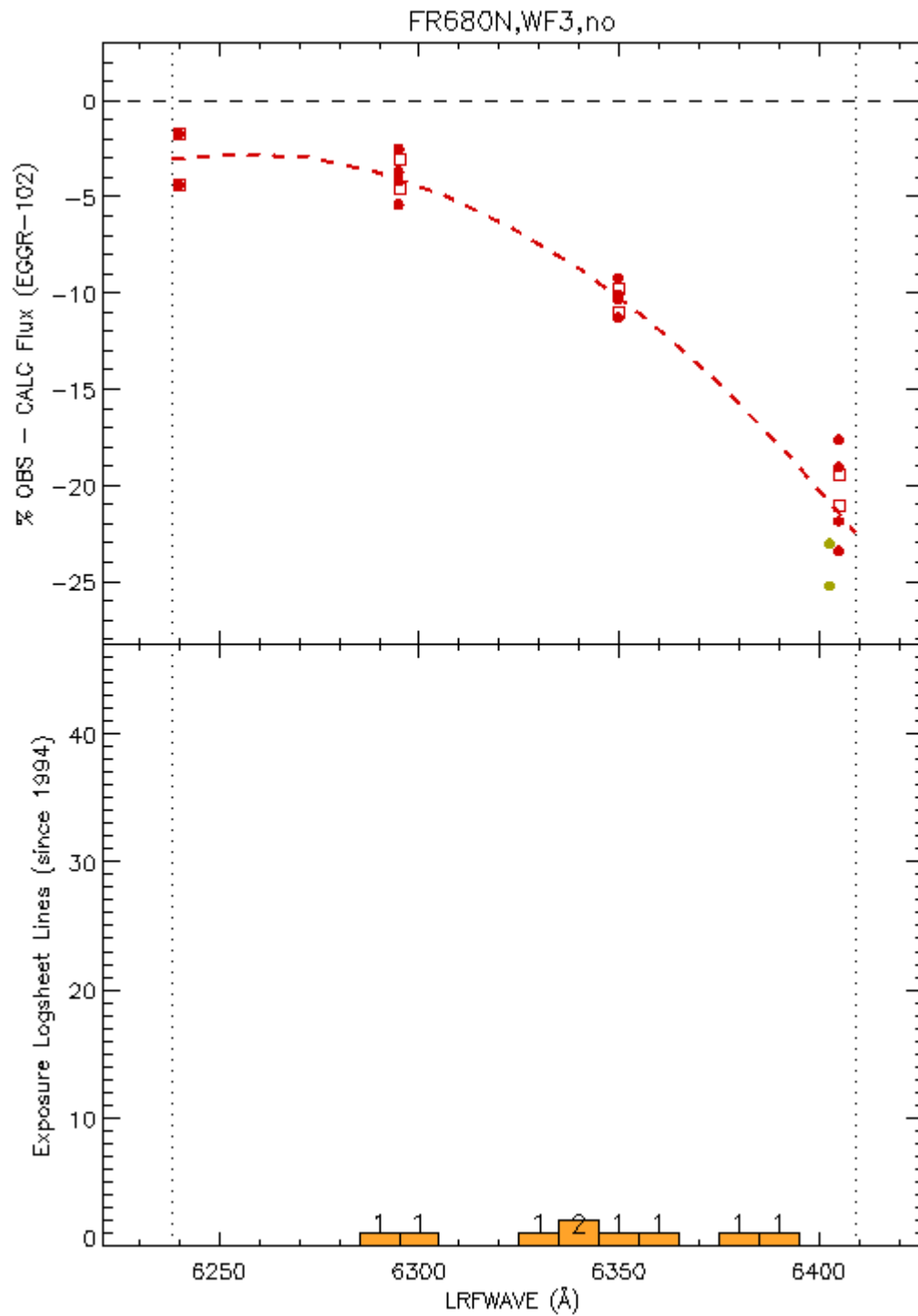


Figure A22: Fitted polynomial(s) across the difference between observed and predicted fluxes. Science observation tallies are also shown. See text for full details.

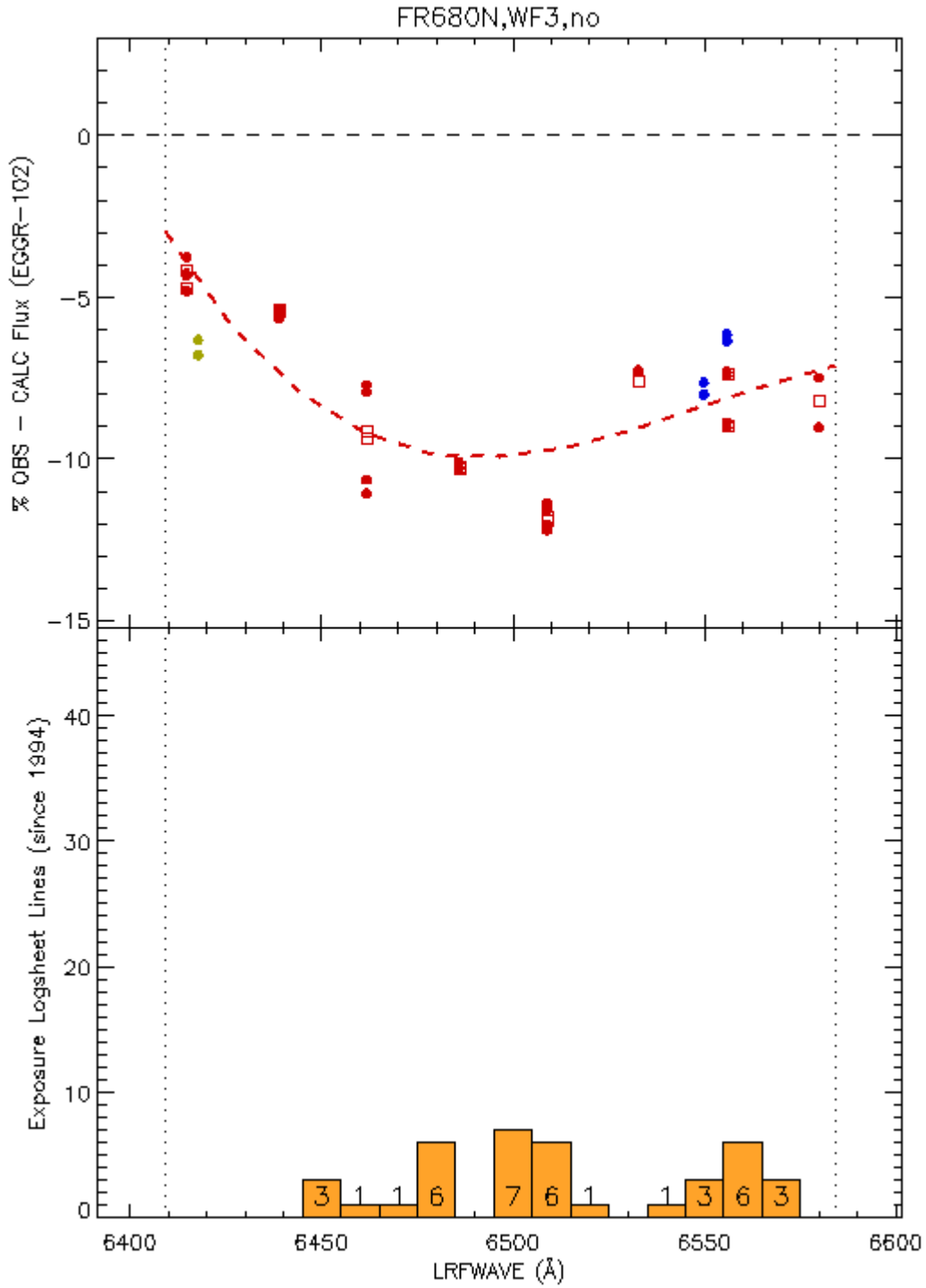


Figure A23: Fitted polynomial(s) across the difference between observed and predicted fluxes. Science observation tallies are also shown. See text for full details.

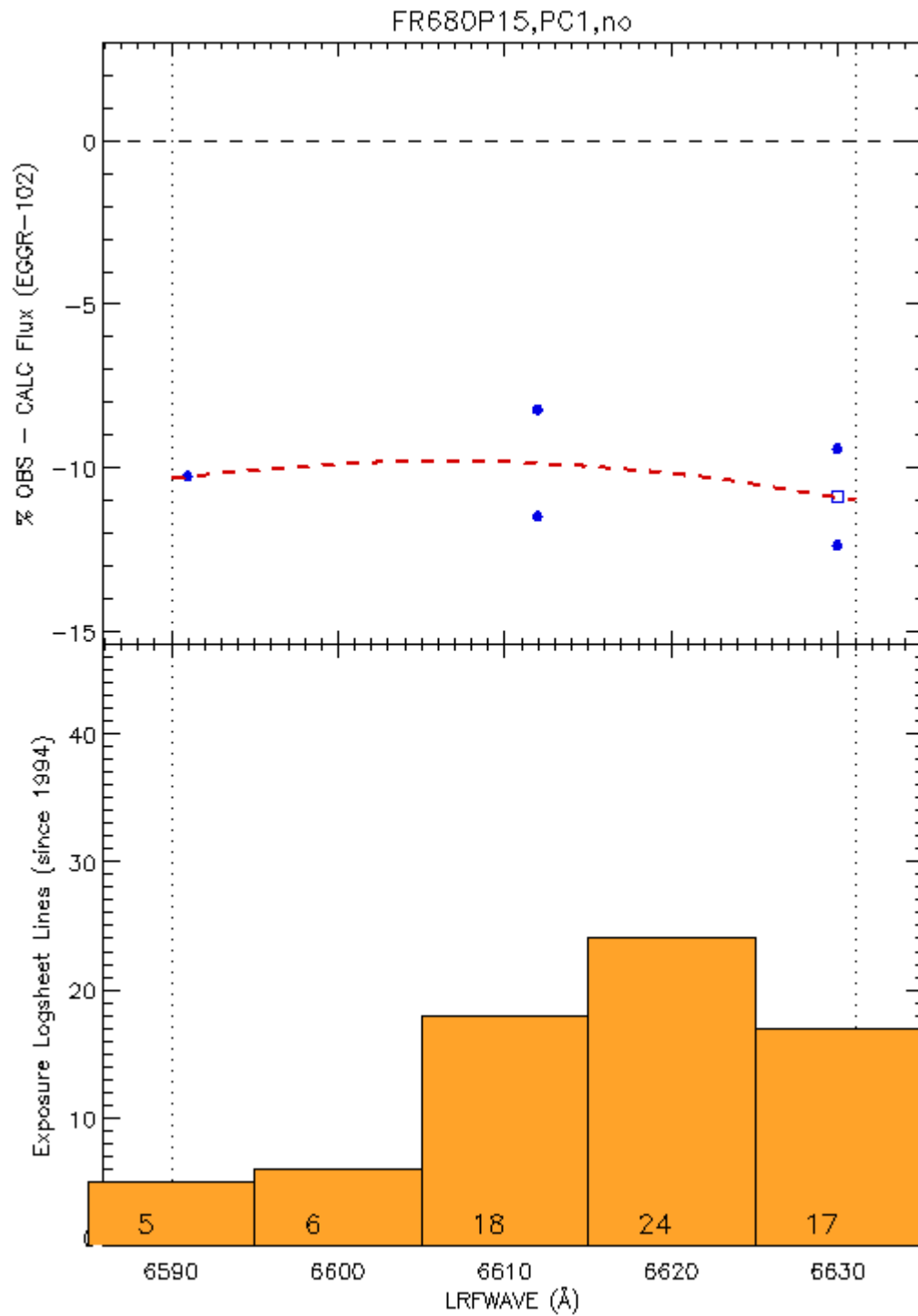


Figure A24: Fitted polynomial(s) across the difference between observed and predicted fluxes. Science observation tallies are also shown. See text for full details.

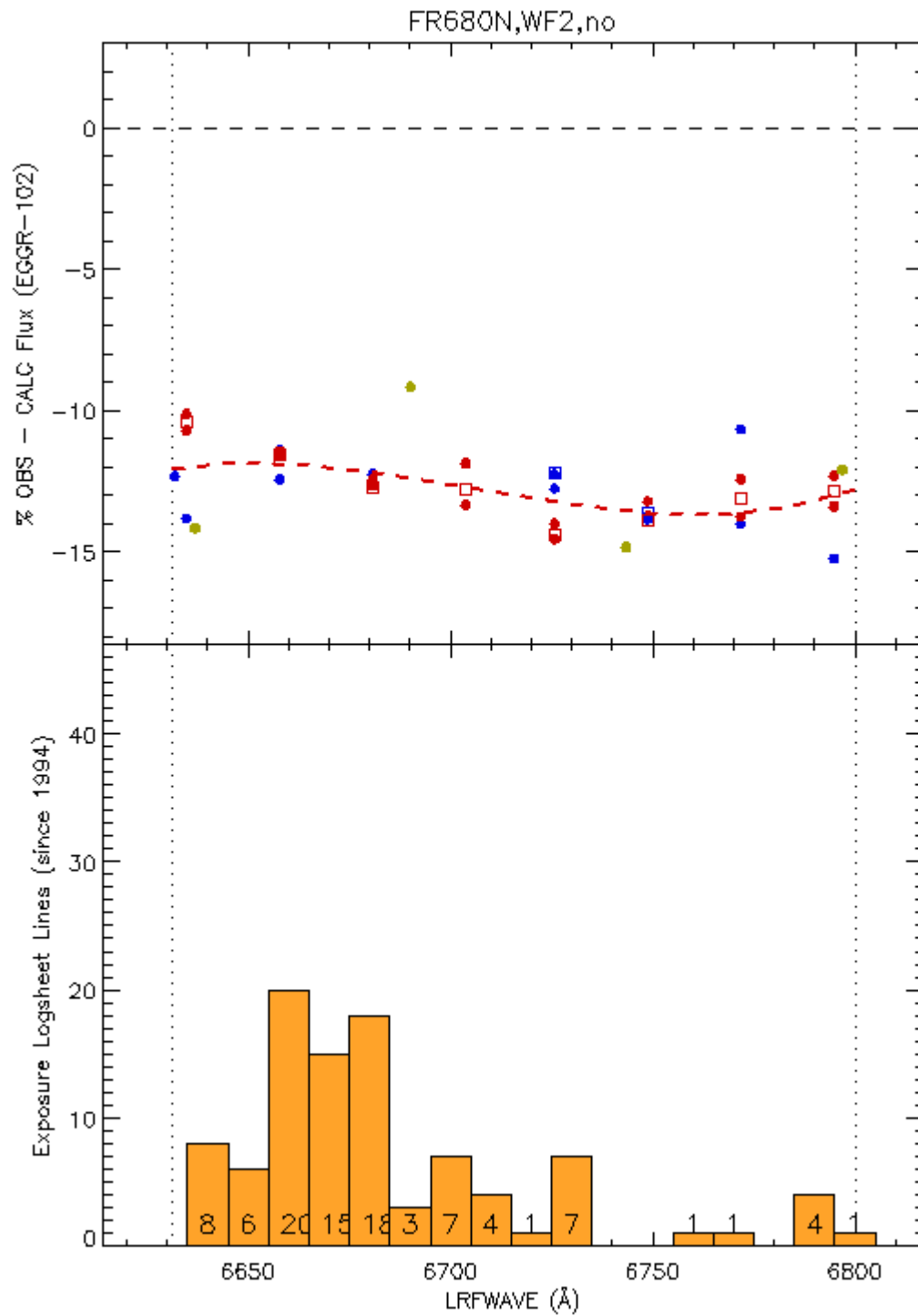


Figure A25: Fitted polynomial(s) across the difference between observed and predicted fluxes. Science observation tallies are also shown. See text for full details.

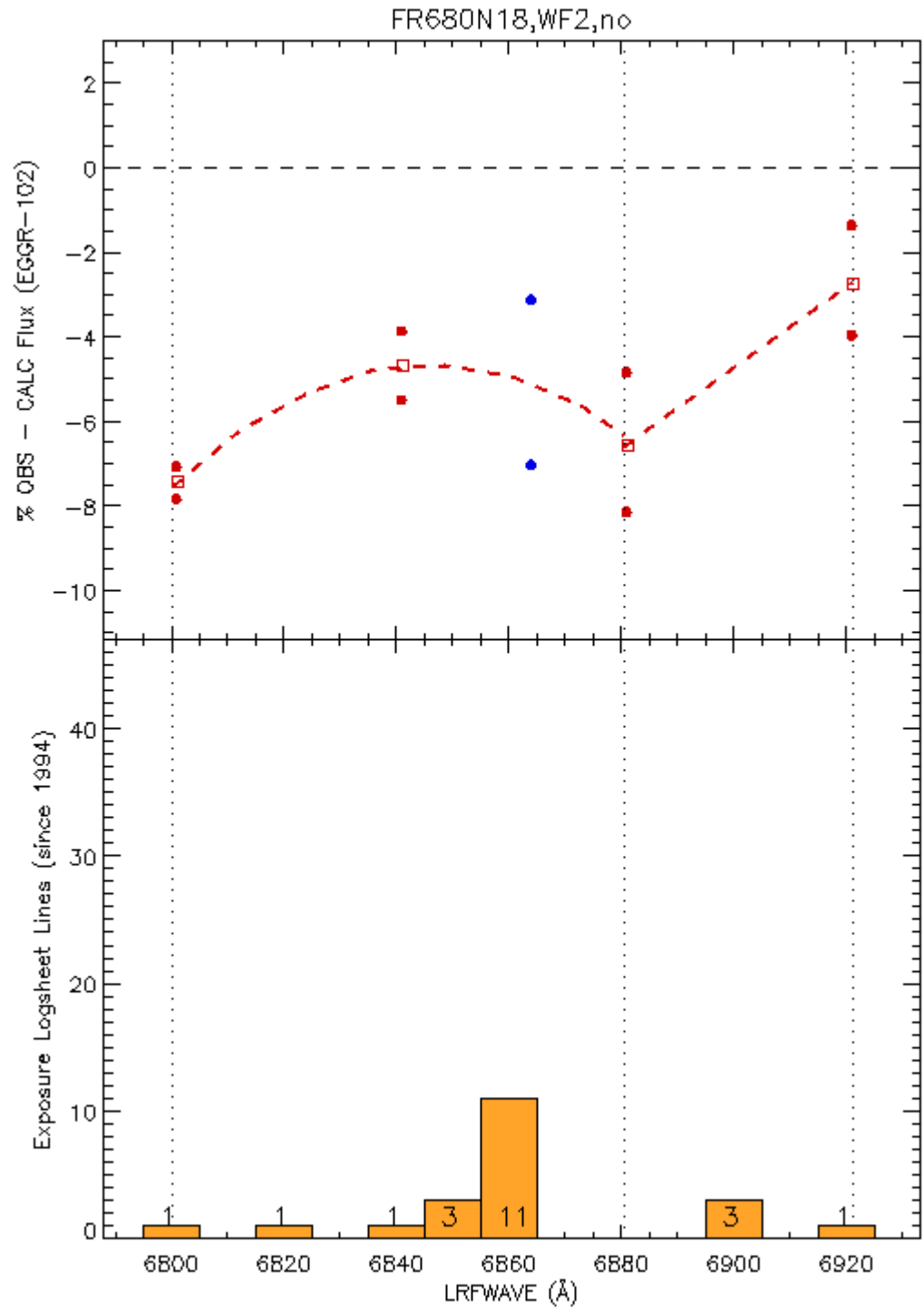


Figure A26: Fitted polynomial(s) across the difference between observed and predicted fluxes. Science observation tallies are also shown. See text for full details.

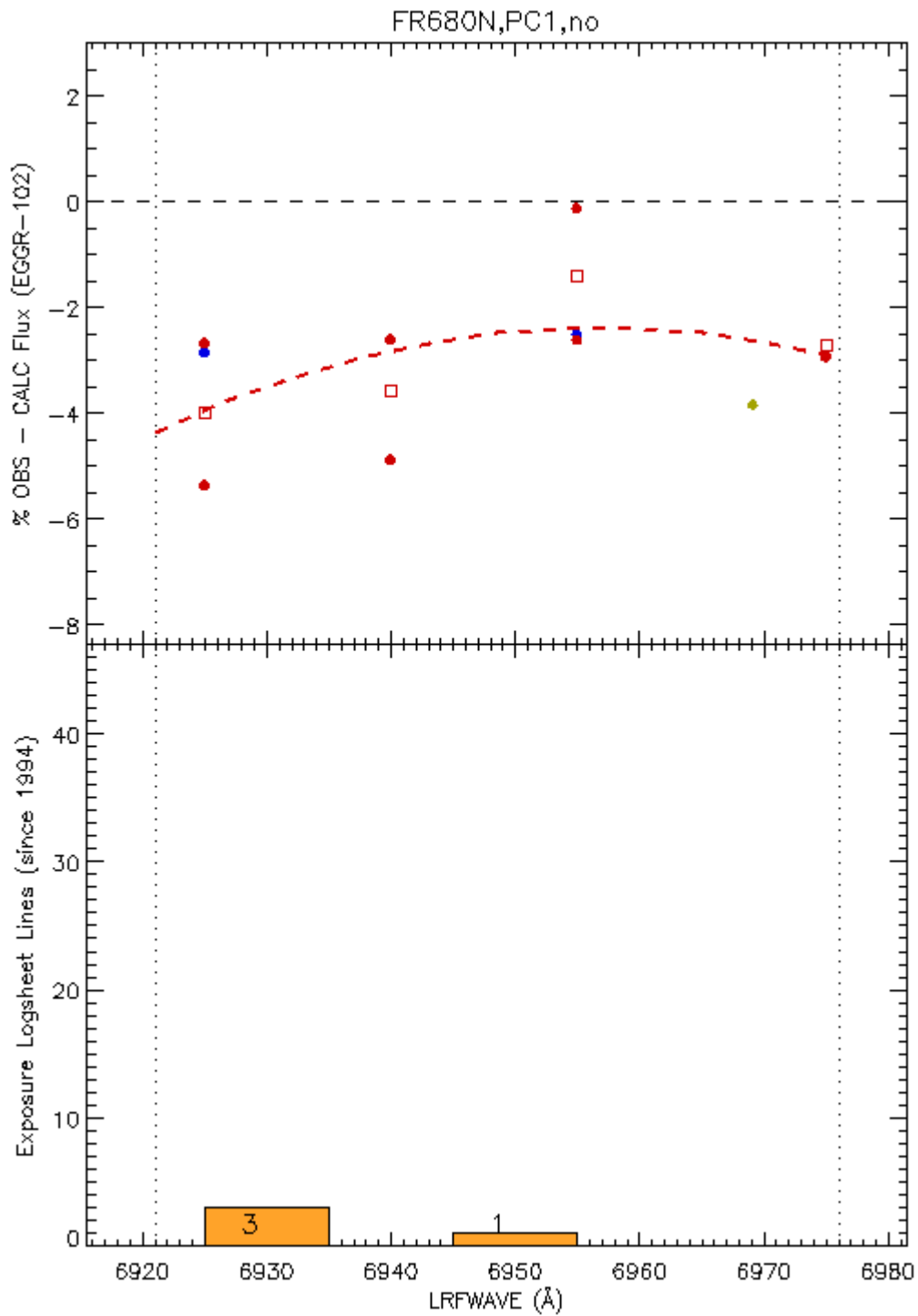


Figure A27: Fitted polynomial(s) across the difference between observed and predicted fluxes. Science observation tallies are also shown. See text for full details.

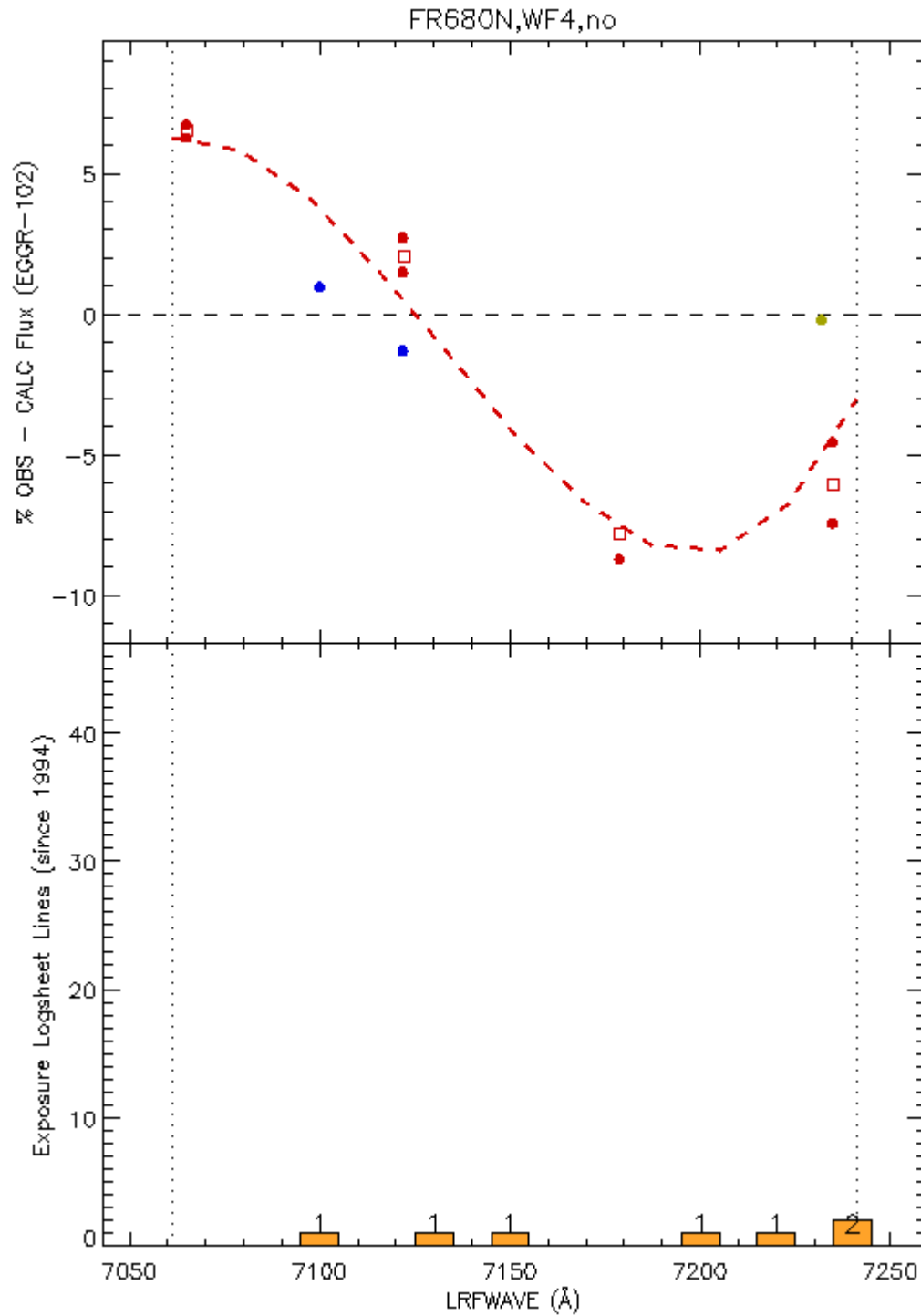


Figure A28: Fitted polynomial(s) across the difference between observed and predicted fluxes. Science observation tallies are also shown. See text for full details.

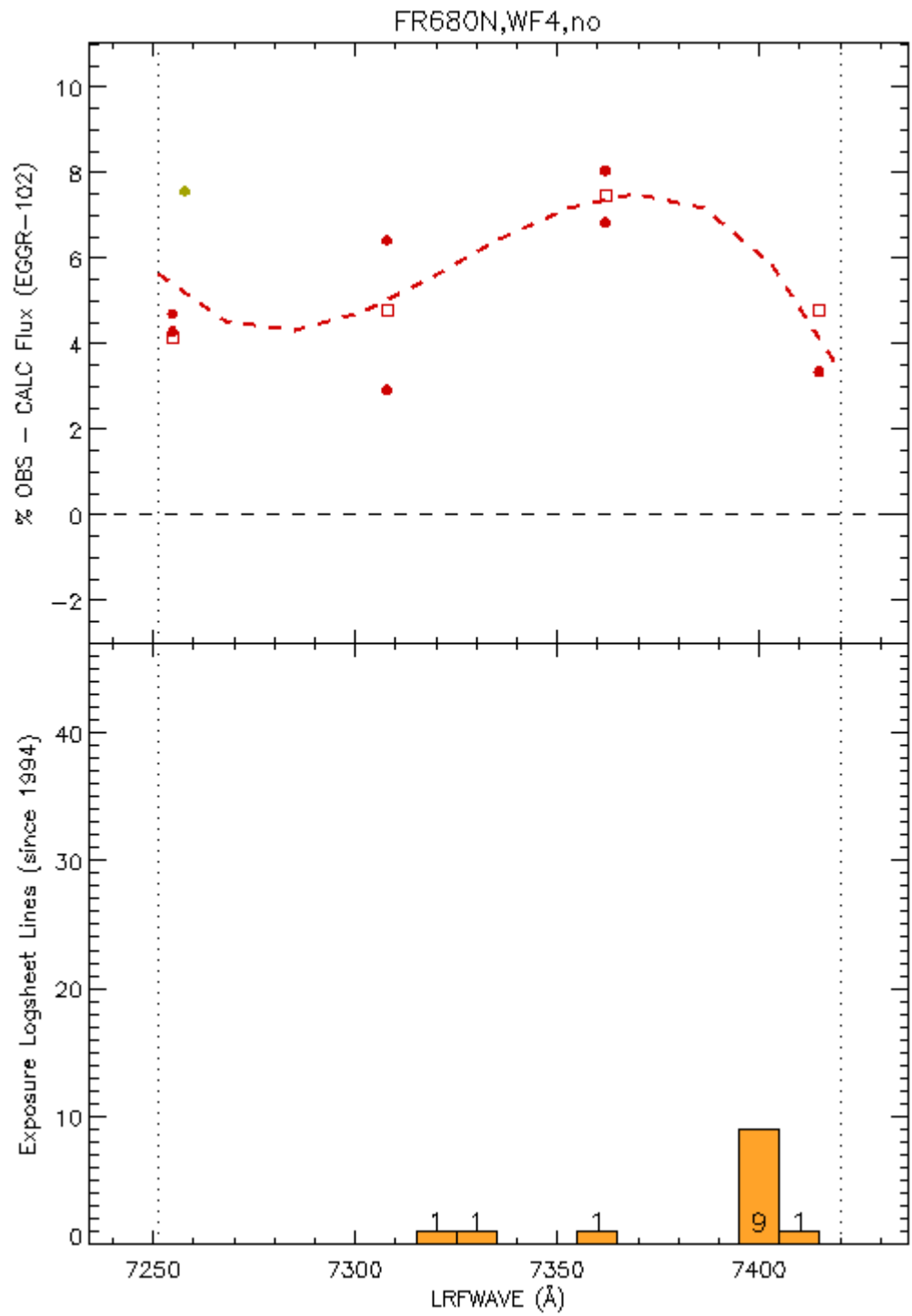


Figure A29: Fitted polynomial(s) across the difference between observed and predicted fluxes. Science observation tallies are also shown. See text for full details.

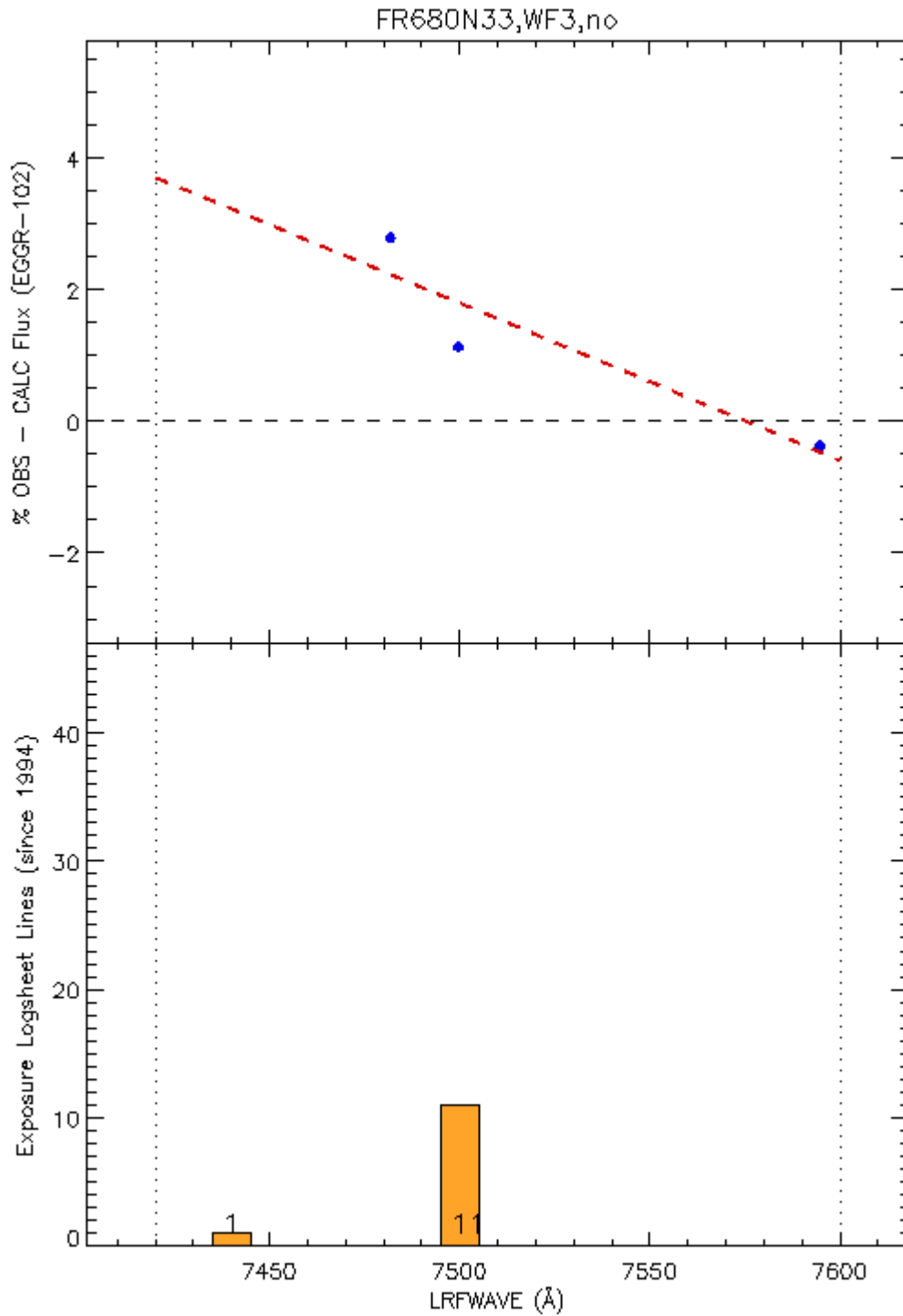


Figure A30: Fitted polynomial(s) across the difference between observed and predicted fluxes. Science observation tallies are also shown. See text for full details.

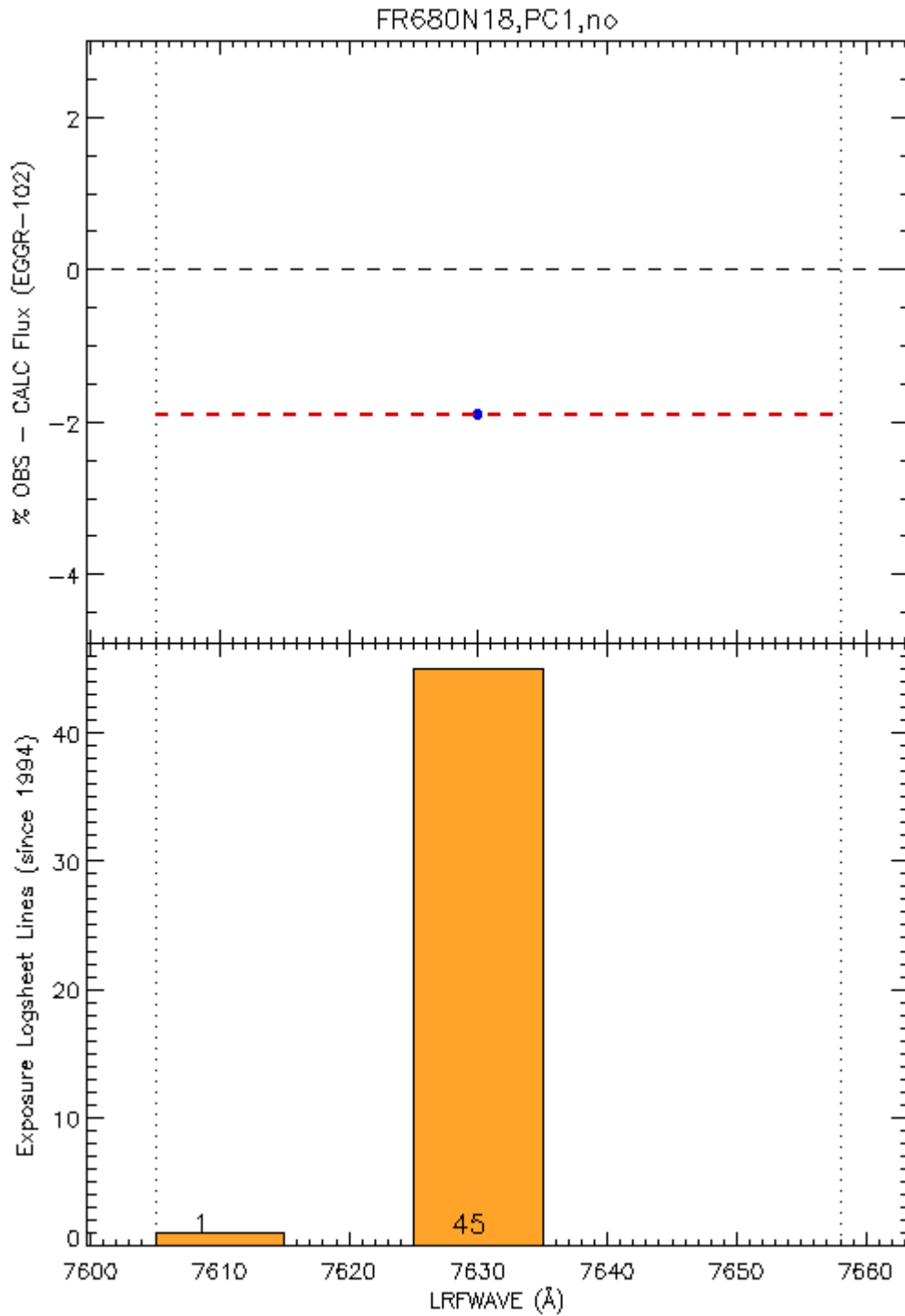


Figure A31: Fitted polynomial(s) across the difference between observed and predicted fluxes. Science observation tallies are also shown. See text for full details.

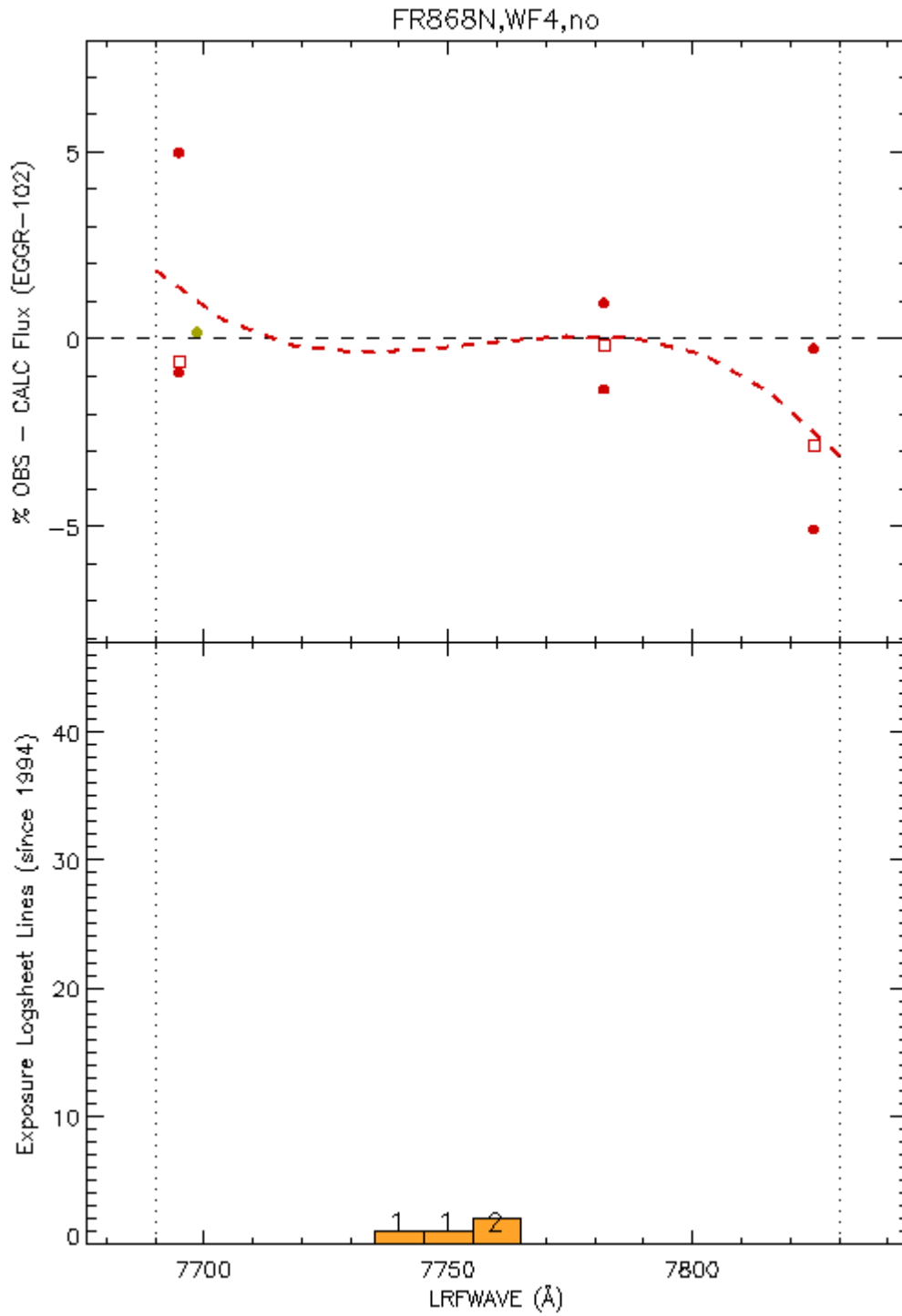


Figure A32: Fitted polynomial(s) across the difference between observed and predicted fluxes. Science observation tallies are also shown. See text for full details.

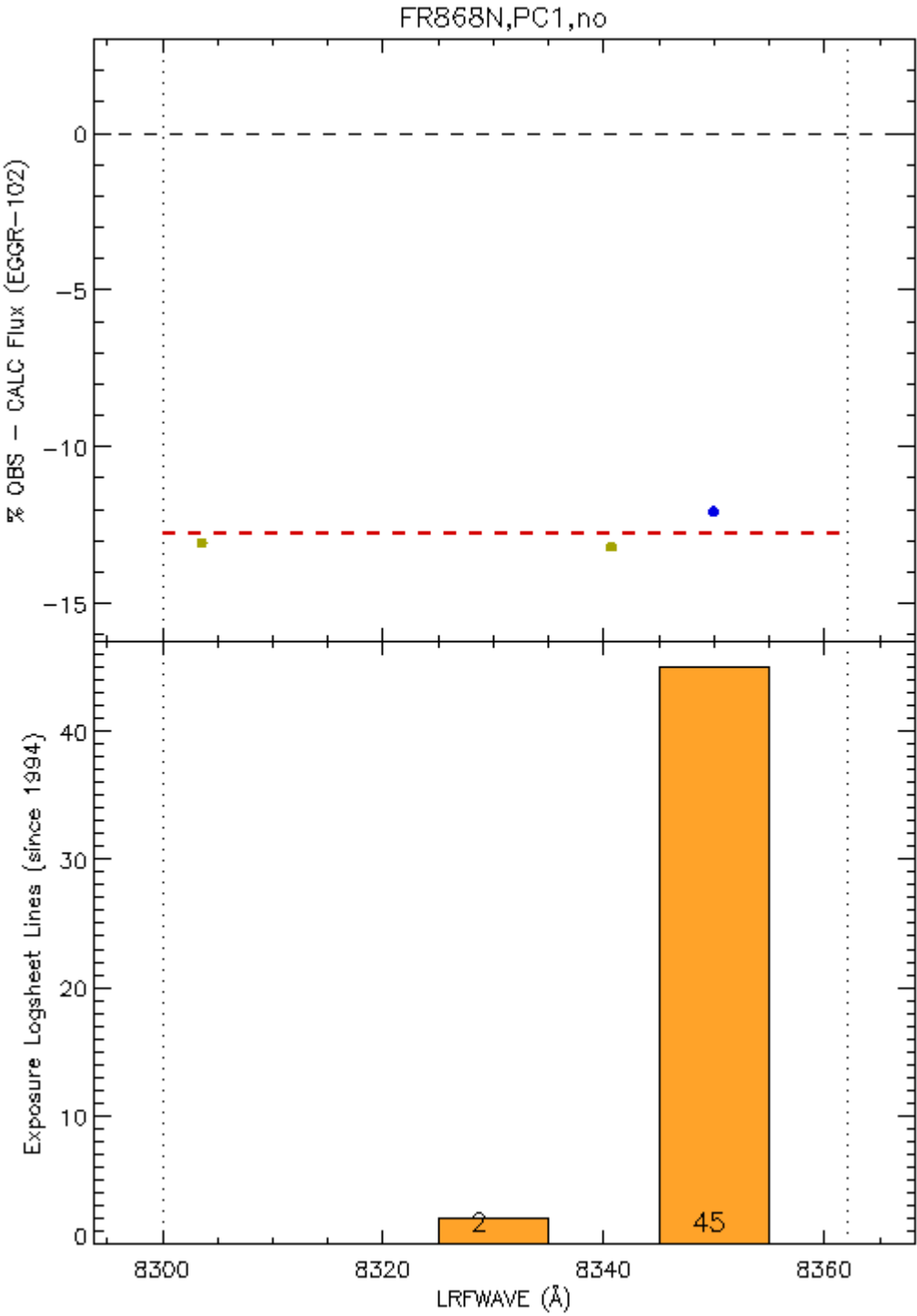


Figure A33: Fitted polynomial(s) across the difference between observed and predicted fluxes. Science observation tallies are also shown. See text for full details.

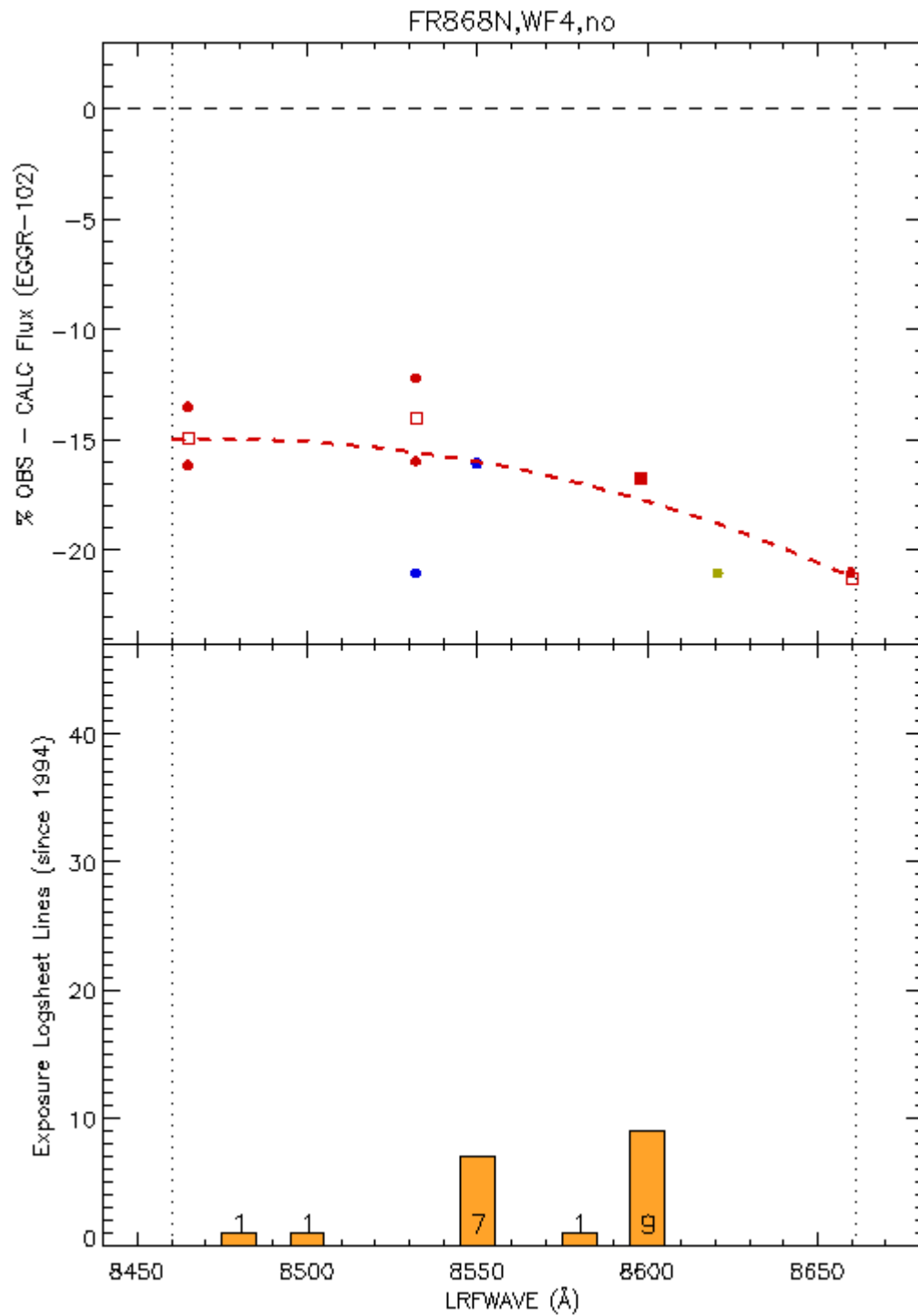


Figure A34: Fitted polynomial(s) across the difference between observed and predicted fluxes. Science observation tallies are also shown. See text for full details.

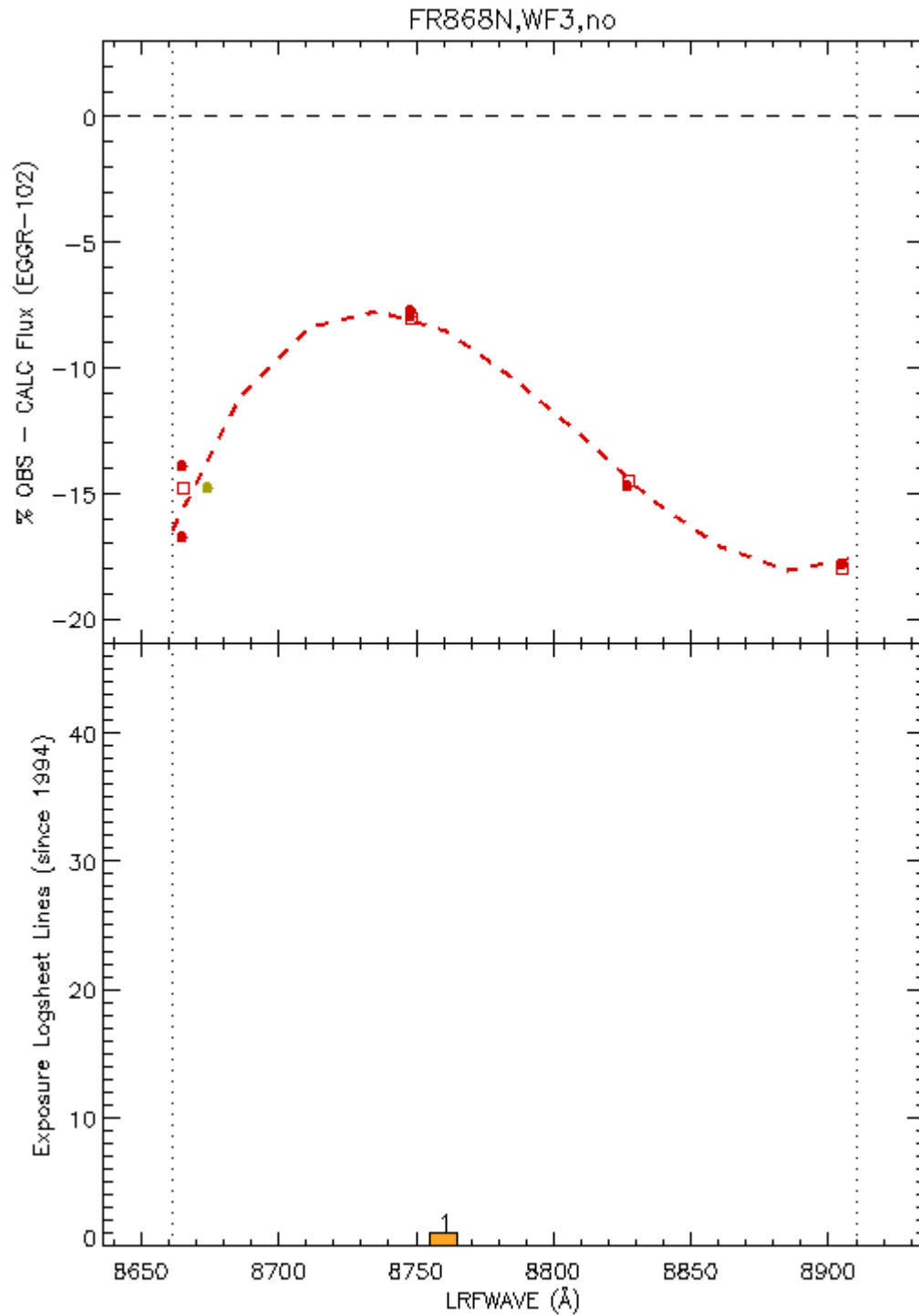


Figure A35: Fitted polynomial(s) across the difference between observed and predicted fluxes. Science observation tallies are also shown. See text for full details.

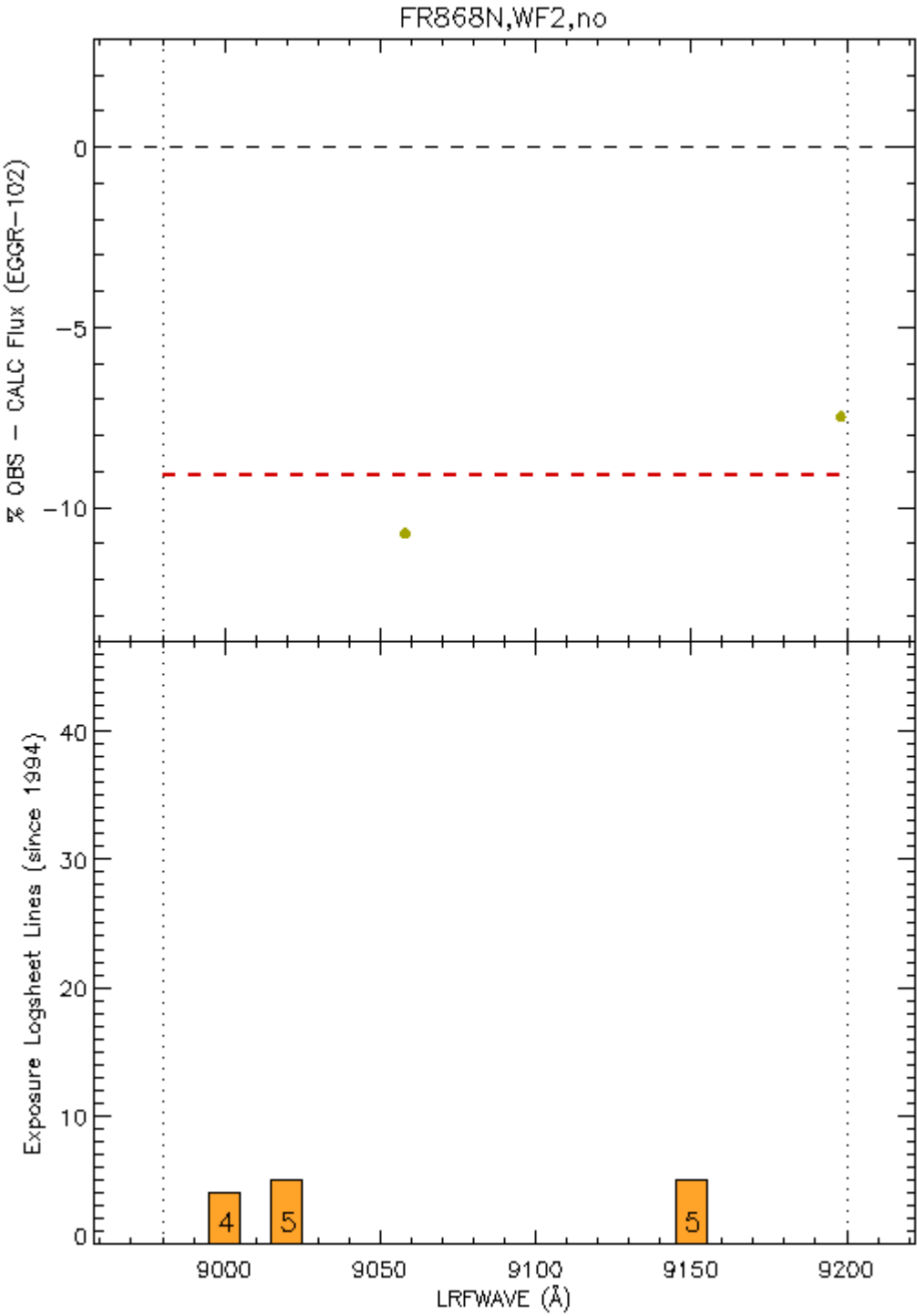


Figure A36: Fitted polynomial(s) across the difference between observed and predicted fluxes. Science observation tallies are also shown. See text for full details.

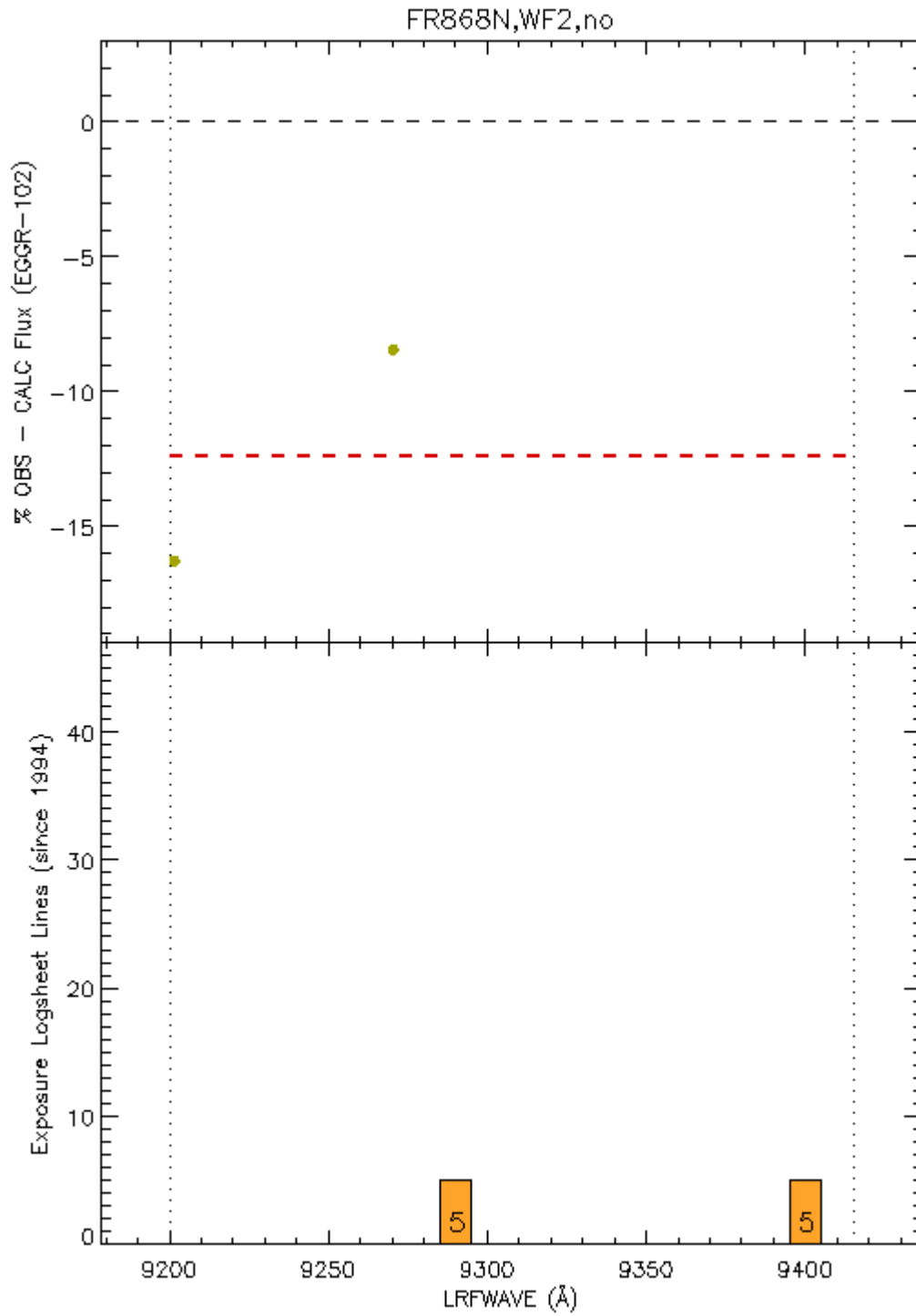


Figure A37: Fitted polynomial(s) across the difference between observed and predicted fluxes. Science observation tallies are also shown. See text for full details.

